University of Nevada, Reno

Study of transport of laser-driven relativistic electrons in solid materials

A dissertation submitted in partial fulfillment of the requirements
for the degree of Doctor of Philosophy in Physics

by

Philippe Leblanc

Dr. Yasuhiko Sentoku/Dissertation Advisor

December, 2013

University of Nevada, Reno
Statewide • Worldwide

THE GRADUATE SCHOOL

We recommend that the dissertation
prepared under our supervision by

PHILIPPE LEBLANC

entitled

Study Of Transport Of Laser-Driven Relativistic Electrons In Solid Materials

be accepted in partial fulfillment of the
requirements for the degree of

DOCTOR OF PHILOSOPHY

Yasuhiko Sentoku, Ph. D., Advisor

Radu Presura, Ph. D., Committee Member

Aaron Covington, Ph. D., Committee Member

Roberto Mancini, Ph. D., Committee Member

Frederick Harris, Ph. D., Graduate School Representative

Marsha H. Read, Ph. D., Dean, Graduate School

December, 2013

Abstract

With the ultra intense lasers available today, it is possible to generate very hot electron beams in solid density materials. These intense laser-matter interactions result in many applications which include the generation of ultrashort secondary sources of particles and radiation such as ions, neutrons, positrons, x-rays, or even laser-driven hadron therapy. For these applications to become reality, a comprehensive understanding of laser-driven energy transport including hot electron generation through the various mechanisms of ionization, and their subsequent transport in solid density media is required. This study will focus on the characterization of electron transport effects in solid density targets using the state-of-the-art particle-in-cell code PICLS. A number of simulation results will be presented on the topics of ionization propagation in insulator glass targets, non-equilibrium ionization modeling featuring electron impact ionization, and electron beam guiding by the self-generated resistive magnetic field. An empirically derived scaling relation for the resistive magnetic in terms of the laser parameters and material properties is presented and used to derive a guiding condition. This condition may prove useful for the design of future laser-matter interaction experiments.

Acknowledgments

First and foremost, I wish to acknowledge my advisor, Dr. Yasuhiko Sentoku, for his support, patience and mentoring over the years. His insights and teachings he has provided me have been invaluable, and without them I would never have completed this work. I also wish to thank my committee members: Dr. Radu Presura, Dr. Aaron Covington, Dr. Roberto Mancini and Dr. Frederick Harris. They have accepted the burden of overseeing this dissertation and the comments and revisions they have provides were immensely useful in improving this document. Furthermore, I wish to thank my parents Normand and Suzanne for their words of encouragement and financial support over the many years I have been in school. It would have been impossible to reach this point without them. Lastly but not least, I wish to acknowledge and thank my girlfriend Montana, for her patience and emotional support during the long nights of writing and revising.

Contents

List of Figures

Chapter 1

Introduction

1.1 Laser-matter interactions

Since the discovery of the theory behind lasing principles by Einstein in 1917 [6] and the development of the first ruby laser by Maiman [7], lasers have been found to be an invaluable tool with many applications. Some of these applications were predicted by Gould [8] where he made mention of spectroscopy, interferometry, radar and nuclear fusion. Over the course of the following 50 years, laser technology would progress at an astounding rate and new applications would be discovered as lasers have become more powerful with superior optical properties.

Initially, the progression of laser intensity for the first five years was rapid going from $\approx 10 \times 10^{7}$ W/cm^{2} to reaching $\approx 10 \times 10^{14}$ W/cm^{2} in that span of time. A seven order of magnitude increase which was caused by the introduction of laser techniques such a "Q-switching" and "Mode Locking". The first lasers were continuous lasers. That is lasers with a constant energy output over time. Both Q-switching and Mode-Locking transformed the traditional continuous beam lasers into pulsed lasers. Q-switching involved the change of the resonant cavity "Quality" (hence the Q) which allowed more light to escape (low Q) to less light to escape the lasing medium (high Q). The build-up of photons would eventually lead to an emitted pulse with much greater energy. Mode-Locking is a technique to fix the relative phase of the independently oscillating modes of a resonant laser cavity. When a laser is mode-locked, all the modes may periodically constructively interfere creating an intense burst of radiation. These techniques were useful to vastly increase laser intensities for the first few years. Around 1965, the limits of traditional pulse amplification techniques began to be felt and laser intensity progress considerably slowed down. It is not until 1985 with the work by Mourou [9] which applied "Chirped Pulse Amplification", a technique being used for radars, to further amplify lasers.

Traditional techniques of amplifications have limitations which were quickly reached by the fast improvements in laser intensity. An amplifier gain medium will begin to show a non-linear response as the beam grows in intensity which leads to the situation where the beam itself may become too intense, and damage the optical amplifying elements. Chirped Pulse Amplification was a technique introduced to circumvent the limitations posed by laser gain medium amplification. The basic idea is to drop the pulse intensity by spatially stretching the beam which has the consequence of lowering its power. To achieve this, the laser beam is directed to a branch of the optical pathway where it will interact with a diffraction grating apparatus. The grating will diffract and split the various electromagnetic modes of the laser at different angles. The spectrally spread beam is then refocused on a second grating which parallelizes the different wavelengths. The beam is then reflected back by a perpendicular mirror through both gratings which refocuses the beam into its original diameter. The return beam however is approximately a thousand times longer spatially and therefore a thousand times less intense.

The stretching occurs because the different wavelengths will travel different distances between the gratings and the reflecting mirror. The stretching apparatus will have have a positive dispersion causing the red (long) wavelengths to travel a shorter distance which means they will end up at the front of the pulse when it returns. Blue wavelengths will travel a longer distance and end on the tail of the pulse. The stretched beam is far less intense and less therefore hazardous to the gain amplification medium. The beam is then safely amplified as much as possible up to the limits the gain mediums may allow. As the beam then exits the amplification stages in its spectrally spread form, it enters the compression phase. Again, a pair of gratings are used which this time offer negative dispersion with blue wavelengths and red wavelengths traveling shorter and longer paths respectively. This will reverse the spectral spread and effectively compress the beam back to its original length. However, the beam will have acquired far more energy after undergoing amplification so the compress beam will be incredibly intense.

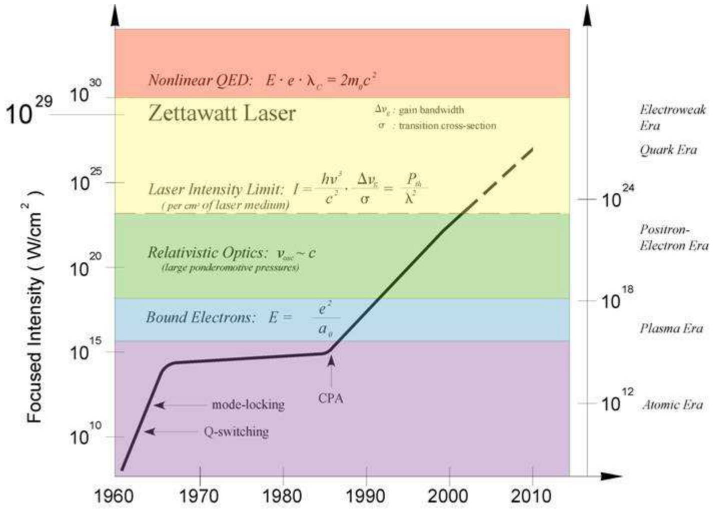

Figure 1.1: Progress of laser technology (intensity).

Chirped Pulse Amplification is still the state-of-art technique to achieve extremely high intensities. Fig. 1.1 shows that post-1985, laser intensities began to grow again at a very rapid pace once it was adopted. Today, there are multiple petawatt class lasers (10×10^{21} W/cm^2) in use around the world. For example, Osaka University has the Petawatt Module Laser [10], Rutherford Appleton Laboratory in the United Kingdoms has the Vulcan Laser [11], Lawrence Livermore National Labs had the PETAWATT laser system [12] and University of Texas has the Texas Petawatt system [13]. In recent years, the community has begun discussing the possibility for lasers of even greater intensity, that is Exawatt or even Zetawatt class lasers [14, 15].

The ultra-rapid delivery of energy offered by these lasers have made them ideal tools to study extreme states of matter at very high temperatures and densities, also known as high energy density physics. They may apply very high pressures due to strong electromagnetic field components. For example, using the Poynting vector, the pressure applied by a laser can be expressed as

$$P = \frac{\langle S \rangle}{c} = \frac{I}{c} \tag{1.1}$$

Where I is the intensity and c is the speed of light. A petawatt class laser delivers an intensity of 10^{21} W/cm^2. This means the pressure from Eq. 1.1 calculates to 3.3×10^{18} pascals or 33 Tbar. At such pressures, non-linear mechanical shocks may be produced which quickly heat up any material to the point of ionization transforming the target into a solid density plasma. Although many experiments have been conducted to study the plasma kinetic effects in low density targets such as various gases, the discussion which follows will focus around what are known as overdense targets, and more specifically solid density plasmas. The physics inside overdense plasmas is not well understood. This is due to limitations of experimental diagnostics and their capability to probe such overdense matter for sub picosecond time scales. In this present work, we study the high energy density physics by numerical simulation to clarify how laser-driver plasmas are formed and how energy is transported in such solid density plasmas.

In the following discourse, we present a series of topics on laser-plasma interactions via computer simulations. A kinetic Particle-in-Cell code is used for this end, the structure and inner workings of which are elaborated in the following chapter. In chapter 3, the code is used to perform a series of simulations designed to explain certain aspects of electron transport in solid materials. Specifically, a study is first presented on the features of ionization in a glass insulator target with results showing the structure of the ionization wave launched as a result of intense laser heating. Results are compared with experimental data to good agreement. Then, a discussion on a new ionization model suited to calculate ionization in non-equilibrium plasmas. A comparison between this new model and the widely used Thomas-Fermi model is then presented. Finally, a study on the role of resistivity in guiding electron transport is shown. A scaling of the resistive magnetic field is derived which provides a threshold based on material and lasers properties to predict when guiding occurs or not. It is benchmarked against 2D PIC simulations which are shown to be in good agreement with the empirical scaling and experimental results.

Before discussing particle kinetics in solid targets, a discussion on laser absorption physics is presented to explain how laser light interacts with solid overdense targets to produce electrons in the first place.

1.2 Laser absorption mechanisms

Laser absorption involves numerous mechanisms which depend on the intensity of the laser as well as the geometry of the surface of the target. The threshold between when a plasma is underdense versus overdense is defined by the the critical density n_c. This density is derived from the dispersion relation for a cold collisionless plasma [16]

$$\omega^2 = {\omega_p}^2 + c^2 k^2 \tag{1.2}$$

where ω is the angular frequency of the laser, ω_p is the plasma frequency and k is the wave number. When $\omega^2 = \omega_p^2$, the wave number k becomes zero which indicates the laser may no longer propagate through the plasma. The plasma frequency depends on the density which can be solved to obtain the critical density.

$$\omega^2 = \omega_p^2 = \frac{4\pi e^2 n_c}{m} \Rightarrow n_c = \frac{m\omega^2}{4\pi e^2} \tag{1.3}$$

For a 1 μm laser, this corresponds to a density of $\approx 1.1 \times 10^{21}$ cm^{-3} and this means that neglecting another effect known as relativistic transparency, lasers will not penetrate a plasmas beyond this density.

For high intensity lasers ($10^{15} < I < 10^{18}$ W/cm^2), absorption physics is dominated by what are known as collisionless processes. The super strong electric field rapidly generates electrons by field ionization. These electrons are then heated to highly relativistic energies and very quickly become non-collisional on the timescale of ≈ 10 fs. In the case where a laser interacts with a perfectly sharp density interface, the surface becomes highly ionized causing it to become reflective. Then laser absorption can be treated using metal optics using the general Helmholtz equation. This yields an eventual scaling of the electron temperature such as $T_e \propto I^{4/9} t^{2/9}$. Since the collision frequency scales as ${T_e}^{-3/2}$, this means $\nu_{ei} \sim I^{-2/3} t^{-1/3}$

which shows how the collision rate drops with increasing intensity. The effective collisional rate is also dependent on the electron quiver velocity $v_{os} = eE_0/m\omega$ through the following relation:

$$\nu_{eff} \simeq \nu_{ei} \frac{{v_{te}}^3}{({v_{os}}^2 + {v_{te}}^2)^{3/2}}. \tag{1.4}$$

When the oscillation velocity becomes comparable to the thermal velocity for high intensity lasers, the previous relation shows how the collision rate becomes significantly smaller. Now that collisional heating has been shown to be less important in the regimes of interest, we shall cover the various collisionless heating mechanisms of electrons in high density targets: resonant absorption, vacuum heating, anomalous skin effect, sheath inverse-bremsstrahlung and finally $J \times B$ heating.

1.2.1 Resonance absorption

This heating mechanism usually works best when the density gradient between the vacuum and the solid is shallower. When laser light which presents an electric field with an oscillatory component in the propagation plane (so called ‘p-polarization’) travels through a rising density gradient, it will eventually reach a point where the density becomes critical. At this point, the normal component of the laser E-field will drive a plasma wave as electrons at the critical surface are pushed by the oscillating electric field. After a few laser cycles, this wave will transfer some energy to the surrounding medium either by particle trapping or wave breaking. The absorption fraction is related to the parameter $\xi = (kL)^{1/3} \sin\theta$. Here k is the wave vector, L is the scale length given by $\frac{d}{dx}\mathrm{logN_e}|_{\mathrm{x=x_c}}$ and θ is the angle of incidence. Then the angular absorption is expressed as $\phi(\xi) \simeq 2.3\xi\mathrm{exp}(-2\xi^3/3)$ [17]. This mechanism is known as resonant absorption since the absorption function just described results in a peak around $\xi \approx 0.75$, the optimal value to drive this heating process. The function tells us that for very low intensities with short scale lengths, the parameters will be off resonance and heating by this method will be reduced. The laser simply does not have the energy to effectively drive the Langmuir waves before they dissipate. However, very high energies and scale lengths have the same effect. The laser must tunnel through more matter before reaching critical density, and the higher intensity will cause the electron’s quiver velocity to be too high to effectively drive waves.

1.2.2 Vacuum heating

As seen in the previous section, short scale density gradients reduce the efficiency of resonance absorption substantially. The oscillation amplitude of the electron in such a case would exceed the density scale length L and cause the waves to break down. However, if the density gradient is sufficiently short, electrons that lie at the critical surface are directly exposed to the laser field full vacuum value. At a certain point during the laser oscillation, the electrons will suddenly be pulled out by the Lorentz force applied by the laser in the vacuum region. As the laser field keeps oscillating, the force eventually reverses course to push the electrons back into the material. Due to the overdense nature of the target, the skin lengths (which is estimated by c/ω_p) is quite short preventing the electric field from extending deeply into the solid. This will allow the now forward moving electron to loose little kinetic energy and be launched with great energy and speed. These electrons will travel relatively uninhibited with long mean free paths with this energy deposition mechanism known as Brunel or vacuum heating [18].

The model assumes two conditions. First, that the magnetic field component in the interaction region is negligible and can thus be ignored. Second, the electric field must have at least part of its component normal to the target surface. Then the electric driver can be expressed as

$$E_d = [1 + (1 - \eta_a)^{1/2}] E_L \sin\theta. \tag{1.5}$$

This expression includes a correction for imperfect reflectivity in η_a which is the classical absorption rate

$$\eta_a = \frac{4}{\pi} \frac{v_{os}}{c} \frac{\sin^3\theta}{\cos\theta}. \tag{1.6}$$

Then E_d and E_L are the driving electric field and the full electric field respectively. Applying relativistic corrections to the kinetic energy of the electrons in absorbed power P_a, that is

$U_k = (\gamma - 1)mc^2$, we then obtain an expression for the fractional absorbed power.

$$\eta_B = \frac{P_a}{P_L} = \frac{c}{\pi v_{os}} f \left[\left(1 + f^2 \left(\frac{v_{os}}{c} \right)^2 \sin^2\theta \right)^{1/2} - 1 \right] \frac{\sin\theta}{\cos\theta} \tag{1.7}$$

$$f = 1 + (1 - \eta_a)^{1/2} \tag{1.8}$$

The parameter of interest is $a_0 = v_{os}/c$ which is directly related to the driving laser field. Two limiting cases exist: the low intensity case where $a_0 \ll 1$ and the relativistic case with $fa_0 \sin\theta \gg 1$. The model predicts an increasing absorption as the angle of incidence becomes greater. Also included, however, is the pump depletion effect which prevents the absorption from reaching unphysical levels. What changes between both limiting cases is the rate of increase of absorption with respect to the angle. For low intensities, the absorption increases more gently at first, then ramps up quickly in an exponential shape and then rapidly falls due to pump depletion after reaching the maximum absorption at a wide angle. For the high intensity case, the initial increase in absorption is faster and will reach the maximum absorption at a smaller angle. The model tells us the angle will get smaller the greater the laser intensity.

The Brunel vacuum heating model competes with resonance absorption. By running multiple simulation with varying scale lengths and intensities, a transition can be seen when Brunel absorption becomes less efficient and resonance absorption becomes dominant. For extreme laser intensities however, vacuum heating is more important.

1.2.3 Anomalous skin effect

The normal skin effect is characterized by electron oscillations within the distance of the skin length $l_s = c/\omega_p$. These electrons are driven by the laser pulse and are assumed to be locally thermalized within the skin length. That is, their mean free path is less than the skin length so they dissipate the energy they acquire through collisions with local ions. However, when intensity is increased, the temperature will invariably increase as well which carries the consequence that the electron mean free path may exceed the skin length. This is what is known as the anomalous skin effect (ASE).

The electron collision distance must then change to be expressed in terms of the new length over which the electric field is penetrating the surface, l_a. The effective collision rate is then expressed as the thermal velocity over the anomalous skin length or $\nu_{eff} = v_{te}/l_a$. One of the results from collisional absorption theory is the effective collisional skin depth $\delta_s = (c/\omega_p)|1 + i\nu|^{1/2}$. This relation can be adapted for the anomalous skin effect by replacing ν in the previous equation with v_{eff} [19].

$$l_a \simeq \frac{c}{\omega_p}\left(\frac{v_{eff}}{\omega}\right)^{1/2} = \frac{c}{\omega_p}\left(\frac{v_{te}}{\omega l_a}\right)^{1/2} l_a \simeq \left(\frac{c^2 v_{te}}{\omega {\omega_p}^2}\right)^{1/3} \tag{1.9}$$

This particular effect is closely related to the Brunel vacuum heating. The difference lies in the non-locality of the relationship between the current and electric field. Whereas in vacuum heating, the current depends only on the electric field, the ASE accounts for electrons which are pushed beyond the skin length where they return by the electric sheath field they create beyond δ_s and up to l_a. Fig. 1.2 presents a comparison between both closely linked heating processes.

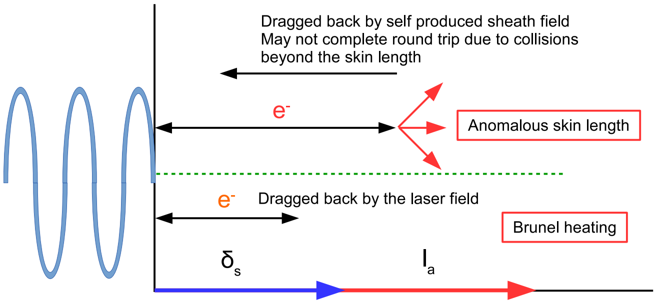

Figure 1.2: This figure presents a comparison of the anomalous skin effect and the Brunel or vacuum heating. The lower portion depicts the Brunel case where the electron is driven directly by the laser field which penetrates up the the skin length. For high intensities, the laser may drive electrons beyond the skin length where additional collisional events take place. They return through the self-generated sheath field.

A later treatment of the derivation of the anomalous scale length by Rozmus and Tikhonchuk (see Ref. [20]) uses a different approach to derive this effect. By assuming the electrons driven by the laser form a Maxwellian velocity distribution in a first order approximation, the distribution can be integrated to obtain the anomalous skin length. The same equation as Eq. 1.9 is obtained with the addition of a multiplication constant $(2/\pi)^{1/6}$.

Then the fractional absorption is derived to be

$$\eta_{ase} = \frac{8\omega l_a}{3\sqrt{3}c} \simeq \left(\frac{T_e}{511keV}\right)^{1/6}\left(\frac{n_c}{n_e}\right)^{1/3} = \frac{4l_a}{3\pi\sqrt{3}\lambda_{laser}} \approx 0.76\frac{l_a}{\lambda_{laser}} \tag{1.10}$$

In the high intensity limit, Brunel heating yields an absorption coefficient of

$$\eta_{vh}{}^{rel} = \frac{4\pi\frac{sin^2\theta}{cos\theta}}{\left(\pi + \frac{sin^2\theta}{cos\theta}\right)^2}. \tag{1.11}$$

Since l_a is longer than the laser wavelength for relativistic laser intensities, the effective absorption is always greater than 75% according to the anomalous skin length which is approximately twice the Brunel absorption at 10^{18} W/cm^2 [17].

1.2.4 Sheath inverse-bremsstrahlung

Whereas the anomalous skin effect describes heating when the electron transit time through the plasma skin length is shorter than the laser wavelength, Sheath-inverse-bremsstrahlung describes the exact opposite. That is, the electron transit time is longer than the laser period. In such a scenario, the electron receives energy via irreversible pushes by the laser field. The treatment by Yang *et al.* [21] derived the fractional absorption in this limit which resulted in

$$\eta_{sib} = \frac{8}{\sqrt{2\pi}}\frac{v_{te}}{c}\frac{a[(a+1)\exp(a)E_1(a) - 1]}{\frac{1}{2} + \frac{\sqrt{\pi a}}{2}\exp(a)\mathrm{erfc}(\mathrm{a}^{1/2})}. \tag{1.12}$$

1.2.5 $J \times B$ heating

The final collisionless absorption mechanism to be discussed is what is commonly known as $J \times B$ heating. The Lorentz force can be divided into two parts.

$$\vec{F} = -e\left(\vec{E} + \frac{\vec{v}}{c} \times \vec{B}\right) \tag{1.13}$$

So far, the discussion has been focused on the electric field contribution to absorption physics. However, the other portion represented by the term $\vec{v} \times \vec{B}$ is also capable of contributing to heating. Given a linearly polarized laser beam, the electric field can be written as $E = E_0(x)\hat{y}\sin\omega t$. Using the equation for the ponderomotive force

$$F_p = -\frac{e^2}{4m\omega^2}\nabla E^2, \tag{1.14}$$

and by substituting the sinusoidal electric field in this expression, the derivation can be carried out to find the x component [22]. The resulting force expression is

$$f_x = -\frac{m}{4}\frac{\partial {v_{os}}^2(x)}{\partial x}(1 - \cos 2\omega t). \tag{1.15}$$

The first term is the ponderomotive force while the second term is the "$J \times B$" term. Notice the 2ω in the cosine function as it indicates this mechanism operates at twice the laser frequency. The $J \times B$ heating will inject electrons in the target twice per laser cycle.

This concludes the discussion on absorption mechanisms for high intensity lasers ($I > 10^{15}$ W/cm^2). For normally incident laser beams, vacuum heating and its two special cases of anomalous skin effect and sheath-inverse bremsstrahlung become negligible and give way to resonant absorption (if the scale length of the density gradient is long) and $J \times B$ heating. As the angle of the laser beams shift from normal incidence to grazing angles, vacuum heating and skin effects become more important as the laser's electric field begins to drive electrons directly. All these mechanisms have become crucial elements in understanding the fundamentals of laser-plasma interactions as they form the theoretical background of energy deposition on a femtosecond timescale. Since electrons are the primary energy carriers for short times after laser energy deposition, the physics behind their generation from cold bulk matter is an important step towards realizing a fully self-consistent model of electron transport in laser-driven plasmas.

1.3 Nuclear fusion

Since the day when mankind first split the atom, the discovery of nuclear fission provided the potential for a great increase in energy production over the widespread use of fossil fuel. However, nuclear fission has its drawbacks with the production of radioactive waste which requires very special handling to be properly disposed. This is one of the major reasons why fission has not seen sweeping adoption despite rapidly growing energy demands of modern society. The principles of nuclear energy production relies on the release of binding energy of nuclei. Fission is the process of splitting heavier elements into two or more lighter constituents. During this process, one can measure a small difference in the total mass of the parent nucleus in comparison to the mass of the daughter nuclei. This mass difference accounts for what is known as the binding energy. Through Einstein's famous mass-energy equivalency equation $E = mc^2$, one can see that the extra mass the parent nuclei had is released as energy and because of the c^2 term, even smalls amount of mass can yield large amounts of energy. One of the most common nuclear fuels used today is Uranium-235. For perspective, the common reaction used today is

$$^{235}_{92}\mathrm{U} + ^{1}_{0}\mathrm{n} \rightarrow ^{141}_{56}\mathrm{Ba} + ^{92}_{36}\mathrm{Kr} + 3^{1}_{0}\mathrm{n} \tag{1.16}$$

This reaction releases 202.5 MeV of energy or 83.14 TJ/kg and the release of additional neutrons allows for the possibility of chain reaction where these neutrons collide with neighboring uranium atoms which themselves undergo the same reaction.

This has been practical since the conditions for nuclear fission to occurs are not difficult to reach and this reaction is occurring routinely around the world in various nuclear reactors. Although the most abundant form of uranium is U-238, U-235 is naturally occurring at 0.72% of uranium mineral. It is the only primordial fissile element known to exist. The bulk natural mineral can also be enriched by removing some of the U-238 to have a greater proportion of U-235, the more fissile of the two isotopes. In the process of achieving fission, it was quickly discovered that the binding energy per nucleon is minimized around Iron. For elements lighter than iron, binding energy per nucleon starts to increase again. It was then discovered that by binding lighter elements together such as hydrogen, the daughter elements were once again lighter than their parents causing the release of the difference as a great burst of energy. This process is known as nuclear fusion, and one of the more studied reactions is the following.

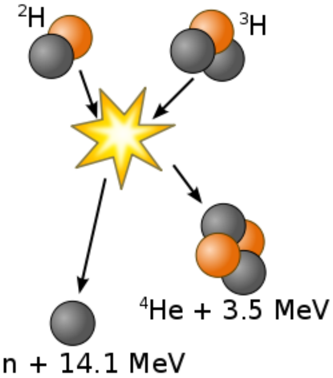

$$^2_1\mathrm{D} + ^3_1\mathrm{T} \rightarrow ^4_2\mathrm{He} + ^1_0\mathrm{n} \tag{1.17}$$

Where D and T are Deuterium and Tritium, the isotopes of hydrogen, respectively. This reaction yields a total of 17.6 MeV or 340 TJ/kg of DT fuel, a four fold increase over uranium fission.

Fusion is not without its problems however. In order for deuterium and tritium to fuse, the coulomb repulsion must be overcomed before the nuclear attractive force can take over. The conditions for this reaction to occur require extreme states of matter and temperatures of the order of 40 million kelvins at which point the kinetic energy of the hydrogen isotopes will be sufficient to overcome the repulsive electromagnetic force during a collision event and allow the nuclei to bind together through the attractive strong nuclear force. In nature, this type of reaction occurs in stellar matter such as young stars. Our Sun for example, is fueled by fusion since its enormous gravity forces the fuel to compress despite its high temperature so that the reaction will proceed. However, similar conditions have been incredibly difficult to achieve under laboratory conditions. There is an expression derived by John D. Lawson known as the “Lawson Criterion” which provides an estimated minimum figure of merit on the conditions for fusion to occur. It is expressed as

$$n_e \tau_e \geq L \equiv \frac{12}{E_{ch}} \frac{k_B T}{\langle \sigma v \rangle}. \tag{1.18}$$

where n_e is the electron density, and τ_e is the plasma confinement time. This provides a condition on the required confinement time and density of the plasma to achieve fusion and depends on the specific reaction. For the D-T reaction shown above, $n_e \tau_e \geq 1.5 \times 10^{20}$ s/m^3.

High intensity lasers have been seen as an attractive tool since their ultra-short energy delivery and resulting high energy flux allow for the production of such extreme temperatures and densities. The strong terabar pressures they apply and quick delivery of energy they provide makes them ideal candidates to study and ignite fusion reactions. Over the years, two major schemes have emerged as viable approaches towards reaching fusion using ultra-intense lasers: Inertial Confinement Fusion and Fast Ignition.

1.3.1 Inertial confinement fusion

Inertial confinement (see reference [23]) fusion has been one of the promising approaches to achieving nuclear fusion on a laboratory scale. The idea behind this technique is to use matter's own inertia (resistance to change motion) to confine the plasma. A series of high intensity lasers arranged in a spherical configuration are fired upon a small deuterium capsule. The energy supplied by the laser serves to heat up the capsule while the light pressure partially compresses the fuel to increase density. Fig. 1.3 shows the geometry of the capsule commonly used.

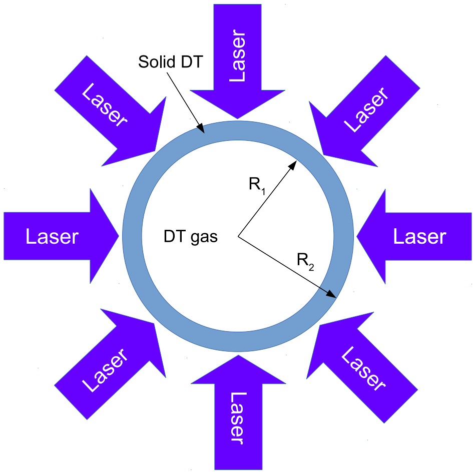

Figure 1.3: The capsule used for inertial confinement experiments consisting of a thin solid deuterium-tritium spherical shell filled with pure DT gas. Although variations on this geometry have been used over time, $R_1 \approx 1.7$ mm and $R_2 \approx 1.3$ mm.

As seen from this plot, the capsule which is placed in the center of a large chamber, is irradiated over 4π steradians from all directions. The idea is not necessarily to compress the capsule using the lasers, but to use the shell's inertia to compress the DT gas inside. The theory of ICF happens over several stages showed in Fig. 1.4. Upon initial contact by the lasers, the surface of the capsule is immediately heated to ultra high temperatures.

In a few nanoseconds, the hydrodynamical effects begin to occur in the guise of plasma ablation which causes the entire capsule to expand. This ablated mass carries momentum away from the capsule in a radially symmetric manner. In order for the momentum of the shell which started at 0 to be conserved, a certain amount of matter from the shell must be launched inward. The shell thus forms a shock, a discontinuity in the density which travels inwards at supersonic speeds. This convergence of shocks efficiently heats up the deuterium and tritium atoms it will pass through and will compress the DT gas to ~ 500 times its solid density and heat it to several millions of kelvin. At this stage of the process, the high density core is under immense pressure. The inertia of the shell however causes the core to enter the third phase known as stagnation. During this phase, a number of DT atoms will begin to fuse creating free energetic neutrons. If stagnation is long enough, the neutron production rate may increase to the point where the reaction is self-sustaining and then ignition will occur which is outlined by a burst of energy.

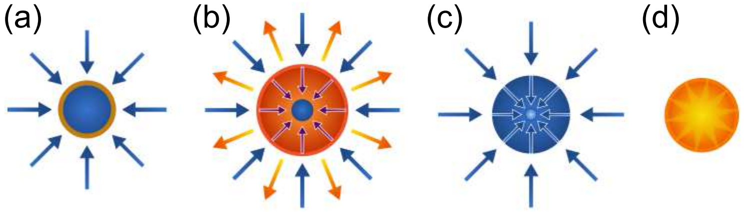

Figure 1.4: Different stages of ICF. (a) Ablation. (b) Shockwave formation. (c) Compression. (d) Ignition.

This particular variant of ICF is known as direct drive. Here, the lasers directly interact with the capsule to deposit their energy. Direct drive has the advantage that laser energy conversion into shock generation is very efficient. However, the tolerances for spherical symmetry for the laser-interactions are extremely narrow and any deviation in the form of shell imperfections or inhomogeneities in the laser energy deposition will cause the DT to fail to ignite. Additionally, one must contend with the complex interaction between a laser and an expanding coronal plasma. To circumvent these issues, another scheme has been proposed to help mitigate the strict symmetry requirements: indirect drive inertial confinement fusion. This method differs with direct drive by the use of a cavity in which the capsule resides, see fig. 1.5.

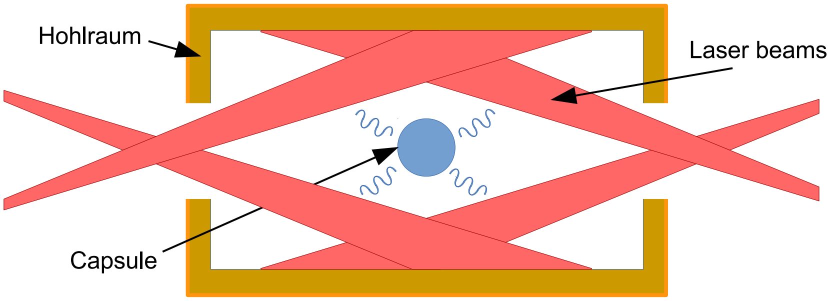

Figure 1.5: Schematic of the indirect drive inertial confinement fusion model. The gold hohlraum encases the capsule and serves as a radiation emitter to essentially cook the capsule using hard x-rays.

The cavity is known as a hohlraum and it is usually a small cylinder made of gold with two apertures on each end which serve as the entry point for the multiple laser beams. The idea is that instead of directly hitting the capsule with a megajoule of laser energy, the lasers beams are realigned to hit the interior of the hohlraum. As the interior surface of the cylinder reaches extreme temperatures, the gold plasma begins to strongly radiate which baths the cavity with x-rays. They eventually heat up the capsule which will ablate both externally and internally causing the gas to compress, heat up and ignite. The difference however is that since the x-rays are emitted omnidirectionally, the effective radiation profile which reaches the capsule is significantly smoothed which in principle will lead to a more symmetric implosion.

Even with the symmetry improvements of indirect drive, there are still significant technical issues associated with ICF. The capsule is plagued with many hydrodynamic instabilities while being heated to very high temperatures. These instabilities cause surface modulations which break the fragile symmetry needed to reach the Lawson criterion. The coupling between the lasers and the capsule core is also greatly reduced since much of the laser energy is converted into radiation which never reaches the capsule.

1.3.2 Fast ignition

With inertial confinement fusion, there is great difficulty in getting a symmetric implosion which will stagnate long enough for ignition to happen. In order to improve the efficiency of the coupling between the laser and the dense core, and relax some of the constraints on symmetry, a new concept was proposed which involved the injection additional energy to spark ignition. The idea is to begin with a spherical implosion using nanosecond laser pulses to begin the ablation and compression stage, but instead of going through a stagnation phase, a secondary short pulse ultra intense laser is used to inject energy as directly as possible into the core while the DT core is collapsed to its densest state. This concept is known as Fast Ignition [24].

With Fast Ignition experiments, the importance of the confinement time of the hot dense core is lessen. Whereas ICF requires a density of ≈ 1000 g/cm^3 at a temperature of 10 keV, fast ignition requires a lower density since a higher temperatures can be reached. With the secondary laser pulse, the temperature is expected to reach 12 keV which requires a much lower 300 g/cm^3 for ignition. The spherical laser apparatus is designed to begin the process of heating and compressing the DT capsule to values near the Lawson criterion, but the secondary laser is what brings the core to an energy-density regimes above the critical point.

There is however, a problem with this concept. As the capsule is being heated and compressed by the spherical lasers, a significant amount of plasma is ablated outward from the surface. This means the secondary ignition laser will not be able to directly deposit its energy at the core since the critical density point will usually be several hundred microns away from the core. Two ideas were proposed to overcome this issue: laser hole boring, and cone guiding. Fig. 1.6(a) demonstrates the concept of hole boring where a laser is used to “bore” a hole through the coronal plasma. The laser causes the plasma to be swept away forming a clear channel with little to no plasma blocking the core. This scheme is technically complex due to the requirement of a third laser apparatus with a relatively long pulse ($\sim$ 100ps) sustaining an intensity greater than 5×10^{18} W/cm^2 (ref. [25]. Once the channel has been bored, the ignition pulse is fired and free to reach the core uninhibited.

The second scheme is so called cone-guided fast ignition [26]. As seen in fig. 1.6(b), the capsule is placed around the tip of a gold cone. During the spherical implosion phase, the cone acts as a shield preventing the ablating plasma from entering the path of the ignition laser. The cone also acts as a guide. By moving the surface of interaction closer to the core,

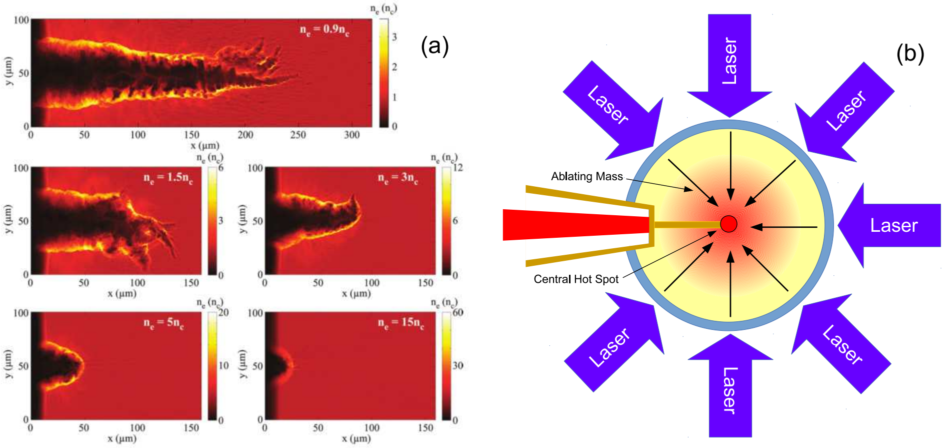

Figure 1.6: (a) Particle-in-cell simulation demonstrating laser hole boring for the application of fast ignition fusion. (b) Cone guiding scheme using a gold cone to move the ignition pulse interaction surface closer to the core.

the coupling between the laser and the core is improved.

The physics of fusion is quite complex as many parameters are involved and many physical processes are needed to describe the entire process from beginning to end. At each stage of energy transport, that is electron generation, transport and coupling, there are still many unknowns remaining before we fully understand the governing facts about laser-matter interactions. This present work will focus on electron generation and transport through solid media in order to better understand what determines the energy transport pattern under various conditions. To perform the study, a state-of-the-art particle-in-cell kinetic code is used to model laser-produced plasmas and specifically electron transport. The structure and features of the code are presented in Chapter 2 while Chapter 3 will present the results of the simulations.

1.4 Computational platform used

Kinetic modeling of plasmas is a computationally very expensive approach due to the sheer number of objects tracked during a simulation. For example, many simulations presented in Chapter 3 consists of hundreds of millions of particles which live in a large grid with over 10 million cells. The large number of objects that must be manipulated requires copious amounts of memory and computational power. To this end, a parallel computer is needed to improve the performance, especially for higher dimensions 2D and 3D simulations. The computer on which PICLS is used is named ARGO and has the following hardware specification:

1. CPU: AMD Bulldozer based Opteron 6272 operating at 2.1Ghz with 16 modular cores
2. CLUSTER: 50 cpus enclosed in 25 nodes for a total of 800 available cores
3. MEMORY: 2 gigabytes per core for a total of 1.6 terabytes
4. ETHERNET: 1 Gbit/s standard ethernet
5. OS: Rocks Clusters Linux 6.0 (64bit)
6. PARALLELIZATION: OpenMPI
7. STORAGE: 2 × 12TB network-attached-storage

Chapter 2

Modeling

2.1 Kinetic modeling

2.1.1 The particle-in-cell method

The premise of kinetic modeling lies in the fact that such models will describes plasmas in their most natural form. That is as a large collection of charged particles which generate electric and magnetic fields and in turn will interact with them, the so called collective effect. The Particle-in-Cell method is one of the multiple kinetic models used today to model non-linear/non-equilibrium plasma dynamics. It takes an intuitive view of a plasma buy describing it as a collection of particles in similar way as real plasmas exist. One of the key aspects of PIC modeling lies in its reliance upon fundamental physical relations which have been proven over the last centuries. At it's core, the model is derived from first principles and makes direct use of Maxwell's equations and Newtonian mechanics via the Lorentz force. The amount of kinetic energy typically found in plasmas means that relativistic corrections to the fundamental equations of motion are often incorporated. Sec. 2.2 will introduce extensions to the base particle-in-cell model such as the inclusion of methods to calculate inter-particle collisions as well as atomic processes in the form of dynamic ionization.

In reality, plasmas are comprised of an uncountable numbers of particles ranging of the order of Avogadro's number (6.02×10^{23}). Computers with enough memory or processing power to process that level of granularity do not yet exist. The fastest computers in the world are multiple orders of magnitude short of handling such a workload. To mitigate this problem, the PIC model introduces what are known as macro-particles. In this model, each macro-particle represents a very large collection of particles within a few orders of magnitude of $\approx 10^{15}$ particles per macro-particle. While macro-particles may be much larger in simulation size than physical particles, the charge-to-mass ratio must be consistent with the physical plasma. Even considering a very small physical system and an extremely large supercomputer, the ratio between real charged particles and macro-particles is many orders of magnitude. The goal is to choose a macro-particle ensemble which is statistically similar to the greater ensemble of real particles while using orders of magnitude fewer computational resources.

Particles in a plasma can both interact with an external field and interact with each other via electrodynamic interactions. However, even by using a reduced number of particles to represent a real plasma, solving Coulomb interactions directly between each pair of particles is computationally unfeasible since it amounts to computing N^2 operations per time step, where N is the number of macro-particles. In order to simplify and reduce the computation workload even further, the PIC model introduces the grid. The PIC paradigm then operates on the premise of using two distinct spaces to solve the equations of motion: the first space is that of the particles, and the second is that of the grid.

The particle space is used to store information relating to the particles: their position, momentum and charge state. To solve Maxwell's equations numerically, spatial resolution of the solution to Maxwell's equations must be finite. The grid space is used for this purpose. It is a spatial domain subdivided into a number of cells where the intersections of the vertices are used as coordinates to store information about the electromagnetic fields and current densities. The grid is geometrically overlayed over the particles such that particles are considered to be occupants of the cells. The 'Cell' part of the Particle-in-Cell monicker draws from the grid cells upon which approximations to Maxwell's equations are solved. The simulation region therefore consists of cells with particles occupying them. The process by which the Maxwell equations are solved and how particles interact with the fields will be detailed in a later section of this chapter. The particle-in-cell model can be described by the simple process of interactions of the macro-particles in a particle space with the electromagnetic fields solved in grid space. In essence, particles in a PIC simulation interact indirectly via a Particle-Cell-Particle process, rather than through direct electrodynamic particle-particle interactions [27]. Fig. 2.1 shows a pictogram of the basic components associated with PIC modeling.

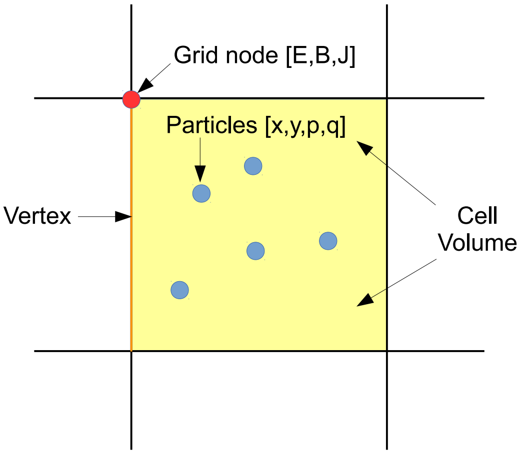

Figure 2.1: A pictogram depicting the dual space concept of PIC modeling. The particle space carries the particle-centric information of position, momentum and charge. The grid space stores the field and current information. The process of transferring information from grid space to particle space and back is iterative.

The particle-grid paradigm is ideally suited to accurately describe kinetic plasmas. In a plasma, the Debye length ($\lambda_D = \frac{v_{\text{thermal}}}{\omega_p}$) describes a volume outside of which electrodynamic forces will be shielded. That is, for a particle at the center of sphere of radius λ_D, it will only feel the effects from neighboring charged particles which lie within the sphere. Particles outside the Debye sphere do not exert any influence on the particle at the center. This means that the ideal scenario involves matching the grid size to the size of the collision-less plasma skin depth, $\frac{c}{\omega_p}$. Macro-particles then contribute their electromagnetic influence which is evaluated at the neighboring vertices of the grid, or at the edge of the Debye sphere. It is relevant to point out that Particle-Cell-Particle interaction process is not capable of resolving particles effects with a smaller scale than a grid size. For example, in the event that two particles cross paths, Coulomb forces between the two will be neglected by this scheme which would reduce the accuracy of the results. As such, the initial PIC technique was used to model hot collision-less plasmas where Coulomb interactions are negligible to begin with.

The process of discretizing Maxwell's equations to obtain field information at the grid nodes invariably introduces numerical error. For example, energy transfers between particles and grid points will introduce small errors which lead to energy not being rigorously conserved. This means the global energy of a simulation will artificially change due to small compounding numerical errors. This is known as 'numerical heating'. Fig. 2.2 shows an example of the energy evolution of a simulation which should be constant under ideal circumstances.

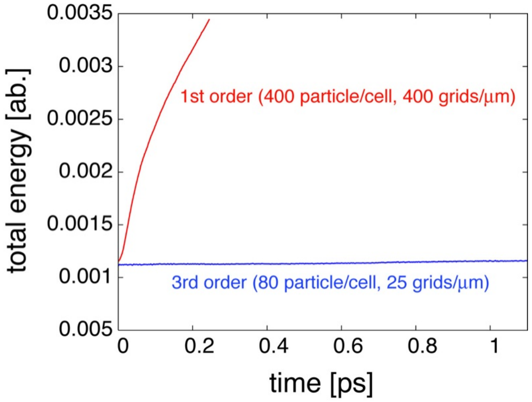

Figure 2.2: The internal energy of a solid density plasma initially at $T = 10\text{eV}$ increases with simulation time at a rate dependent upon grid size, macro-particle count and order of interpolation. Shown here, energy is much closer to being conserved using 3^{rd} order interpolation, even with a much larger grid cell size and a much smaller number of particles than 1^{st} order. A standard PIC simulation would require 1000 grids/μm to equivalently suppress numerical heating. [1]

There are several ways to reduce the impact of numerical heating. The first is to use a smaller grid size. With additional grid nodes for a given simulation spatial domain, the Maxwell equations will be solved over more nodes leading a smoother field profile. The second method to mitigate numerical heating is to include a greater number of particles per cell. Kinetic modeling originated from solving Vlasov equations using smooth distribution functions with ideal statistical representation of the realistic plasmas. Using additional particles for the PIC method will improve particle distribution statistics and lead to smoother density distributions. Field evolution and particle displacement also have a temporal aspect to them. Integrating the Lorentz force on the particles over a shorter time step will improve the accuracy of the current calculation which rely on particle motion. With smaller steps, the particle trajectories will be more accurately computed which results in better current density evaluation. Finally, an alternative technique to reduce numerical heating is to use better interpolation schemes.

Interpolation in this context is the process by which an extended field which is evaluated in particle space is then re-evaluated at a nearby point. The particles are responsible for generating the fields. However, recall that grid space is used to store field information. Since particle positions are not the same grid node position, the fields generated by the particles must be re-evaluated at the grid position. In the most basic fashion, a particle's electromagnetic influence is extended to the nearest grid node. This interpolation scheme carries the obvious flaw that a particle which is near the center of a cell may contribute only to the nearest grid node. At the next time step, the particle may shift in a different quadrant of a cell and its field contribution will instantly shift to a different node. As expected, this leads to discontinuities in field and contribute to numerical heating. In a different scenario, a particular cell may be spatially unbalanced with most of its resident particles falling in the same quadrant leading to a huge buildup of field contributions into a single grid node. This scheme is known as zeroth order interpolation of currents and serves only to demonstrate the concept of numerical heating caused by inaccuracy in current estimations from particle motion.

The next scheme extends the interpolation of the field to all grid nodes of a cell. This means the current contributions from a particle will be evaluated at two points in 1D simulations, four points in 2D and eight points in 3D. This is referred to as first order interpolation. Higher order interpolation can implemented as well and serve to reduce the discontinuities in the fields extrapolation. Fig. 2.3 depicts the various interpolation orders and their range of influence on the grid. Fig. 2.2 shows that increasing to third order interpolation can have a dramatic impact on energy conservation.

Increasing the interpolation order isn't without its caveat. The increase in the number of points where the fields must be evaluated for every particles will incur a performance

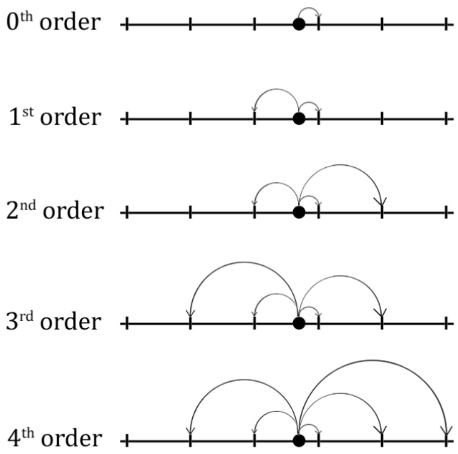

Figure 2.3: The interpolation orders and their range of influence for a 1D simulation grid. Higher order interpolation orders distribute current contributions to increasingly distant grid nodes.

penalty. However, the vector pipelines included in modern computer processors along with highly evolved compiler vector optimization can largely offset the increase cost of higher interpolation by effectively processing the distribution on multiple grid points simultaneously. Interpolation is a far more efficient method of reducing numerical heating due to modern computational design in comparison with decreasing cell size or increasing particle numbers.

Langdon [28] has demonstrated the success of the dual space approach to modeling kinetic plasmas. The paradigm of particle-in-cell modeling technique has been discussed above. We now continue with internal algorithms used in PICLS, a modern PIC code currently used.

2.1.2 Particle-in-cell iterative algorithm

There is a specific algorithm used in all particle-in-cell codes to self-consistently compute the plasma dynamics. At its most basic form, this is a four step process with two steps committed to computing equations of motions and Maxwell equations, and two steps involving the translation between particle and grid space. All steps are performed within a single time step (Δt) after which time is iterated by the specified increment.

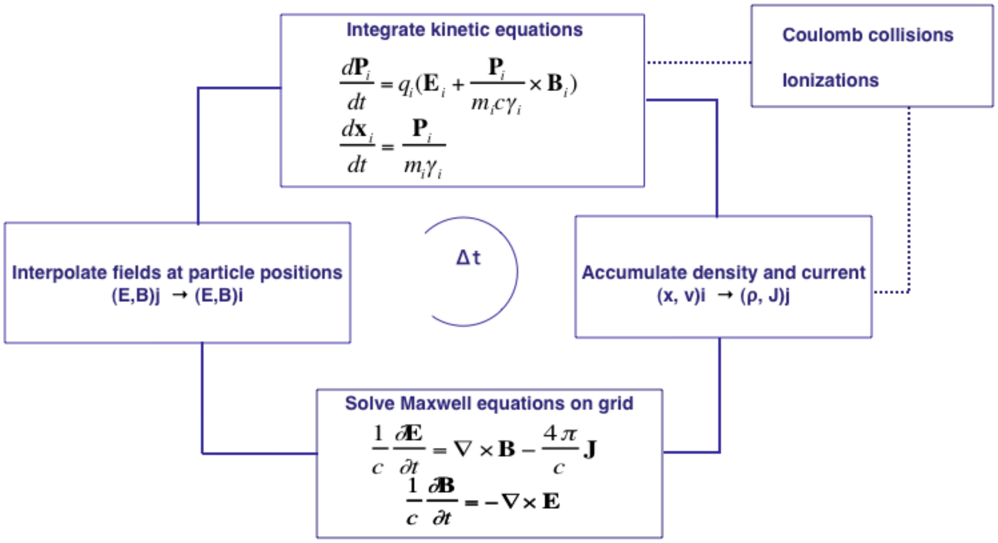

Figure 2.4: Generic particle-in-cell algorithm. The equations governing the particle trajectories are evaluated using four steps in a single time step.

The scheme depicted in Fig. 2.4 is an iterative process. The procedure is shown below with the added extensions to standard particle-in-cell model which will be discussed later in the chapter.

1. Integrate macro-particle kinetic equations from relativistically corrected Newtonian mechanics
2. Accumulate densities and currents at grid points using interpolation from macro-particle positions
3. Randomize and collide macro-particles with neighbors in the same cell
4. Evaluate ionization conditions and distribute any ionization product macro-particles
5. Solve Maxwell equations on grid using directionally split representation by shifting fields and accumulating currents
6. Interpolate fields at macro-particle positions using field solutions from grid
7. Increment simulation time and repeat

In PICLS, time and space are normalized to the laser period and wavelength respectively. Spatial resolution is typically defined as the number of grid points used to describe one laser period. In many of the simulations discussed in Chapter 3, a common value of 40 grid points per microns is typically used. Spatial resolution also sets temporal resolution. A 40grid/microns resolution also means a temporal resolution of 40 time steps/laser period. This leads to $\Delta t \approx 0.08$ fs for a 1 μm laser.

2.1.3 Solving Maxwell's equations

With the basic algorithm enumerated in the previous section, it is time to discuss the details of each step. We first start with the relativistically consistent Maxwell equations which are the most fundamental equations in classical electrodynamics. In vector form and unit system independent they are,

$$\vec{\nabla} \cdot \vec{E} = 4\pi k \rho \qquad \vec{\nabla} \cdot \vec{B} = 0$$

$$\vec{\nabla} \times \vec{E} = -g \tfrac{\partial \vec{B}}{\partial t} \qquad \vec{\nabla} \times \vec{B} = \tfrac{1}{gc^2} \left(\tfrac{\partial \vec{E}}{\partial t} + 4\pi k \vec{J} \right)$$

with the unit-system dependent constants [29],

Constant	CGS/Gaussian	SI/MKS
k	1	$\frac{1}{4\pi\epsilon_0}$
g	$\frac{1}{c}$	1

In particular, we focus on the curl equations. By solving those equations and by maintaining charge conservation in the simulation, we are implicitly solving Gauss' Law as well, as can be seen by taking the divergence of Ampere's Law.

$$\vec{\nabla} \cdot (\vec{\nabla} \times \vec{B}) = \frac{1}{gc^2} \left(\frac{\partial}{\partial t} \vec{\nabla} \cdot \vec{E} + 4\pi k \vec{\nabla} \cdot \vec{J} \right) = 0 \tag{2.1}$$

because of $\vec{\nabla} \cdot \vec{\nabla} \times = 0$, so that

$$0 = \frac{\partial \rho}{\partial t} + \vec{\nabla} \cdot \vec{J}. \tag{2.2}$$

The results is a basic current continuity equation. This of course dictates that charge must be conserved. The $\vec{\nabla} \cdot \vec{B}$ equation is satisfied so long as it is solved initially and all other equations are solved consistently throughout the simulation. We then proceed with a similar treatment of Faraday's law.

$$\begin{aligned}
\vec{\nabla} \cdot (\vec{\nabla} \times \vec{E}) &= -g\frac{\partial}{\partial t}\vec{\nabla} \cdot \vec{B} \\
\vec{\nabla} \cdot (\vec{\nabla} \times \vec{E}) &= 0 \\
\vec{\nabla} \cdot \vec{B} = \text{ constant } &= 0, \text{ if initially zero}
\end{aligned}$$

These results to the following conclusions. If the initial plasma's charge balance is globally neutral and the magnetic field is divergentless, the Maxwell equations stipulate that those features will remain at later times so long as the remaining Maxwell equations and the charge continuity equation are satisfied and no magnetic field divergence is externally introduced throughout the remainder of the simulation [30, 31]. A current conservation scheme detailed later in this chapter provides conformance with the continuity equation, allowing the remaining components to be resolved exclusively through the curl equations.

2.1.4 Directional splitting of Maxwell's equations

In there natural form, the Maxwell equations form a set of non-linear differential equations. There is a method known as 'directional splitting' which results in a modified set of linear equations. These equations are better suited to solving the electromagnetic fields in the grid space. Fundamentally, the Maxwell equations can be reformulated as wave equations which describe the propagation of light in vacuum. The wave equations are themselves not useful in there original form for the purpose of numerical integration. Based on the theory that any wave can be decomposed into two components, a forward traveling component and a backward traveling component, the electromagnetic wave equations can be decomposed into a pair of advection equations. These equations lend themselves well to numerical integration and will prove most useful to solve the electromagnetic fields on the grid. The matrix formalism for Maxwell's curl equations can be seen in Ref. [1]. This is most clearly stated by developing a matrix formalism for Maxwell's curl equations which can then be diagonalized, with a more straightforward solution available in the transformed basis.

$$\frac{\partial \vec{E}}{\partial t} - c\vec{\nabla} \times \vec{B} = \vec{J} \tag{2.3}$$

$$\frac{\partial \vec{B}}{\partial t} + c\vec{\nabla} \times \vec{E} = 0 \tag{2.4}$$

Faraday's Law is componentized,

$$\begin{aligned}
\frac{\partial \vec{B}}{\partial t} &= -c\vec{\nabla} \times \vec{E} \\
\vec{\nabla} \times \vec{F} &= \begin{bmatrix} i & j & k \\ \frac{\partial}{\partial x} & \frac{\partial}{\partial y} & \frac{\partial}{\partial z} \\ F_x & F_y & F_z \end{bmatrix} \\
\frac{\partial B_x}{\partial t} &= -c\left(\frac{\partial E_z}{\partial y} - \frac{\partial E_y}{\partial z}\right) \\
\frac{\partial B_y}{\partial t} &= -c\left(\frac{\partial E_x}{\partial z} - \frac{\partial E_z}{\partial x}\right) \\
\frac{\partial B_z}{\partial t} &= -c\left(\frac{\partial E_y}{\partial x} - \frac{\partial E_x}{\partial y}\right)
\end{aligned} \tag{2.5}$$

Ampere's Law is componentized,

$$\begin{aligned}
\frac{\partial \vec{E}}{\partial t} &= c\vec{\nabla} \times \vec{B} - 4\pi\vec{J} \\
\frac{\partial \vec{E_x}}{\partial t} &= c\left(\frac{\partial B_z}{\partial y} - \frac{\partial B_y}{\partial z}\right) - J_x \\
\frac{\partial \vec{E_y}}{\partial t} &= c\left(\frac{\partial B_x}{\partial z} - \frac{\partial B_z}{\partial x}\right) - J_y \\
\frac{\partial \vec{E_z}}{\partial t} &= c\left(\frac{\partial B_y}{\partial x} - \frac{\partial B_x}{\partial y}\right) - J_z
\end{aligned} \tag{2.6}$$

These equations are developed in preparation for a matrix formulation with 4π factored into $\vec{J}$ for brevity. For each Cartesian component, we get two equations, all six of which can be lined up into a matrix formulation with $\vec{F}^T = (E_x, E_y, E_z, B_z, B_y, B_z)$.

In the x-direction, using nomenclature $\partial q \rightarrow \partial_q$, Ampere's Law (2.3) becomes,

$$\begin{gathered}
(\partial_t \vec{E})_x - c(\vec{\nabla} \times \vec{B})_x = (\vec{J})_x \\
\partial_t E_x - c(\partial_y B_z - \partial_z B_y) = J_x .
\end{gathered} \tag{2.7}$$

Which can be written more explicitly in preparation for the matrix formulation as

$$\begin{aligned}
&\partial_t E_x \\
&+\partial_x(0E_x + 0E_y + 0E_z) + \partial_y(0E_x + 0E_y + 0E_z) + \partial_z(0E_x + 0E_y + 0E_z) \\
&+\partial_x(0B_x + 0B_y + 0B_z) + \partial_y(0B_x + 0B_y - cB_z) + \partial_z(0B_x + cB_y + 0B_z) \\
&= J_x
\end{aligned} \tag{2.8}$$

A parallel analysis results in a nearly identical form for Faraday's Law. Each equation can be written as one row in the matrix equation

$$\partial_t \vec{F} + \mathbf{A}\partial_x \vec{F} + \mathbf{B}\partial_y \vec{F} + \mathbf{C}\partial_z \vec{F} + \vec{J} = 0. \tag{2.9}$$

With $\vec{F}^T = (E_x, E_y, E_z, B_x, B_y, B_z)$ and $\vec{J}^T = (J_x, J_y, J_z, 0, 0, 0)$ and matrix definitions

$$\mathbf{A} \equiv \begin{pmatrix}
0 & 0 & 0 & 0 & 0 & 0 \\
0 & 0 & 0 & 0 & 0 & c \\
0 & 0 & 0 & 0 & -c & 0 \\
0 & 0 & 0 & 0 & 0 & 0 \\
0 & 0 & -c & 0 & 0 & 0 \\
0 & c & 0 & 0 & 0 & 0
\end{pmatrix} \tag{2.10}$$

$$\mathbf{B} \equiv \begin{pmatrix} 0 & 0 & 0 & 0 & 0 & -c \\ 0 & 0 & 0 & 0 & 0 & 0 \\ 0 & 0 & 0 & c & 0 & 0 \\ 0 & 0 & c & 0 & 0 & 0 \\ 0 & 0 & 0 & 0 & 0 & 0 \\ -c & 0 & 0 & 0 & 0 & 0 \end{pmatrix} \tag{2.11}$$

$$\mathbf{C} \equiv \begin{pmatrix} 0 & 0 & 0 & 0 & c & 0 \\ 0 & 0 & 0 & -c & 0 & 0 \\ 0 & 0 & 0 & 0 & 0 & 0 \\ 0 & -c & 0 & 0 & 0 & 0 \\ c & 0 & 0 & 0 & 0 & 0 \\ 0 & 0 & 0 & 0 & 0 & 0 \end{pmatrix} \tag{2.12}$$

In Eq. (2.9), the partial derivatives are independent. For the x direction,

$$\partial_t \vec{F} + \mathbf{A}\partial_x \vec{F} + \vec{J} = 0. \tag{2.13}$$

Maxwell's equations are identical in any right handed coordinate system, therefore the choice of the x component and its associated $\mathbf{A}$ versus (y, z, x) and (z, x, y) is arbitrary, allowing the ordered cycling of indices to reflect identical sets of equations in the y and z directions.

To efficiently solve these equations, the matrix $\mathbf{A}$ must be diagonalized by finding its eigenvectors and building the diagonalizing transform $\mathbf{L}^{-1}\mathbf{A}\mathbf{L}$,

$$\mathbf{L} \equiv \begin{pmatrix} 0 & 1 & 0 & 0 & 0 & 0 \\ 0 & 0 & -1 & 0 & 1 & 0 \\ 0 & 0 & 0 & 1 & 0 & -1 \\ 1 & 0 & 0 & 0 & 0 & 0 \\ 0 & 0 & 0 & 1 & 0 & 1 \\ 0 & 0 & 1 & 0 & 1 & 0 \end{pmatrix} \tag{2.14}$$

$$\mathbf{L}^{-1} = \frac{1}{2}\begin{pmatrix} 0 & 0 & 0 & 2 & 0 & 0 \\ 2 & 0 & 0 & 0 & 0 & 0 \\ 0 & -1 & 0 & 0 & 0 & 1 \\ 0 & 0 & 1 & 0 & 1 & 0 \\ 0 & 1 & 0 & 0 & 0 & 1 \\ 0 & 0 & -1 & 0 & 1 & 0 \end{pmatrix} \tag{2.15}$$

Diagonalizing $\mathbf{A}$,

$$\mathbf{A'} = \mathbf{L}^{-1}\mathbf{A}\mathbf{L} = \begin{pmatrix} 0 & 0 & 0 & 0 & 0 & 0 \\ 0 & 0 & 0 & 0 & 0 & 0 \\ 0 & 0 & -c & 0 & 0 & 0 \\ 0 & 0 & 0 & -c & 0 & 0 \\ 0 & 0 & 0 & 0 & c & 0 \\ 0 & 0 & 0 & 0 & 0 & c \end{pmatrix} \tag{2.16}$$

Evaluation will also require the quantity

$$\mathbf{A'}\mathbf{L}^{-1} = \frac{c}{2}\begin{pmatrix} 0 & 0 & 0 & 0 & 0 & 0 \\ 0 & 0 & 0 & 0 & 0 & 0 \\ 0 & 1 & 0 & 0 & 0 & -1 \\ 0 & 0 & -1 & 0 & -1 & 0 \\ 0 & 1 & 0 & 0 & 0 & 1 \\ 0 & 0 & -1 & 0 & 1 & 0 \end{pmatrix} \tag{2.17}$$

Left multiplying by $\mathbf{L}^{-1}$ and inserting $\mathbb{I} = \mathbf{L}\mathbf{L}^{-1}$, Maxwell's equations become

$$\begin{aligned} \mathbf{L}^{-1}\partial_t\vec{F} + \mathbf{L}^{-1}\mathbf{A}\mathbf{L}\mathbf{L}^{-1}\partial_x\vec{F} + \mathbf{L}^{-1}\vec{J} = 0, \\ \mathbf{L}^{-1}\partial_t\vec{F} + \mathbf{A'}\mathbf{L}^{-1}\partial_x\vec{F} + \mathbf{L}^{-1}\vec{J} = 0. \end{aligned} \tag{2.18}$$

The x equations are then, in vector form

$$\partial_t \begin{pmatrix} 2B_x \\ 2E_x \\ B_z - E_y \\ B_y + E_z \\ B_z + E_y \\ B_y - E_z \end{pmatrix} + c\partial_x \begin{pmatrix} 0 \\ 0 \\ -B_z + E_y \\ -B_y - E_z \\ B_z + E_y \\ B_y - E_z \end{pmatrix} + \begin{pmatrix} 0 \\ 2J_x \\ -J_y \\ J_z \\ J_y \\ -J_z \end{pmatrix} = 0 \tag{2.19}$$

Using the Levi-Civita pseudo-tensor $\epsilon_{ijk} = (+1, -1, 0)$ for cyclic, anti-cyclic and degenerate permutations of indexes i, j, k respectively [32]as well as an abstracted index notation for the Cartesian coordinates with one permutation provided as an example here,

$$\begin{pmatrix} i \\ j \\ k \end{pmatrix} = \begin{pmatrix} 1 \\ 2 \\ 3 \end{pmatrix} \to \vec{x} = \begin{pmatrix} x_1 \\ x_2 \\ x_3 \end{pmatrix} = \begin{pmatrix} x \\ y \\ z \end{pmatrix} \tag{2.20}$$

the bottom four equations in eq. (2.19) are

$$\left(\partial_t \pm c\partial_{x_i}\right)\left(B_{x_j} \mp \epsilon_{ijk} E_{x_k}\right) = \pm\epsilon_{ijk} J_{x_k} \tag{2.21}$$

Again, Maxwell's equations are identical in any right handed coordinate system. From Eq. 2.21, permuting indices provides additional equations in the direction of any cartesian axis.

Maxwell's equations are simplified under the combined representation. Continuing with the x component,

$$W^+ \equiv B_z + E_y \tag{2.22}$$

$$W^- \equiv B_z - E_y \tag{2.23}$$

$$V^+ \equiv B_y + E_z \tag{2.24}$$

$$V^- \equiv B_y - E_z \tag{2.25}$$

The bottom four equations in (2.19) are,

$$\partial_t \begin{pmatrix} W^- \\ V^+ \\ W^+ \\ V^- \end{pmatrix} + c\partial_x \begin{pmatrix} -W^- \\ -V^+ \\ W^+ \\ V^- \end{pmatrix} + \begin{pmatrix} -J_y \\ J_z \\ J_y \\ -J_z \end{pmatrix} = 0 \tag{2.26}$$

Or more succinctly,

$$\begin{gathered} (\partial_t \pm c\partial_x)W^\pm \pm J_y = 0 \\ (\partial_t \mp c\partial_x)V^\pm \pm J_z = 0 \end{gathered} \tag{2.27}$$

These equations are of the form

$$(\partial_t - c\partial_x)\, u(x,t) = v(x,t) \tag{2.28}$$

Applying time and space centered differencing

$$\frac{u(x,t+\Delta t) - u(x,t)}{\Delta t} - c\frac{u(x+\Delta x,t) - u(x,t)}{\Delta x} = v\left(x + \frac{\Delta x}{2}, t + \frac{\Delta t}{2}\right) \tag{2.29}$$

A condition for the solver is

$$\Delta t = \frac{\Delta x}{c} \tag{2.30}$$

which removes step size coefficients from all but the source term

$$u(x,t+\Delta t) - \cancel{u(x,t)} - u(x+\Delta x,t) + \cancel{u(x,t)} = v\left(x+\frac{\Delta x}{2}, t+\frac{\Delta t}{2}\right)\Delta t \tag{2.31}$$

Using the transform

$$t' = t + \frac{\Delta t}{2} \rightarrow t + \Delta t = t' + \frac{\Delta t}{2} \text{ and } t = t' - \frac{\Delta t}{2}, \tag{2.32}$$

the differenced advection equations become,

$$u(x,t') = u\left(x+\Delta x, t' - \frac{\Delta t}{2}\right) + v\left(x+\frac{\Delta x}{2}, t'\right)\Delta t \tag{2.33}$$

Equation 2.33 is the general form of the advection equations after modification for numerical integration applications. This formula computes new values at the next time step by adding an existing value of u to a value of v evaluated at the midpoint of the grid cell and shifting the resulting value by one grid cell. In other terms, the electromagnetic wave must be strictly copied by full grid cell which will guarantee the consistency of shape of the field as it propagates in space. The current is computed at a time and spatial midpoint and is accumulated in the advection direction. For the form,

$$\left(\partial_t + c\partial_x\right) u(x,t) = v(x,t) \tag{2.34}$$

a mirrored algorithm performs the same function, but shifting in the opposite spatial direction. The advantage of these advection equations is that each dimension can be treated independently which simplifies the solving of the fields in higher dimensions.

2.1.5 Current calculation

Current is generated as particles are displaced due to forces applied to them. The Maxwell solvers are used to approximate the current contribution by evaluating the motion of macroparticles in the PIC simulation. Current interpolation must be performed very carefully, however, since the plasma dynamics are very sensitive to small perturbations in current

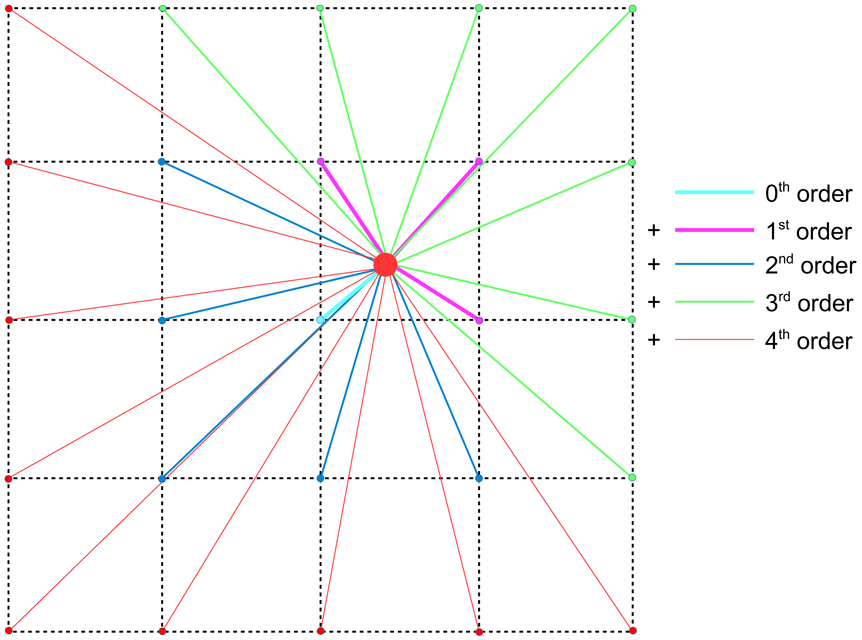

Figure 2.5: Interpolation of charge density from macro-particles at grid cell vertexes in zeroth (cyan), first (magenta), second (blue), third (green), and fourth (red) order.

density. Small inconsistencies may lead to rapidly growing numerical heating which may render simulation results void.

In order to avoid numerical heating, currents from macro-particles must be smoothly redistributed from one group of grid cell vertexes to another as the macro-particle moves through the simulation. High order interpolation may provide adequate smoothing by making electrons appear as smooth extended charged clouds.

Extending interpolation for two and three dimensions is as simple as considering the cell as an area (2D) or a volume (3D). Fig. 2.5 shows how interpolation is extended to 2D. Although conceptually simple, interpolation calculation for high order smoothing can be quite cumbersome. Work on interpolation is detailed in Buneman [31], and further formalized in Esirkepov [33].

In a zeroth order approximation with maximum reasonable numerical noise, the entire current of a particle can be applied to its nearest grid cell vertex (or in the case of this Maxwell solver, the grid cell midpoint). For a first order calculation with less abruptness in 1D, the particle can be considered a line segment of length equal to the cell size but centered on the particle position. Sliding this line segment with the direction and distance of particle travel in a single time step, the current contribution to the grid cell vertex overlapped by the line segment is proportional to the length of the line segment on the opposite side of the grid cell vertex from the macro-particle position. Fig. 2.5 illustrates this concept in two dimensions.

This must be normalized such that when the entirety of the line segment representing the macro-particle has passed fully across the grid cell vertex, the time integrated current contribution is equal to the representative charge of the macro-particle, regardless of particle velocity. Only in this way will the continuity equation be accurately solved, allowing the rest of the Maxwell solving machinery to avoid dealing with divergence solutions of fields which require long range calculations.

These current interpolation methods perform a charge density decomposition of the macro-particle into components contributing density/current to various grid cell vertexes. The interpolation of currents is effectively performed by distributing charge to grid cell vertexes both before and after the movement of a macro-particle, and then performing a subtraction to determine the differential current. Provided as example is the second order form polynomial distribution. In 1D,

$$S_i^{1D}(x) \qquad = \frac{3}{4} - (X_i - x)^2 \tag{2.35}$$

$$S_{i\pm1}^{1D}(x) \qquad = \frac{1}{2}\left(\frac{1}{2} \mp (X_i - x)\right)^2 \tag{2.36}$$

This is an array of bell-shaped charge density distribution functions centering on the macro-particle's coordinates (x, y, z). An analogous 3-dimensional function is,

$$S_{ijk}^{(3D)}(x, y, z) = S_i(x)S_j(y)S_k(z). \tag{2.37}$$

Of course, in the same way as the 1D treatment, similar functions are required for adjacent grid cells $(i \pm 1, j \pm 1, k \pm 1)$. This means a 3×3 matrix of functions represent the 2^{nd} order charge density distribution at nearest neighbor grid cell vertexes,

$$S_{ij} = S_i^{(1D)}(x_j), \quad i = \{-1, 0, 1\} \text{ and } j = \{1, 2, 3\}, \text{ with } x_j = (x_1, x_2, x_3) = (x_1, y_1, z_1) \tag{2.38}$$

However, for implementation purposes, the matrix used is 5 × 3 with the additional six elements,

$$S_{ij} = 0 \text{ for } i = \{2, -2\}, j = \{1, 2, 3\}$$

This is because the $\{\pm 2\}$ grid cells are out of the range of 2^{nd} order interpolation for the present, initial macro-particle position ($x_j = (x_1, y_1, z_1)$), but may be within the range of interpolation for the final macro-particle position ($y_j = (x_2, y_2, z_2)$). The charge density distribution interpolated from the final macro-particle position after moving through one time step is a similar 5 × 3 matrix,

$$T_{ij} = S_i^{(1D)}(y_j), \quad i = \{-1, 0, 1\} \text{ and } j = \{1, 2, 3\}, \text{ with } y_j = (y_1, y_2, y_3) = (x_2, y_2, z_2)$$

The normed difference $|\vec{x} - \vec{y}| = dx$ must be smaller than the grid cell size. In PICLS this requirement is guaranteed by the condition $\Delta x = c\Delta t$. This is required for the Maxwell solver, meaning in order for a macro-particle to move more than one grid cell size (Δx) in one time step (Δt), that macro-particle would require an unphysical velocity $|\vec{v}| > c$.

To determine the distribution of $\vec{J}$ rather than ρ, we require the differencing of the charge density distributions under motion. This can be accomplished by straightforward matrix subtraction,

$$\mathbf{D} = \mathbf{T} - \mathbf{S}.$$

The actual interpolation is quite involved,

$$W_{ijk1} = D_{i1}\left(S_{j2}S_{k3} + \frac{1}{2}D_{j2}S_{k3} + \frac{1}{2}S_{j2}D_{k3} + \frac{1}{3}D_{j2}D_{k3}\right) \tag{2.39}$$

$$W_{ijk2} = D_{j2}\left(S_{i1}S_{k3} + \frac{1}{2}D_{i1}S_{k3} + \frac{1}{2}S_{i1}D_{k3} + \frac{1}{3}D_{i1}D_{k3}\right) \tag{2.40}$$

$$W_{ijk3} = D_{k3}\left(S_{i1}S_{j2} + \frac{1}{2}D_{i1}S_{j2} + \frac{1}{2}S_{i1}D_{j2} + \frac{1}{3}D_{i1}D_{j2}\right) \tag{2.41}$$

with the actual three component current distribution at the grid cell vertexes,

$$\mathcal{J}^1_{i+1,j,k} - J^1_{i,j,k} = -q\frac{dx}{dt}W_{ijk1} \tag{2.42}$$

$$\mathcal{J}^2_{i,j+1,k} - J^2_{i,j,k} = -q\frac{dy}{dt}W_{ijk2} \tag{2.43}$$

$$\mathcal{J}^3_{i,j,k+1} - J^3_{i,j,k} = -q\frac{dz}{dt}W_{ijk3}. \tag{2.44}$$

In 4^{th} order interpolation, available in PICLS, the process is similar, except that further grid cells are accessible by interpolation, making the range fully $i = \{-3...3\}$ instead of effectively $i = \{-1...1\}$ as in 2^{nd} order, making the entire calculation much larger.

2.1.6 Solving particle motions

While fields are well defined at grid cell vertexes by PIC Maxwell solvers, finding the electrodynamics contributing to the acceleration of a macro-particle in a physical simulation space requires the interpolation or averaging of fields at grid cell vertexes to approximate the field experienced by the macro-particle.

This is effectively a cloud-cloud interaction. Both the fields at grid cell vertexes contributing to macro-particle accelerations and the current contributions from moving macro-particles at grid cell vertexes are smoothed by interpolation. This indirect mechanism also masks any direct particle-particle Coulomb interactions, thus no particle interactions are resolved at distances shorter than the grid cell size (generally the Debye length or $\approx c/\omega_p$).

A scheme that is similar in nature to interpolating macro-particle currents on grid cells, fig. 2.6, is used to approximate electric and magnetic fields at particle positions for use in solving particle motions. The appendix details the additional cost of higher order interpolation in higher dimensions.

For lasers of intensity $I = 10^{18}\text{W/cm}^2$ and higher, electron motion within the laser field becomes highly relativistic. Accurately simulating electron motion under the influence of such lasers requires a relativistic treatment of particle motion mechanics. Application of mechanics is a multi-step process,

1. Accelerate macro-particle $\frac{1}{2}$ time step (Δt) in the direction of the electric field $\vec{E}$ field

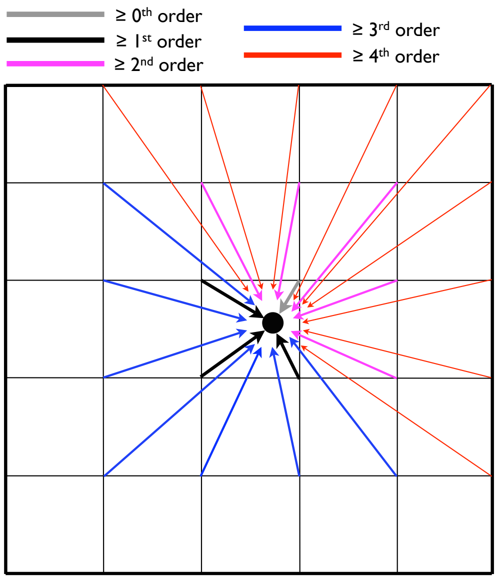

Figure 2.6: Interpolation of neighboring $\vec{E}$ and $\vec{B}$ fields at particle position in 2D. Different colors indicate at which order of interpolation fields from a particular grid cell contribute to the field at the particle position. Higher order interpolation becomes computationally very expensive in 3D. Weighting of contributions varies for each component with order of interpolation for proper normalization.

2. Rotate macro-particle momentum $\vec{p}$ based upon the small Lorentz force deflection angle estimated by $\vec{B}$ and $\vec{v}$ over time step Δt. (Note: This approximates a static magnetic field over the duration of the times step, which will not alter particle energy.)

3. Accelerate macro-particle $\frac{1}{2}$ time step (Δt) according to $\vec{E}$ field

This method is based upon the Boris scheme [34].

The magnetic field generates a small rotation angle through the duration of the time step.

$$\vec{\Omega} = \frac{q}{2mc}\frac{\vec{B}}{\gamma}\Delta t$$

with γ being the relativistic kinetic factor,

$$\gamma = \sqrt{1 + \frac{p^2}{c^2 m^2}}$$

The momentum of the macro-particle is rotated around the vector $\vec{\Omega}$ using a rotation matrix

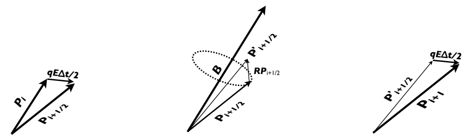

a) accelerate 1/2 step b) rotate about **B** c) accelerate 1/2 step

Figure 2.7: Macro-particle accelerations in the Boris scheme involve linear acceleration, rotation, and then linear acceleration.

based on Euler-Rodrigues,

$$\mathbf{R} = \frac{2}{1+\|\Omega\|^2}\begin{pmatrix} \frac{1}{2}(1+\Omega_x^2-\Omega_y^2-\Omega_z^2) & \Omega_x\Omega_y+\Omega_z & \Omega_x\Omega_z-\Omega_y \\ \Omega_x\Omega_y-\Omega_z & \frac{1}{2}(1-\Omega_x^2+\Omega_y^2-\Omega_z^2) & \Omega_y\Omega_z-\Omega_x \\ \Omega_x\Omega_z+\Omega_y & \Omega_y\Omega_z-\Omega_x & \frac{1}{2}(1-\Omega_x^2-\Omega_y^2+\Omega_z^2) \end{pmatrix}$$

The acceleration is performed by applying these steps in sequence, as depicted in fig. 2.7

$$\vec{P}_{i+\frac{1}{2}} = \frac{q\Delta t}{2}\vec{E} + \vec{P}_i$$

$$\vec{P}_{i+1} = \frac{q\Delta t}{2}\vec{E} + \mathbf{R}\vec{P}_{i+\frac{1}{2}}$$

2.2 PIC extensions: atomic processes

Early particle-in-cell schemes were focused on calculating charged particle kinetics under the exclusive influence of a local potential shaped by long range ($> \lambda_D$) electric and magnetic fields generated by neighboring charges. In reality, many other effects occur which influence the evolution of a plasma. For example, charged particles can directly interact with each other through the coulomb potential they inherently generate. Such interactions are known as collisions and may dramatically affect the current geometry. As such, the standard PIC model needs to be extended to compute the effect of collisions on plasma kinetics. A method to compute such collisions is detailed in the Collisions subsection of this chapter which simplifies the calculation by reducing the many body interaction to a sum of binary interactions. Also in this section is introduced the concept of weighted macro particles which can reduce numerical noise when few particles are used inside cells.

Since plasmas are inherently dynamic with rapidly changing thermodynamical conditions, the local state of a volume of plasma will change over time. For example, as plasmas are heated or cooled, the temperature range can be such that the average charge state of its constituents may vary over time. This temporal aspect of the charge state of a plasma was not taken into account by early PIC models. These models did not attempt to explain how charged particles or global charge state of the plasma evolved over time or how the charge distributions came to be in the first place. In essence, the atomic processes of material ionization and recombination were neglected to simplify the computations for the modest hardware available. In the regime where a plasma is of sufficiently low density and sufficiently hot, neglecting these atomic processes can be an adequate approximation. However, high density plasmas involve processes which allow the charge state to evolves over time as energy is either injected, ejected or spatially redistributed through various atomic mechanisms. In fact, ionization physics may dominate the dynamics under certain conditions. For such plasmas, the standard PIC method must further be extended by including ionization models. Three models are discussed below which are included in PICLS. Two of the models presented below are used to compute collisional based ionization. Their realm of validity applies to different types of plasmas due to a differing range of approximations included in them. The first is the Thomas-Fermi equilibrium ionization model and the second non-equilibrium impact ionization model. The third model applies to ionization induced by strong electric fields. This model is known as electron field or tunnel ionization.

2.2.1 Collision model

Modeling ultra-intense laser-plasma interactions also requires simulating the collisional nature of plasmas, particularly for regions where particle energies are temporarily far from equilibrium. By way of example, a 100 TW, sub-picosecond laser pulse can drive the temperature of a micron scale solid foil target to 1 keV, while large swathes of electrons are distributed not in the Maxwellian distribution indicative of this temperature, but rather in a distribution with two or more clear, distinct temperatures [2]. This scenario includes extremely large density gradients reaching from sub-critical densities ($n < 10^{21}\mathrm{cm}^{-3}$) to many times more than solid density ($n > 10^{25}\mathrm{cm}^{-3}$). As a result, during the energy transport in laser-plasma interactions from sub-critical to extremely high densities, the Coulomb collisions requires an accurate treatment. Individually weighted macro-particles are used to simulate extremely dense regions where equally weighted particles would become impossible. However, collisions between particles of different weights must be handled carefully to conserve energy and momentum either exactly or statistically.

A collision model using equally weighted particles was first described by Shanny et al. [35]. This was extended to exactly conserve non-relativistic momentum and energy in multi-component plasmas by Takizuka and Abe [36]. A relativistic correction was subsequently introduced by Sentoku [37]. Monte-Carlo techniques were introduced by Miller and Combi [38]and extended to unequal particle weights by Nanbu and Yonemura [39]. These Monte Carlo approaches were limited in that energy and momentum were conserved in aggregate, yet it is advantageous to use fewer particles per cell in Particle-in-Cell simulations than would allow for proper statistical conservation of energy and momentum.

There are several restrictions on cell size relevant to modeling macro-particle collisions and ionizations

- Grid size should coincide with the Debye length, such that collisions are performed between particles within a Debye sphere, similarly to the physical model of collisions in plasma. The Debye sphere masks fluctuations in fields, preventing collisions between particles separated by more than the Debye length.
- Temperature and density gradient scale lengths must be much larger than grid cell size to make averages used in collision frequency calculations meaningful.
- In order to be relatively free from statistical error, cell size should be large enough to encompass a sufficient quantity of macro-particles.

For particle α, the collision term is a sum of integrals over the phase spaces of every

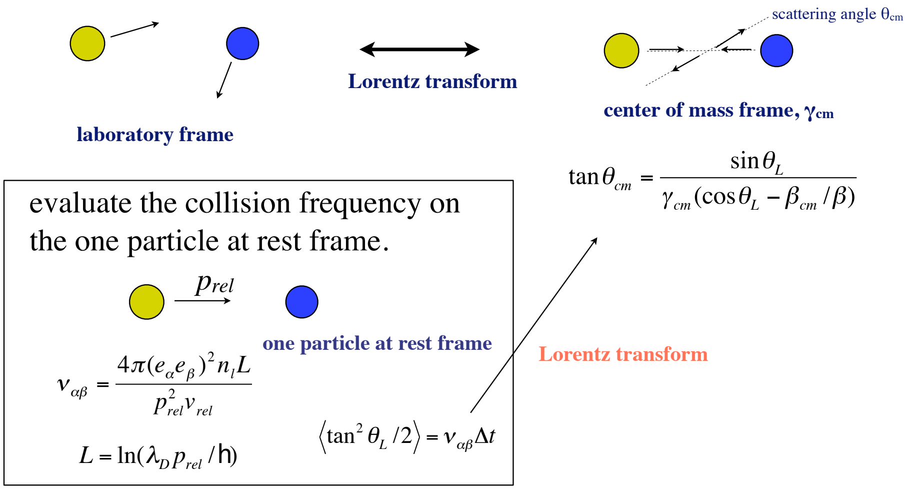

Figure 2.8: Binary collisions are performed in a 3-step process. [2]

other particle with which it can collide. Non-relativistically this is,

$$(\partial f_\alpha t)_{coll} = -\sum_\beta \partial v_j \frac{e_\alpha^2 e_\beta^2 \lambda}{8\pi\epsilon_0^2 m_\alpha} \int d\vec{v}' \left[\frac{\delta_{jk}}{u} - \frac{u_j u_k}{u^3}\right] \left[\frac{f_\alpha}{m_\beta} \partial f_\beta(\vec{v}') v_k' - \frac{f_\beta(\vec{v}')}{m_\alpha} \partial f_\alpha v_k\right] \quad (2.45)$$

with e_i, m_i, f_i being the charge, mass, and phase distribution of particle i [36]. By resolving enough particle collisions through random pairings, these integrals are solved via the Monte Carlo method by random pairing of binary collisions.

Collision operations are performed in a sequence of frames of reference as described below and graphically illustrated in Fig.2.8 for each pair.

1. Transform into rest frame of one macro-particle
2. Calculate collision frequency and scattering angle from local environment (density, temperature, etc.)
3. Transform scattering angle and macro-particle momenta into center-of-mass frame
4. Calculate final momenta
5. Transform macro-particles back into simulation frame

2.2.2 Ionization by Thomas-Fermi model (equilibrium model)

The Thomas-Fermi model is a statistical model of the atom which allows for the prediction of the local average ionization degree of a plasma based on the inter-atom spacing and medium temperature. In this model, the individual atoms are represented as spheres and the electrons are treated as a quasi-classical Fermi gas under the influence of the Coulomb potential shaped by neighboring charges. Fundamentally, this model predicted what is known as pressure ionization. Namely, the principal factor in determining the equations of state was the atomic density. For very high densities, the average atomic spacing would be much smaller thus raising the Coulomb potential above the ionization threshold. If this condition occurred, an electron would be stripped from its orbital and become a free particle. In the original Thomas-Fermi model, the temperature of the material was assumed to be 0 and the effects of exchange forces between particles were neglected. This means that the atoms' and electrons' kinetic energy was not taken into account in calculating the pressure on an atom exerted by its neighbors. For this model, the material is modeled as a large collection of atoms represented as spherical cells as seen in Fig. 2.9.

The volume of each cell is determine by the density of the medium and is assumed to be equal to the average available space to each ion. The electrons on the other hand are modeled as a quasi-classical Fermi gas which permeates the material. The idea is that this collection of charges form self-consistent Coulomb potentials which then act on the electron gas. Under the right conditions, the magnitude of the potentials can reach levels which exceed the ionization potential threshold where electrons are stripped from the permeating gas to become free particles. Feynman, Metropolis and Teller were amongst the first to lay the pioneering ground work and achieve the first set of equations of state for the Thomas-Fermi model [40].

As explained above, the temperature of the medium is assumed to be zero and exchanges forces are neglected in the most basic version of the model. As such, the potential formed by the charged distribution depends solely on the atomic distribution of the material. Since the density is assumed to be identical for all atoms and the pressure on a specific atoms is assumed to be isotropic, that is spherically symmetric, we can write the following relationship

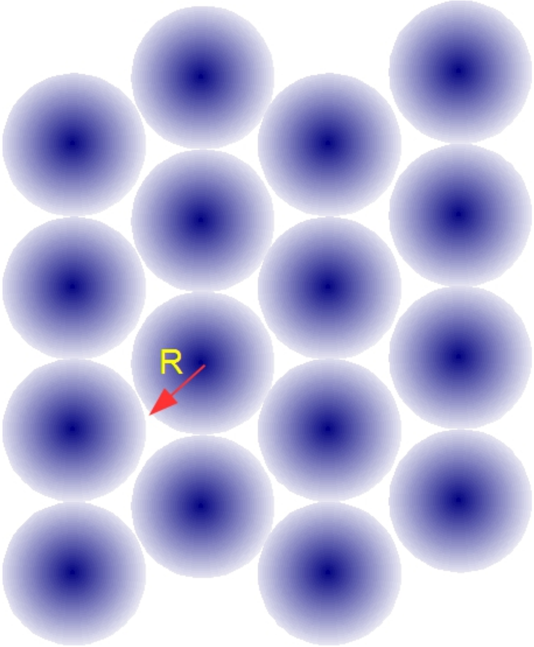

Figure 2.9: Example of a 2D distribution of atoms according to the Thomas-Fermi model. Each sphere contains exactly 1 atom and its radius is R which is determined by the average density of the medium and therefore the average afforded volume for each atom.

linking the density and potential using the Poisson equation.

$$\frac{1}{e}\nabla^2 V(r) = -4\pi e n(r) \tag{2.46}$$

Since we assume spherical symmetry, we may discard all but the radial components of the Laplace operator.

$$\frac{1}{e}\frac{1}{r^2}\frac{d}{dr}\left(r^2\frac{dV(r)}{dr}\right) = -4\pi e n(r) \tag{2.47}$$

We then make a variable substitution such that $V(r) = \frac{E_0}{e} - \frac{Ze^2}{er}\phi$ where $r = \mu x$. This leads to the following relation

$$\phi = \frac{(E_0 - eV)}{Ze^2}\mu x. \tag{2.48}$$

Here, E_0 is the maximum total energy. By imposing the assumption that there is a connection between kinetic energy and electron density, it is possible to be able to write the following series of calculations.

$$E = T + V \tag{2.49}$$

$$T = E - V \tag{2.50}$$

$$\frac{{p_0}^2}{2m} = E - V \Rightarrow {p_0}^2 = 2m(E - V) \tag{2.51}$$

$$\rho_e = \frac{8\pi}{3h^3}{p_0}^3 = 8\pi/3h^3\,[2m(E - V)]^{3/2} \tag{2.52}$$

Here, ρ_e is the electron density, V the potential, m the electronic mass and E the total energy. We then substitute Eq. 2.48 in to Eq. 2.47 along with the expression for ρ_e to obtain a differential equation of the form

$$\frac{d^2\phi}{dx^2} = \frac{64\pi^2 e^2 m\sqrt{2mZe^2}}{3h^3}\frac{\mu\sqrt{\mu}}{\sqrt{x}}\phi^{\frac{3}{2}} \tag{2.53}$$

Since μ is still undefined, it is a practical consideration to assume

$$\mu\sqrt{\mu} = \frac{3h^3}{64\pi^2 e^2 m\sqrt{2mZe^2}} \tag{2.54}$$

Which leads to $\mu \equiv a_0(9\pi^2/128Z)^{\frac{1}{3}}$. We are then left with a non-linear differential equation of the form

$$\frac{d^2\phi}{dx^2} = \frac{\phi^{\frac{3}{2}}}{x^{\frac{1}{2}}}, \tag{2.55}$$

which is known as the Thomas-Fermi equation. Here, x is the distance from the center of the nucleus measured in units of μ which corresponds to the atomic radius. In this context, a_0 is the classical Bohr radius for hydrogen. To solve this equation, a numerical approach is taken. The boundary conditions are as follows.

$$\phi(0) = 1 \;;\; \frac{d\phi}{dx} = \frac{\phi}{x} \quad \text{at} \quad x = 1 \tag{2.56}$$

$$: \phi = 1 + a_2 x + a_3 x^{\frac{3}{2}} + a_4 x^2 + \cdots \tag{2.57}$$

This series solution's leading coefficient, a_2, seeds the shape of the potential solution

Table 2.1: Coefficients of the series solution to the Thomas-Fermi equation

$$a_3 = \frac{4}{3}$$
$$a_4 = 0$$
$$a_5 = \frac{2}{5}a_2$$
$$a_6 = \frac{1}{3}$$
$$a_7 = \frac{3}{70}{a_2}^2$$
$$a_8 = \frac{2}{15}a_2$$
$$a_9 = \frac{2}{27} - \frac{1}{252}{a_2}^3$$
$$a_{10} = \frac{1}{175}{a_2}^2$$
$$a_{11} = \frac{31}{1485}a_2 + \frac{1}{1056}{a_2}^4$$

as every following coefficient depends upon its value as seen in table 2.1. Depending on the initial slope of the potential, solutions for free atoms, bound atoms and ions can be obtained.

In order to make use of the solution to the Thomas-Fermi equation, it must be reshaped in terms of real thermodynamic variables. To achieve this, the application of the virial theorem can be useful. This theorem states that for a closed stable system of particles, there is a relation between the kinetic energy and the total energy according to $2 < T >= \sum_{k=1}^{N} < \vec{F_k} \cdot \vec{r_k} >$ where $\vec{F_k}$ is the force applied to the k-th particle at position $\vec{r_k}$. This allows for the formulation of an expression connecting the pressure of the system to the internal energy.

$$\frac{3}{2}Pv = E_{kin} + \frac{1}{2}E_{pot} \quad \text{where} \quad v = \frac{4\pi}{3}(\mu x_0)^3 \tag{2.58}$$

Here P is the pressure, v the volume, E_{kin} and E_{pot} are the kinetic and potential energy respectively. This leads to the pressure being expressed as

$$Pv = \frac{e}{15}\frac{Z^2e^2}{\mu}{x_0}^{\frac{1}{2}}{\phi_0}^{\frac{5}{2}}(x_0). \tag{2.59}$$

Later iterations of the model have extended the realm of applicability beyond the restricted set of conditions imposed by the original model. The Thomas-Fermi was eventually extended to apply to small temperatures using a perturbation approach described by Marshak and Bethe [41]. Richard Latter presented an extended version of the model to apply to arbitrary temperatures [42]. In this method, the electron density ρ_e is no longer an expression which depends on the potential alone as in eq. 2.52. Since electrons are fermions, they must obey the Pauli exclusion principle. This has the consequence that single particle quantum states can only be occupied by a single electron at a time. In the context of a non-zero temperature environment, the electrons distribution will have a tendency to partition itself in a certain manner. For $T = 0$, it was assumed that all quantum states up to the maximum momentum were occupied. When temperature increases however, the electron distribution will change as well and take on the form of what is known as the Fermi-Dirac distribution

$$\overline{n}_i = \frac{1}{e^{\epsilon_i - \mu/kT} - 1}. \tag{2.60}$$

Here, $\overline{n}_i$ is the probability of finding a particle in state 'i', ϵ_i is the energy associated with state 'i', k is the Boltzmann constant and T the absolute temperature. It is then possible to recover the spatially dependent electron density by

$$\rho_e(\vec{r}) = \frac{8\pi}{h^3} \int_0^\infty \frac{p^2 dp}{e^{[-\alpha + p^2/2m - eV(\vec{r})]/kT} - 1} \tag{2.61}$$

With equation 2.61, a pressure can be obtained by again using the Poisson equation and carrying out the derivation

$$P = \frac{ZkT}{V} \frac{2}{9} \frac{a}{\phi(0)} I_{\frac{3}{2}}[\phi(1)] \tag{2.62}$$

where $\phi(r/r_0) = [\alpha + eV(r)]r/kTr_0$, $a = (r_0/c)^2$ and $1/c = 4\pi e(2m)^{\frac{3}{4}}(kT)^{\frac{1}{4}}/h^{\frac{3}{2}}$. Here $I_{\frac{3}{2}}[\phi(1)]$ is the integral

$$I_{\frac{3}{2}}[\phi(1)] = \int_0^\infty \frac{y^{\frac{3}{2}} dy}{e^{(y - \phi(1))} + 1}. \tag{2.63}$$

The Thomas-Fermi model has so far led to the calculation of pressure for two sets of initial assumptions. The derivations presented above are meant to provide insight on the link between pressure and the free electron density. Here, the pressure is defined as the transfer of momentum between external electrons and electrons internal to one of the atom-spheres introduces as the basic building block of the model. Since there is a direct link between electron distribution density and the pressure as shown in the equations above, it follows that varying the external pressure, either through a mechanism which increases density or by injecting energy and thus raise the temperature, will have an impact on the electron distribution. The density equation 2.61 allows for thermal excitation and ionization of bound electrons. This process is known as pressure ionization and is an important factor in computing plasma dynamics.

More *et al.* from Ref. [43] derived what is know as the Quotidian Equation Of State (QEOS) model. This model is a general purpose EOS model for hydrodynamic plasmas which include contributions by ions to the thermodynamical quantities: Helmholtz free energy, total energy, entropy, chemical potential, pressure and free electron number per ion. The latter is of particular importance since this quantity is highly dynamical in the context of plasmas. Again, the Fermi pressure can be written as

$$p_e = n(R_0) k_B T \frac{I_{3/2}(\mu/k_B T)}{I_{1/2}(\mu/k_B T)} \tag{2.64}$$

where $n(R_0)$ is the electron density at the boundary of the atom. This can be written as

$$n(R_0) = 2 I_{1/2}(\mu/k_B T)/{\lambda_{th}}^3. \tag{2.65}$$

Since density is the number of particles per unit of volume, multiplying the density by the volume of one atom will give Q, the number of free electron per atom as

$$Q = \left(\frac{4\pi {R_0}^3}{3}\right) n(R_0). \tag{2.66}$$

This result assumes that Z=1. One of the features of the semi-classical Thomas-Fermi model is its capacity to scale to any material. If $Q_1(\rho_1, T_1)$ is the solution for hydrogen, then the scale solution $Q(Z, \rho, T) = Z Q_1(\rho_1, T_1)$ where $\rho_1 = \rho/AZ$ and $T_1 = T/Z^{4/3}$. Here A is the atomic number of the element of interest. It is then possible to construct a solution for the number of free electrons per atom which is derived in Ref. [44].

$$Q(Z, \rho, T) = Z \frac{x}{1 + x + \sqrt{1 + 2x}} \tag{2.67}$$

In the above expression, Q was obtained by fitting of the equation of state (EOS). The term

x in Eq. 2.67 is given as

$$x = \alpha \left[\left(\frac{\rho}{ZA_m} \right)^C + A^C \left(\frac{\rho}{ZA_m} \right)^{BC} \right]^{\beta/C} \tag{2.68}$$

here A_m is the atomic mass, ρ is the ion mass density in g/cm^3, T_e is the electron temperature in eV and

$$A = a_1 \left(\frac{T_e}{Z^{4/3}} \right)^{a_2} + a_3 \left(\frac{T_e}{Z^{4/3}} \right)^{a_4} \tag{2.69}$$

$$B = -exp \left[b_0 + b1 \left(\frac{T_e}{T_e + Z^{4/3}} \right) + b2 \left(\frac{T_e}{T_e + Z^{4/3}} \right)^7 \right] \tag{2.70}$$

$$C = c1 \left(\frac{T_e}{T_e + Z^{4/3}} \right) + c2 \tag{2.71}$$

where, $\alpha = 14.3139$, $\beta = 0.6624$, $a_1 = 3.323 \times 10^{-3}$, $a_2 = 0.971832$, $a_3 = 9.26148 \times 10^{-3}$, $a_4 = 3.10165$, $b_0 = -1.7630$, $b_1 = 1.43175$, $b_2 = 0.315463$, $c_1 = 0.366667$ and $c_2 = 0.983333$.

This equation is quite useful for the implementation in hydrodynamic codes and PIC-hybrid codes. This fitting function takes only two inputs, density and temperature which can be extracted from the code. However, since laser-plasma interactions typically yield non-Maxwellian temperature distributions with two distinct electron populations, the calculation for temperature in the laser-plasma interaction must be performed with certain assumptions. Although there is no clear boundary between bulk electrons and hot electrons, a distinction must be artificially introduced to mitigate the skewed effect of including super relativistic electrons in the energy pool for the temperature calculation. Typically the value of 10 keV is used as the boundary temperature between bulk and hot electrons. This means electrons above the threshold will be discarded when calculating the temperature since electrons falling in this category will be less collisional and thus not contribute to the local thermodynamics. Note that the ionization dynamics are not sensitive to this value of '10 keV' as seen in Ref. [3].

The process of ionization inside the code simply follows the predictions by the fitting function. The density is extracted by adding all the particles' weight within a cell and divide by the cell volume. The temperature is extracted from the average kinetic energy of the particles within one cell. Then a predicted ionization level is computed from Eq. 2.67. If the ion's current charge state Z_i is lower than the predicted ionization degree $Z(T_e, \rho)$, and if local thermal energy is greater than the required ionization energy $\bar{I}$, then ionization is performed by using eq. (2.72) [45] and the particle weight. A corresponding electron is introduced in the system with zero initial energy at the ion position. $\bar{I}$ is computed as

$$\bar{I} = I_0 \frac{\exp\left(1.29\, r^{(0.72-0.18\, r)}\right)}{\sqrt{1-r}} \tag{2.72}$$

where $I_0 = (10\mathrm{eV})Z$ and $r = Z_i/Z$ also Z_i and Z are current charge state and atomic number, respectively. Eq. (2.72) estimates the ionization energy which translates to the average energy of all bounded electrons of charge state Z_i within a single cell in the context of the particle-in-cell simulation paradigm. For example, Fig. 2.10(b) plots the actual ionization energy (red curve) corresponding to ionization degrees for gold. The ionization degree approximated by the TF model is shown by the green curve, which is smooth in nature, but note that the total of the ionization energy for each level $\sum_0^{79}(E_{Z+1} - E_Z)$ is similar in both predictions.

To ensure energy is conserved during the process of ionization, we subtract the ionization energy from the bulk electrons while excluding fast electrons. The merit of using the TF model is a relatively low computational cost since only the average charge state is computed as opposed to the charge state of each ion. It has been observed, in general, that the Saha model is twice more computationally expensive than TF, however this will also depend on the target material and other simulation parameters. A model using the Saha equation is able to compute the charge state distribution in each cell, although it is computationally expensive. At non-relativistic intensity regime, both the TF model and the Saha model agree well with experimental observations in terms of the average charge state distribution in ultra-fast heated material by a short pulse (see Ref. [46] for more details).

In addition to ionization, the Thomas-Fermi also has another useful feature. The equations of state which govern the pressure at a certain density and temperature assume the

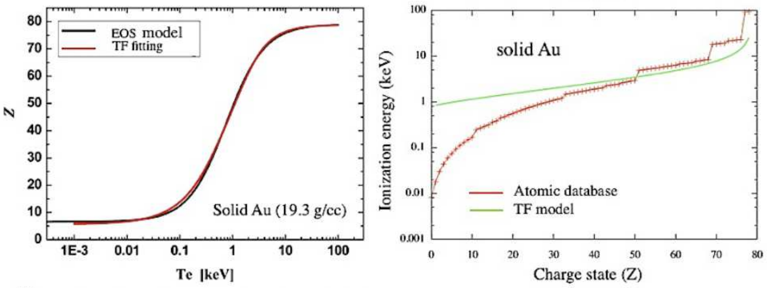

Figure 2.10: (a) Average ionization degree as a function of temperature for solid gold from EOS database (red) and TF fitting (black). (b) Average ionization energy for gold (Z=79) given by atomic data base (red curve) and by Thomas-Fermi model (green curve). See ref. [3]

system at hand is in thermodynamic equilibrium. Since atomic processes are probabilistic in nature, this implies that processes and their reverse can occur at any time. For a certain set of conditions, one side may be favored at the expense of the other. As the environmental conditions of a system change, so will the balance between the two opposing atomic processes. The balance between the atomic processes is governed by sets of atomic rate equations. Although the scope of the topic exceeds that of this present work, one additional aspect requires mention. The processes of interest in the context of kinetic modeling of plasmas are that of collisional ionization, and its opposite process known as three-body recombination. That is the process by which two free electrons interact with each other while under the influence of an ion. One electron transfers energy to the other which can lead to the first electron recombining to the ion in lower energy bound states while the second electron remains free. For almost any plasma conditions, both processes are occurring simultaneously. When the temperature and density increase, ionization is favored and the average charge state will increase as well. In return, when the plasma cools, the rate of recombination increases favoring a lower average ionization level. The Thomas-Fermi model does account for the dual process nature of ionization in the predicted ionization levels it computes. The ionization values it predicts are equilibrium values when both ionization and recombination have stabilized to a constant rate.

There are limitations in the implementation of this model in PICLS. As long as energy is being deposited by the laser and the plasma is still heating, the code will correctly model the ionization degree predicted by TF. There are strict requirements for the conservation of charge and current for collective behavior of the plasma to be self-consistent and as long as newly ionized electrons are added to the system, the self-consistency is easily maintained. When a new free electron is born, it is placed at the exact overlapping position as the ion from which it originates. This means charge is rigorously conserved at the position of the ion since the total local charge at the position of the ion does not change between immediately before and immediately after the ionization event. Also, the new electron is assigned no momentum so it does not contribute any current. Since no current is added to the system, current is also rigorously conserved. The opposite process has posed significant challenges in its implementation due to difficulty in rigorously observing charge and current conservation. Specifically, when the plasma cools and the TF model predicts that three-body recombination will begin to dominate leading to a decreasing average ionization state, the code does not self-consistently model the recombination process. This is due to the difficulty in conserving charge and current when removing electrons as they recombine. After inter-particle dynamics are computed and particles under the action of the fields are displaced, electrons and ions no longer share the exact same positions. So when an electron which is found suitable for recombination is suddenly removed, a discontinuity in the spatial charge distribution and therefore in current density is observed. Attempts have been made to implement three-body recombination based on the predicted TF ionization values, however severe numerical heating has been observed resulting from the charge and current discontinuities. Since a solution resolving the numerical instabilities resulting from recombination has not yet been found, our code does not perform recombination when the plasma state reaches a cooling state.

The Thomas-Fermi model can lead to the calculation of ionization surfaces over density and temperature domains. For informational purposes, these surfaces have been plotted to show the expected values over the relevant temperature-density domain in fig. 2.11. The plots are those of the specific elements pertaining to simulations which will presented in Chapter 3.

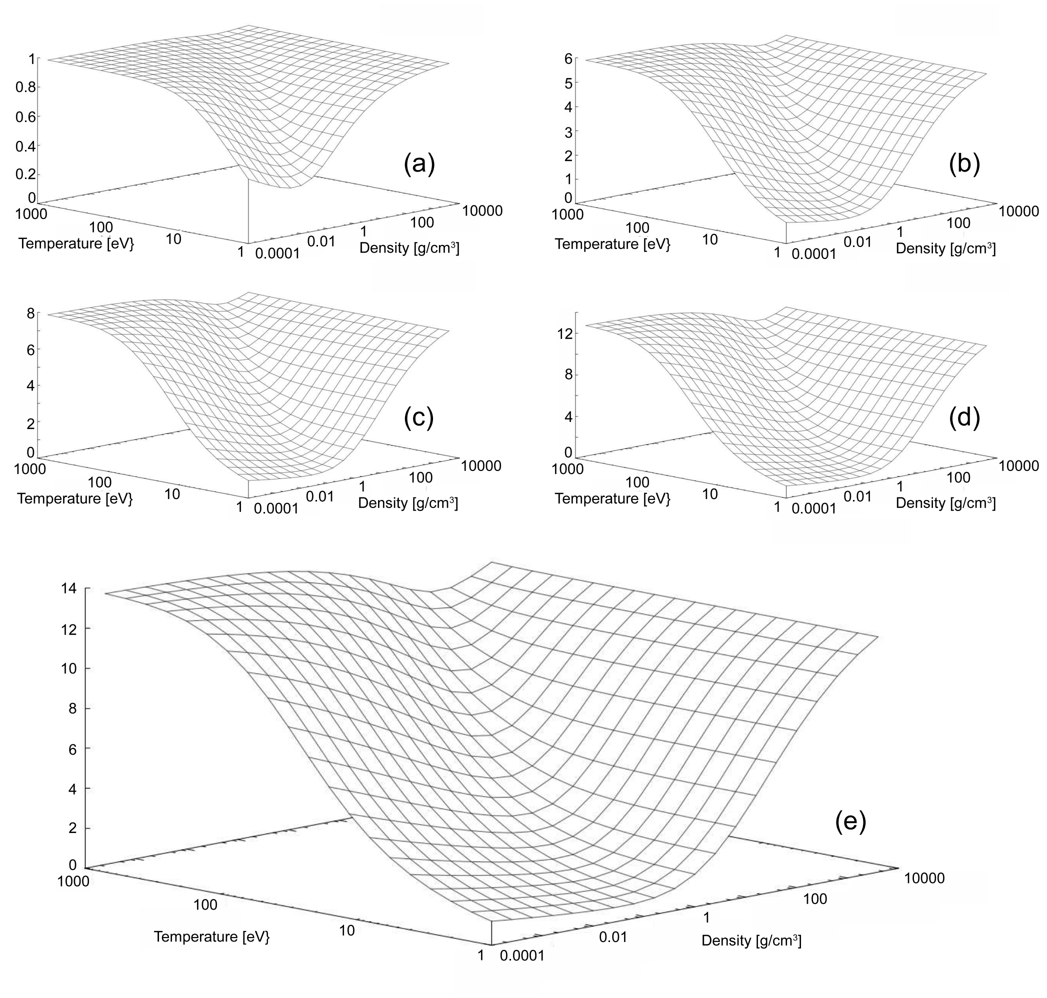

Figure 2.11: A log-log plot over wide temperature and density domains of the Thomas-Fermi model's ionization prediction $\bar{Z}$ for (a) hydrogen, (b) carbon, (c) oxygen, (d) aluminum and (e) silicon.

2.2.3 Ionization by electron impact model

The Thomas-Fermi model described in the previous section assumes that the plasma conditions are near thermal equilibrium. For laser-produced plasmas where many of the physical processes involved take place on sub-picosecond scales, this assumption is incorrect. In such plasmas, more than one electron populations with completely independent energy distributions will coexist locally. To address this problem, an impact ionization model based on electron-ion collisional cross sections has been explored and implemented in PICLS. The pioneering works on impact ionization modeling was done by A. Kemp *et al.* [47]. We follow a similar procedure but in computationally less expensive way. By establishing an electron-ion collisional pair, and taking into account the energy of the incoming electron as well as the ionization state of the ion, a cross section of ionization can be derived. The formula was derived by Lotz [48] and is shown below.

$$\sigma = \sum_{i=1}^{N} a_i q_i \frac{\ln(E/P_i)}{EP_i}\{1 - b_i \exp[-c_i(E/P_i - 1]\}. \tag{2.73}$$

Here, E is the energy of incoming electron, P_i is the binding energy of the i-th subshell, q_i is the number of electrons in subshell i, and a_i, b_i and c_i are free parameters determined from experimental measurements. These values are provided by Lotz and are shown in table 2.2 as a reference. Using Eq. 2.73 the average cross section in each cell is obtained as

Table 2.2: Constants a, b, and c of the empirical formula for different shells. The quantity n is the principal quantum number and is equal to 4, 5, 6, or 7 for the s shell; equal to 4, 5, or 6 for the p shell; equal to 5 or 6 for the d shell; equal to 4 or 5 for the f shell. Constant a is given in 10^{-14} cm^{2}eV^2

	1s	1s^2	2p	2p^2	2p^3	2p^4	2p^5	2p^6	3d	3d^2	3d^3	3d^4	3d^5	3d^6	3d^7	3d^8	3d^9	3d^{10}
a	4	4	3.8	3.5	3.2	3.0	2.8	2.6	3.7	3.4	3.1	2.8	2.5	2.2	2.0	1.8	1.6	1.4
b	0.60	0.75	0.6	0.7	0.8	0.85	0.90	0.92	0.6	0.7	0.8	0.85	0.90	0.92	0.93	0.94	0.95	0.96
c	0.56	0.50	0.4	0.3	0.25	0.22	0.20	0.19	0.4	0.3	0.25	0.20	0.18	0.17	0.16	0.15	0.14	0.13
	2s	2s^2	3p	3p^2	3p^3	3p^4	3p^5	3p^6	4d	4d^2	4d^3	4d^4	4d^5	4d^6	4d^7	4d^8	4d^9	4d^{10}
a	4	4	4	4	4	4	4	4	4	3.8	3.5	3.2	3.0	2.8	2.6	2.4	2.2	2.0
b	0.3	0.5	0.35	0.40	0.45	0.50	0.55	0.6	0.3	0.45	0.6	0.7	0.8	0.85	0.90	0.92	0.93	0.94
c	0.6	0.6	0.6	0.6	0.6	0.5	0.45	0.4	0.6	0.5	0.4	0.3	0.25	0.20	0.18	0.17	0.16	0.15
	3s	3s^2	np	np^2	np^3	np^4	np^5	np^6	nd	nd^2	nd^3	nd^4	nd^5	nd^6	nd^7	nd^8	nd^9	nd^{1}0
a	4	4	4	4	4	4	4	4	4	4	3.8	3.6	3.4	3.2	3.0	2.8	2.6	2.4
b	0	0.3	0	0	0.2	0.3	0.4	0.5	0	0.2	0.3	0.45	0.6	0.7	0.8	0.85	0.90	0.92
c	0	0.6	0	0	0.6	0.6	0.6	0.5	0	0.6	0.6	0.5	0.4	0.3	0.25	0.20	0.18	0.17
	ns	ns^2	nf	nf^2	nf^3	nf^4	nf^5	nf^6	nf^7	nf^8	nf^9	nf^{10}	nf^{11}	nf^{12}	nf^{13}	nf^{14}		
a	4	4	3.7	3.4	3.1	2.8	2.5	2.2	2.0	1.8	1.6	1.4	1.3	1.2	1.1	1.0		
b	0	0	0.6	0.7	0.8	0.85	0.90	0.92	0.93	0.94	0.95	0.96	0.96	0.97	0.97	0.97		
c	0	0	0.4	0.3	0.25	0.20	0.18	0.17	0.16	0.15	0.14	0.13	0.12	0.12	0.11	0.11		

$$\bar{\sigma}_{ion} = \frac{n_i}{N_e} \sum_{j}^{N_e} \sigma_j(\bar{Z}, E_j) v_{ej}, , \tag{2.74}$$

here n_i is the ion density in the cell, N_e is the number of electrons in the cell, E_j and v_{ej} are electron energy and speed, respectively. Note here that we use the average ionization degree $\bar{Z}$ in the cell and avoid the individual pairing to boost the calculation speed. Otherwise the evaluation of the probability of ionization must be done $N_{ion} \times N_e$ times where N_{ion} and N_E are the numbers of ions and electrons per cell respectively. Using the average cross section, the ionization probability is obtained by

$$P_{ion} = 1 - \exp(-\bar{\sigma}_{ion}\Delta t), \tag{2.75}$$

here Δt is the simulation time step. We increase ionization degree by '1' for each ion randomly when its random number r satisfies $r \geq P_{ion}$ as long as the local kinetic energy is greater than the required ionization energy. This is consistent with the Monte-Carlo approach since the process will be repeated a large number of times ensuring the ionization is distributed evenly amongst all ions in a cell. To ensure energy is conserved, we reduce local kinetic energy by distributing a momentum reduction to all local electrons within a cell equivalent to the ionization energy. This method allows to calculate ionization values in much more natural manner by directly taking inter-particle interactions which mirrors more closely the multi-particle nature of real plasmas. The impact model should allow for improvements in accuracy in non-equilibrium plasmas, such as relativistic laser produced plasmas. Of importance to the validity of this model is the fact that impact ionization only calculates the cross-section for ionization. The process of three-body recombination is separate process and requires its own set of cross-sections which at this time are not included in PICLS. As such, the code may only increase ionization when conditions are satisfied, but the electrons that were freed in the process will remain free even if the plasma cools down. This is in contrast with the Thomas-Fermi model which includes the contributions to ionization from recombination. As mentioned in the previous section, the code does not perform recombination when the plasma cools down. However, the contribution of recombination is small during the heating phase for intense laser-matter interactions, but nevertheless present at all times even when the plasma is ionizing. Indirectly, the process of three-body recombination is partially accounted for in the code when using the TF model while the target is being heated. When impact ionization is used, three-body recombination is completely neglected since it is a separate process with a unique set of cross-sections.

In essence, an approximation is assumed that for very intense laser-matter interactions, recombination is negligible such that impact ionization which only computes ionization, can predict average local ionization levels of a non-equilibrium plasma. To test the validity of this assumption, a fully self-consistent impact ionization model complete with recombination capability will have to be implemented. This remains a future endeavor. The cross-section for each species computed from the Lotz formula is plotted in Fig. 2.12.

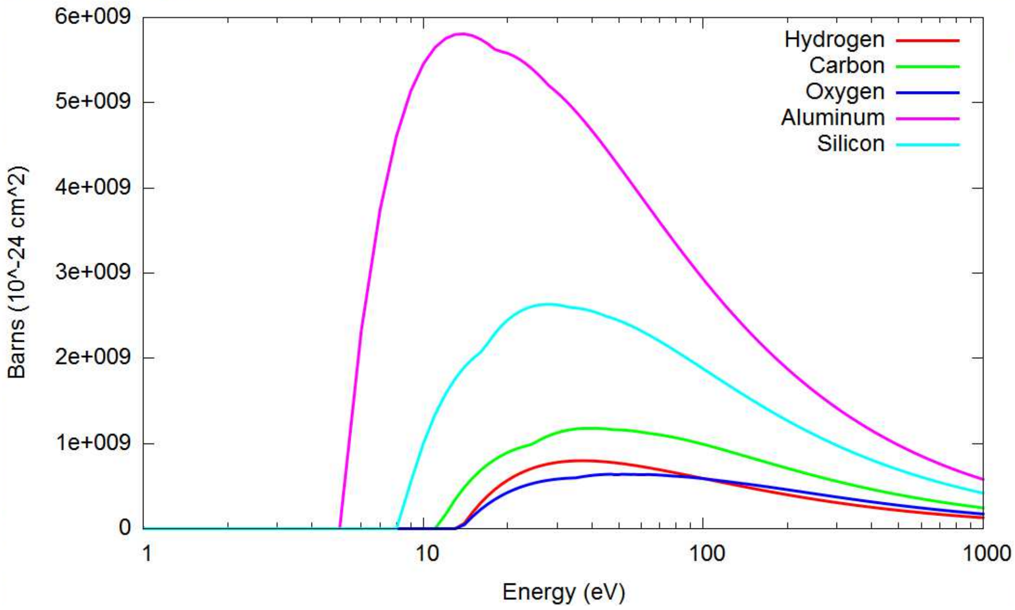

Figure 2.12: The cross section for the first ionization degree for the 5 elements used in the simulations in chapter 3 as a function of incoming electron energy. The peaks of these curves vary between ≈10 and 50 eV and correspond to the impact electron energy with the greatest likelihood of initiating ionization.

2.2.4 Tunneling Ionization

The final topic covered in this chapter is that of tunnel ionization. This physical phenomena is of key importance to laser-plasma interactions since without its implementation, fully self-consistent simulations of laser-produced plasmas would be impossible. In order to perform the most accurate simulation possible to benchmark against experimental results, one must begin with the same set of conditions present in the laboratory. That is, as experimental physicist must begin with cold neutral materials, so should the initial simulation conditions reflect cold matter. This poses a problem for energy transport simulations that rely on collisional ionization alone. In the event of high intensity laser-matter interactions, ions or atoms absorb very little energy from the ponderomotive pressure applied by the laser. The vast majority of the energy that is absorbed is done so by the orbiting electrons. However, cold matter has no free electrons present to act as an absorbing medium. Instead, electrons are generated by a different ionization process: field ionization.

Fig. 2.13(a) shows a basic diagram of the concept behind tunnel ionization. A high intensity laser pulse will present upon the incident surface a very large electric field computed as (see Ref. [49])

$$I = \frac{1}{2}\epsilon_0 c|E|^2 \Rightarrow E = \sqrt{\frac{2I}{\epsilon_0 c}} \tag{2.76}$$

Here, I is the laser intensity in W/m^2, ϵ_0 is the permittivity of free space equal to 8.854×10^{-12} F/m, c is the speed of light 3.0×10^8 m/s and E is the electric field in V/m. If we choose a laser intensity of 1.0×10^{18} W/cm^2, the threshold of relativistic laser interactions, the electric field computed is $E = 2.7 \times 10^{12}$ V/m. A field of this magnitude will reshape the Coulomb potential of a bound electron by lowering the external potential barrier. This will allow the electron to tunnel through the now finite potential barrier and become free as seen in Fig. 2.13(b).

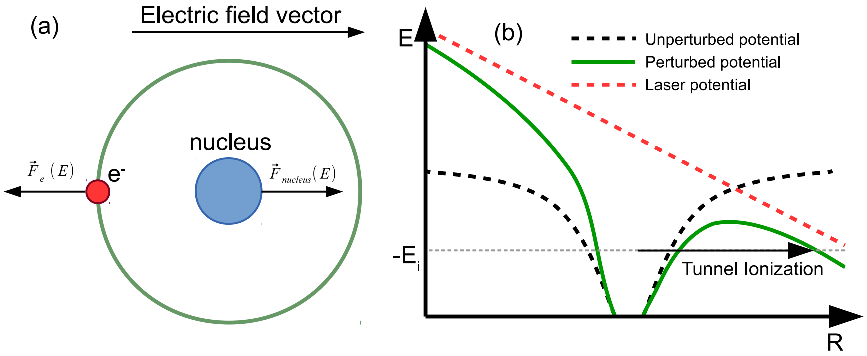

Figure 2.13: (a) A basic force diagram depicting the opposing forces felt by the positive nucleus and negative electrons when subjected to an electric field. (b) An externally applied electric field has the effect of lowering the potential barrier to values below the electron ionization potential allowing it to tunnel out to the continuum.

In the code, an ionization rate equation based on Landau and Lifshitz's treatment in Ref. [50] is used. Work by Kato *et al.* to adapt the Landau formalism to form a tunnel ionization rate equation which depends on the electric field alone is presented in Ref. [51]. This equation is written as

$$W_i[E_L(t)] = 4\omega_a \left(\frac{\epsilon_i}{\epsilon_\hbar}\right) \frac{E_a}{E_L(t)} exp \left[-\frac{2}{3}\left(\frac{\epsilon_i}{\epsilon_\hbar}\right)^{3/2} \frac{E_a}{E_L(t)}\right]. \tag{2.77}$$

Here, $\omega_a = me^4/\hbar^3$, $E_a = m^2e^5/\hbar^4$, ϵ_h and ϵ_i are the ionization potentials of hydrogen (13.6 eV) and of the "i-th" element under study, respectively, and $E_L(t)$ is the magnitude of the electric field perturbing the atom. Then the probability of tunnel ionization occurring becomes

$$P_{fi} = 1 - e^{-W(E_L(t))\Delta t}. \tag{2.78}$$

Since tunneling is a probabilistic event, a random number between 0 and 1 is generated for the atom being subjected to an electric field. If P_{fi} is greater than this number, ionization will proceed. An electron is then added with no momentum at the position of the atom and the charge state of the ion is incremented by one. When tunnel ionization is significant, the energy drain spent on ionization must be accounted for. This is done through the implementation of ionization currents. These currents are added to simulate ohmic power dissipation equivalent to the ionization energy (ref. [52])

$$EJ_{ioniz} = \sum_k W_k N_k \epsilon_k \tag{2.79}$$

with W_k the average ionization rate in a sinusoidal field, N_k the electron density and ϵ_k the ionization potential. The ionization current then becomes

$$J_{ioniz}{}^{(i)} = \frac{U_p{}^{eV}}{|E_{norm}{}^2|\Delta t} E^{(i)} \tag{2.80}$$

Once an electron has tunneled and has been freed, it will feel the strong ponderomotive pressure from the laser and then be accelerated inside the target. Collisional ionization then becomes important as electrons transfer radiation energy into kinetic energy as they become the main carriers of energy in the target. Without field ionization, electrons would not be produced and therefor very little of the laser energy would be absorbed. In the following chapter, a different mechanism where tunneling ionization becomes important in plasma dynamics besides direct heating by the laser will be introduced.

Chapter 3

Simulations

The study of electron transport in solid materials as a result of ultra-intense laser interactions has been an important topic in high energy density physics. Applications of laser-produced plasmas are numerous since the dynamics of such plasmas are governed by many types of physical processes. Lasers have long been leading candidates to achieve nuclear fusion, one of the major endeavors long associated with high energy density physics. However, other applications in the medical field have gained traction in recent years since they can also employ lasers to produce various sources of particles and light by adhering to the same principles of intense laser-matter interactions. By nature, laser produced plasmas have the common element that laser light is consequently absorbed and converted into kinetic energy by electrons. Hence the study of electron transport is of paramount importance to understand the dynamics of a laser produced plasma.

Experimentally, these plasmas have posed many challenges since they usually involve extreme conditions which pose problems on the level of diagnostics. First, the timescales of these plasmas are usually very short ranging from femtoseconds to nanoseconds. For such timescales, it can prove difficult or impossible to capture a detailed time evolution of the physical effects involved. Second, the energies reached by certain classes of lasers can produce a broad range of radiation spectrum and particles energies which exceed the sensitivity and resolution of a single detector. This can be partially mitigated by using multiple detector types to capture more information, but this can be impractical for specific experimental conditions. Lastly, when studying laser-matter interactions with optically thick opacity profiles, the only information that can be captured is that which leaves the surface of the target under study. The interior of the target and thus the bulk of the plasma dynamics which are responsible for radiation and particle transport remain uncharted unless radiographic techniques are used.

In order to complement experimental data and mitigate some of limitations to potentially gain additional insight on laser-plasma interactions, modeling of the plasmas can be used to better understand the internal dynamics and physical processes. In this chapter, a series of simulations are presented which study various aspects of laser-plasma interactions with emphasis on ionization and electron transport physics. The first topic presented is on ionization physics in glass targets with specific emphasis on the ionization speed, geometry and underlying drivers. Then, the role of the collisional ionization model on affecting the transport dynamics is studied. A comparison between the local thermal equilibrium Thomas-Fermi model and the non-equilibrium Impact model is presented. Finally, a study of the resistivity and its role in shaping the electron transport is detailed for the third set of simulations. A transport guiding condition is derived from basic assumptions and the result benchmarked against simulation results.

3.1 Insulator ionization modeling

3.1.1 Experimental premise

High intensity laser-plasma interactions are immensely complex. The physics involved is usually highly non-linear which makes predicting and understanding the behavior of such plasmas very difficult. The transport effects as well as the process by which certain materials ionize when subjected to intense laser radiation are not well understood. To begin the process of understanding how materials transition into plasmas, an experiment conducted at the Nevada Terawatt Facility was performed in order to study the process of ionization in insulator materials [53, 54].

The target material chosen for the experiment was Silicate glass. This material has clear advantages since it is optically transparent in the visible regime at room temperature. This allows the use of diagnostics such as shadowgraphy and interferometry which employ lasers as backlight sources to monitor the transmission of the target during the transition from solid to plasma. As the target ionizes, the free electrons generated will cause the low intensity laser to be absorbed by the process of inverse Bremsstrahlung and then scattered isotropically. The more free electrons there are, the greater the absorption which directly leads to reduction in transmitted laser light. Cameras sensitive to the particular wavelength of the backlight source can then measure the amount of light coming through the target and determine the boundaries of the plasma by the location where the light transmission begins to decrease. The experiment was conducted using the 50 TW Leopard laser at the University of Nevada, Reno. The laser parameters for the experiment were as follows: wavelength $\lambda = 1057$ nm, pulse length $\tau \approx 0.4$ ps, beam energy between 1.4 and 10 J and the focal spot of $\sim 15\mu$m. This yields a beam intensity $I = 2 \times 10^{18}$ W/cm^2. Fig. 3.1 shows the result of the experiment at two different times demonstrating the propagation of the ionization wave inside the target. It is gathered from these results that the ionization wave expands with a hemispherical geometry and retains its shape for several picoseconds. Using the multi-frame data and the axial profile of the absorption of the backlight laser to define the position of the ionization front where the shadowgraphy light signal begins to drop from base values (i.e. values measure before the beginning of the laser interaction), it is then possible to calculate the average speed of the propagation of the ionization wave. For a laser

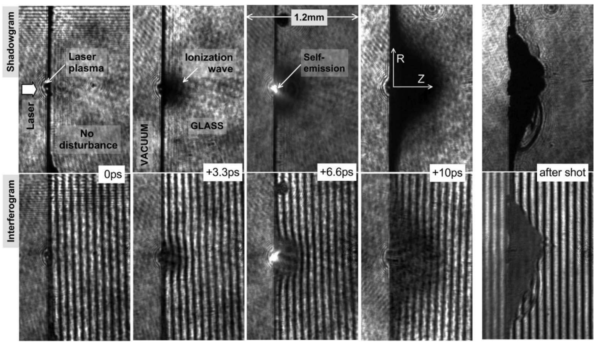

Figure 3.1: Captured image of the ionization wave in a 1.1 mm thick BK7 glass target. The spatial resolution was 15 μm with an exposure time of 0.4 ps.

intensity of 2×10^{18} W/cm^2, the speed of ionization was measured to be $\sim c/3$ or $\sim 30\%$ of the speed of light. See Ref. [54] for a detailed description of experimental procedures.

3.1.2 Simulation parameters

In order to better understand the governing physics of an ionization wave driven by a relativistic electron current in an insulating target, a simulation using the Cartesian particle-in-cell code PICLS featuring binary collision and dynamic ionization was performed. Due to the nature of the problem, a 2D simulation is needed to gather required information since not only 1D information such ionization speed is needed, but also the geometry of the wave and spatial charge densities which are inherently of higher dimension. For this simulation, both field ionization and the Thomas-Fermi (TF) ionization model for collisionally heated plasmas to calculate ionization levels were included in the calculation.

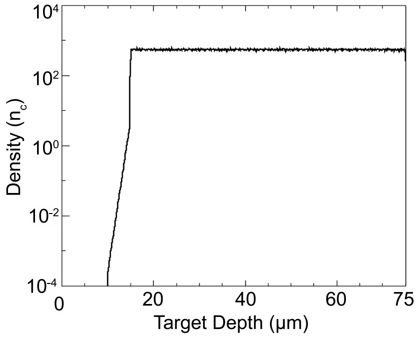

Figure 3.2: Simulation target transversal ion density profile in units of the critical density n_c. The target is designed as a solid slab with exponential pre-plasma profile.

The target consists of solid silicate glass (SiO_2, 2.6 g/cm^3) arranged in slab geometry. In order to facilitate laser absorption, a 5 μm length of low-density gas is placed in front of the target which simulates the effect of pre-ionization by the laser pre-pulse. The target is composed of oxygen (Z=8) and silicon (Z=14) in a ratio of 2:1 with a corresponding electron density $n_O = 404 n_c$ and $n_{Si} = 246 n_c$, respectively, where $n_c = 10^{21}$ cm^{-3} is the electron critical density for 1 μm laser light. This brings the total solid density of the target to about $650 n_c$ for the solid part when the target is fully ionized. The composition of the pre-plasma is the same as the slab but is of a different density. As seen in Fig. 3.2, the pre-plasma has an exponentially increasing profile from $10^{-4} n_c$ to $\sim 4 n_c$. The simulation includes 66 macro-particles per cell, that is 2 silicon, 4 oxygen and 60 electrons to balance the ions charge. The grid size is set to $\lambda/40$ or 0.025 μm/grid. The total size of the simulation box is $75 \times 100\mu$m for a total of 3000×4000 cells. A total of 100 processors and 2 weeks of computation time were required to perform this simulation.

3.1.3 Insulator ionization physics

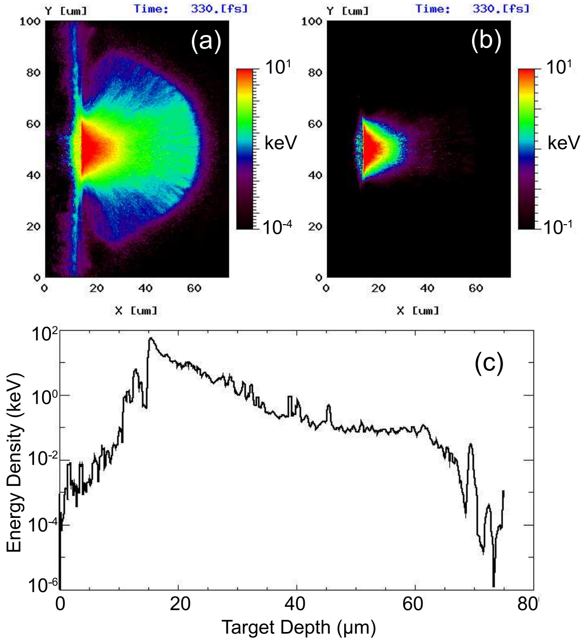

Figure 3.3: (a) Electron energy density in units of keV showing hemispherical expansion of the energy transport. (b) A change in contour levels shows the bulk of the energy is within a narrow region near the center of the target. (c) Transversal plot of the energy density showing a sharp drop at $x > 60$ μm.

A snapshot of the 2D simulation at 330 fs is shown in Fig. 3.3(a) which shows the electron energy density. This quantity is an indication of the global spatial energy distribution inside the target at the specified time. Since at this early time the electrons are not yet in thermal equilibrium with the ions, they carry the bulk of the absorbed energy. We notice the energetic electrons appear to expand in a hemispherical pattern just as in the experiment. Fig. 3.3(b) shows the same data plotted for a different range. This time only the areas where the energy density is above 100 eV are shown. We see that the energy expansion is isotropic and there is a bias with the bulk of the energy residing within a 20 μm region near the axis of the laser. Calculation show that within the first 5 microns from the target surface, 92% of the energy is contained within the central region leaving only 8% expanding laterally. Another singular feature is the sudden sharp decline in energy density near the outer shell of the expanded hemisphere. The energy density drops smoothly radially until $x \sim 55\ \mu$m where a sharp drop is seen in Fig. 3.3(c).

The ionization profile at the same point in the simulation reveals a different picture. Despite the energy density having an asymmetric radial profile, the ionization as seen in Fig. 3.4 is significantly more anisotropic. We can also notice the ionization displays very small scaled filaments indicating that the ionization wave does not ionize in radially uniform way. The ionization wave also has a clearly defined front at $x = 60\mu$m beyond which ionization levels drops to zero. This appears to be significant since it also coincides with the sudden drop in electron energy density beyond 60 μm. The other conclusion we can draw from this is the fact that ionization is relatively consistent radially despite a sharp drop in energy density beyond the 20 μm wide central region. This indicates that ionization is governed by mechanisms other than collisional ionization since the hot electron density appears to have to impact on the ionization magnitude deep in the target near the ionization front.

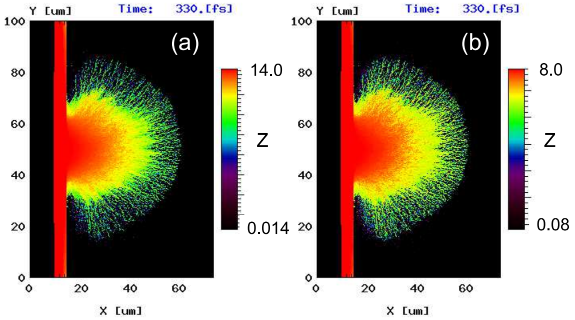

Figure 3.4: (a) Ionization degree of Silicon at 330fs. (b) Ionization degree of oxygen at 330fs.

3.1.4 Electric sheath field generation

Since there does not appear to be a strong correlation between local electron energy density and local ionization degree at the ionization front, collisional ionization cannot explain the ionization physics seen in Figs. 3.3 and 3.4. The electric field's structure, shown in Fig. 3.5, may help explain the unique behavior of insulator ionization dynamics. We first notice from Fig. 3.5(a) an electric sheath field, which is characterized by a ring structure overlapping the ionization front at $x = 60\ \mu$m. As seen from Fig. 3.5(b), which corresponds to the longitudinal profile of the sheath field at the center of the target, the peak of this field is shown to be 1.6×10^{11} V/m which exceeds the threshold for the field ionization of silica (10^{10} V/m [55]) by a factor of 16. At $x > 60\ \mu$m, the target is not ionized and the fast electrons injected from the laser interaction regions are slowed down as they pass through the self-consistent potential generated by the sheath field. As the sheath field travels through the material, it excites and frees bound electrons by the process of field ionization. These newly freed electrons suppress the large electric field and allow the fast electrons to propagate through. Most of the hot electrons are stopped and reflected back in this electrostatic potential $\Phi_s = eE\lambda_{Dh}$. Note the small scale threads of the ionization path as seen in Fig. 3.4 behind the ionization front. They result from the electrical breakdown of the material as the sheath field plows through the target. Their filamentated structure is reminiscent of another natural breakdown phenomenon, electrical breakdown of air during a storm which produces lightning bolts.

The absence of free electrons in insulators precludes the possibility of a neutralizing return current before the initial ionization occurs. As a consequence, the fast electrons carry a net charge and current deep into the target and the lack of balancing return current creates a local charge separation. At the location of the fast electrons, the target is not yet ionized and as such, the electrons perceive the medium they are located in as similar to a vacuum given their small cross-section of interaction with cold bulk atoms. As the charge separation proceeds, the build up of electrons at the front excites the strong sheath field which can reach magnitudes greater than the breakdown voltage of most insulators. As the sheath field is the first source of new electrons resulting from the transport of the fast electrons, the initial ionization inside insulators is therefore initially dominated by field ionization.

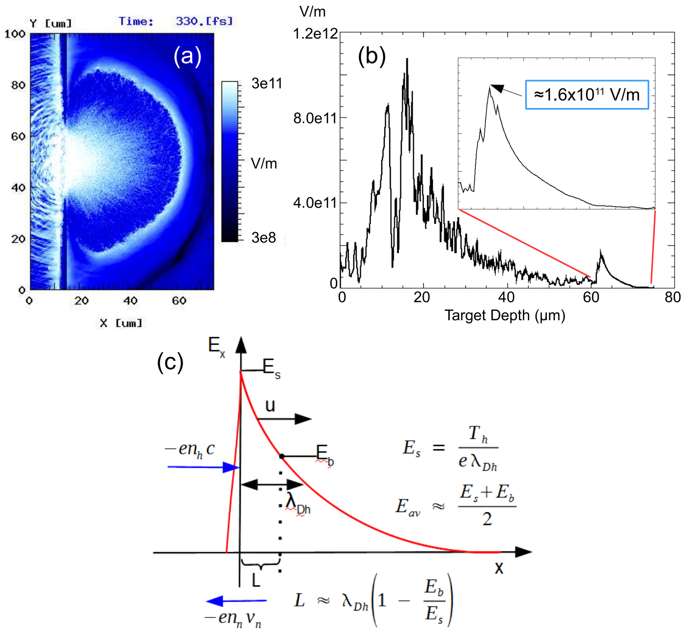

Figure 3.5: (a) Contour of the electric sheath field $E_{sheath} = \sqrt{{E_x}^2 + {E_y}^2}$ in Volts/meter. (b) A transversal profile of the sheath field with a magnified view of the sheath field peak at the ionization front. (c) A diagram of the sheath field describing annotated with geomtrical elements for the derivation of the ionization speed.

3.1.5 Ionization velocity scaling

Here we estimate the propagation speed of breakdown ionization using a simple model of current neutralization for relativistic laser intensities. At the ionization front, the local breakdown produces new electrons which are accelerated backward by the sheath field to rapidly supply a return current. The acceleration time scale is about $\tau \approx L/u$ where u is the ionization wave speed and the breakdown region length is $L \approx \lambda_{Dh}(1 - E_b/E_s)$. Here, E_s corresponds to the peak of the electric sheath field. The conditions are assumed that E_s exceed the breakdown electric field E_b ($E_s \gg E_b$). Following Fig. 3.5(c), L corresponds to the distance between the point at which the sheath field equals the breakdown threshold E_b, and the location at which the sheath field reaches its peak. Since the sheath field decays very rapidly behind the ionization front, the fast electron current behind the front is quasi neutralized by the return current of new born electrons, we thus employ a simple current conservation condition $en_h c \cong en_n v_n$ with e the electron charge, n_h (n_n) the hot electron (new born electron) density, v_n the speed of return current, respectively. Here it is assumed that the fast electron at velocity c the speed of light as an appropriate approximation since MeV electrons do travel at a significant fraction of the the speed of light. Here we neglect the ionization energy since it is much smaller than the hot electron energy flowing into the sheath region. Then the speed of the return current is estimated to be $v_n \approx (eE_{av}/m_e)\tau$. Since the electrons will be subjected to a varying electric field as the sheath field is traveling over their location, we make the approximation that E_{av} is the average electric field the electron would perceive where $E_{av} \approx (E_s/2)(1+E_b/E_s)$. By solving the current conservation equation for u, we get

$$\frac{u}{c} \approx \frac{1}{2}\frac{n_n}{n_h}\frac{T_h}{m_e c^2}\left(1 - \frac{{E_b}^2}{{E_s}^2}\right) \sim \frac{1}{2}\frac{n_n}{n_h}\frac{T_h}{m_e c^2} \tag{3.1}$$

This equation implies the ionization wave can only proceed (that is $u > 0$) when $E_s > E_b$ which indicates breakdown ionization is possible. For relativistic laser plasma interactions, the hot electron temperature T_h follows the ponderomotive scaling described in [56]. This means that T_h is proportional to the square root of the laser intensity, $\sim ((I{\lambda_0}^2)/(1.83 \times 10^{18}))^{1/2}$, such that the ionization wave speed is proportional to $I^{1/2}$. We performed 1D simulations to check this scaling and produced a plot containing previous as well as current experimental observations in Fig. 3.6. We see a clear transition in the ionization speed at around 10^{18} W/cm^2, and the experimental data is also consistent with the $I^{1/2}$ scaling.

3.1.6 Electron energy spectrum and filaments evolution

Taking the electron energy spectrum, it is possible to extrapolate an electron temperature from the slope of the spectrum. Our calculations show the temperature to be 200 keV with electron energies up to 5 MeV in the potential gap and beyond. The green plot in Fig. 3.7(b) shows the spectrum of electron energy for 60 μm $< x <$ 75 μm from which the temperature was evaluated. Notice a sharp dip in electron population for $E <$ 200 keV which indicates that the sheath field acts as barrier for electrons below that energy effectively blocking their forward flux. The ratio of the two spectrums, plotted in Fig. 3.7(c) shows a relatively flat behavior for more energetic particles, but a sharp peak appears for lower energy electrons

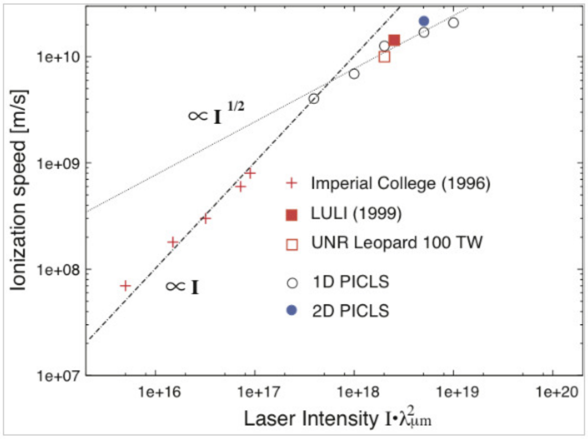

Figure 3.6: Scaling of the ionization speed with $I{\lambda_0}^2$. A transition occurs between the sub-relativistic and relativistic regime at $I{\lambda_0}^2 = 10^{18}$ W/cm^2. The simulation derived results are measured by tracking the ionization front over time and estimating an average velocity from its displacement.

which indicates there are many more electrons of that energy range behind the ionization front than ahead.

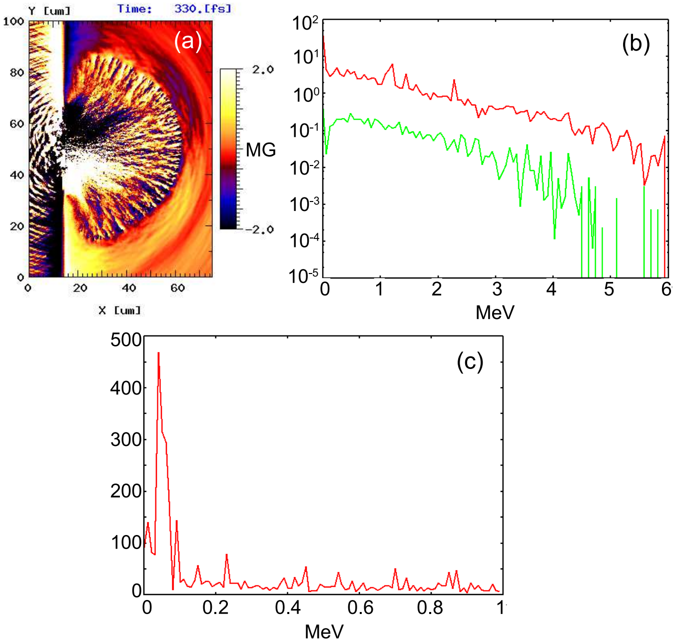

Figure 3.7: (a) A contour plot of the magnetic field showing the small scale filamentation indicative of fragmented current streams. (b) Electron energy spectrum behind the ionization front (red) and ahead of the front (green). (c) Ratio of the spectrum behind the ionization over the spectrum ahead of the front plotted for the range of 0 to 1 MeV.

The final topic for this section concerns the ionization filaments themselves. The structure of the electric sheath field having been described above, it is now time to study the structure of the plasma left behind the ionization front. By looking at Fig. 3.8(a) which shows the sheath field in greater detail, we notice inhomogeneities along the its surface. Small fluctuations in the fast electron flow cause the electric sheath field in certain areas to be stronger. This can manifest itself as local peaks in the field which promotes the process of field ionization. As seen in Fig. 3.8(a) and (b), the local peak in the field has caused an isolated cold cell to increase its ionization level. As the sheath field moves over the course of a few femtosecond, the newly born electrons feel a backward pushing force as seen in Fig. 3.8(c) and (d). As they are pulled backwards through neighboring cells, these electrons which may have gained a few hundred keV from the potential gap, will collisionally ionize other cold atoms. In the path where this process is taking place, the resistivity will begin to drop as new bound electrons are freed due to these mobile charge carrying particles' ease of transmitting current. Meanwhile, the portion of the forward going electrons with lower energy will encounter the counter propagating electrons and form a small filaments similar to a Weibel structured instability. The filamentary structure seen in Fig. 3.7(a) behind the ionization is indicative of unstable counter-propagating currents. In essence, the formation of the ionization filaments is the result of a type of resistive feedback instability.

3.1.7 Summary

In summary of the previous findings, laser-excited ionization in insulator materials display unique features not seen in conducting targets. The simulations presented are in good agreement with experimental observations. We were able to show the hemispherical isotropic expansion of the ionization front despite the highly anisotropic electron beam propagation. In the process, it was uncovered that charge separation from the ultra-relativistic fast electrons was responsible for the existence of an electric field strong enough to initiate ionization. We therefore learned that ionization was initially dominated by electrical breakdown known caused by tunneling ionization. A scaling was then derived to predict the ionization wave velocity and established that $v_f \propto I$ in the sub-relativistic regime, and $v_f \propto \sqrt{I}$ in according

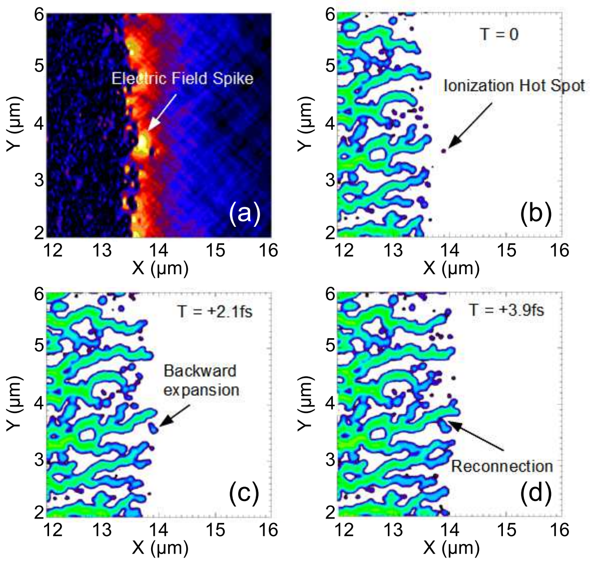

Figure 3.8: (a) A closeup view of the electric field at the ionization front. We notice a local peak due to inhomogeneities in the electron flux. (b), (c) and (d) show the ionization degree evolution over a few femtosecond showing the reconnection of isolated electrons with developing current paths.

to the ponderomotive scaling at intensities beyond the relativistic threshold.

The properties of the plasma behind the ionization field were studied to explain the filamentary structure. We noticed inhomogeneities in the electric field which generated electrons which subsequently began to counter propagate in the medium by the application of a backward pushing force from the electric sheath field. At the locations where ionization occurs and electrons are generation, the transition from solid to plasma leads to a drop in resistivity of several orders of magnitude. The pockets where the resistivity is significantly lower will then invite additional electrons to travel through these locations since they become preferential paths of least resistance. The greater flux of electrons will initiate further ionization due to an increase in collision events. Again, the collisional ionization will further lower resistivity inviting more electrons in the process. This leads a feedback response between the localized reduction in resistivity and increase in collisional ionization. This filaments become unstable and will rapidly grow while energy deposition is still occurring which is likely to be responsible for the lightning structure seen in the ionization patterns and filamentation of the magnetic field. This resistive instability will dominate the electron flux dynamics until the temperature increases sufficiently for the plasma to become collisionless. The scale width of the current filaments is less than 5 μm (see Fig. 3.7(a)) which is smaller than the resolution of the diagnostics used for the experiment. As such, the current filaments which form due to the resistive instability have not been directly measured in silicate glass and direct comparison cannot therefore be made with simulation results at this present time.

3.2 Non-equilibrium ionization modeling

3.2.1 Electron two-temperature energy distribution

The Thomas-Fermi model of the atom has been the standard model used in kinetic modeling of plasmas. However, its premise relies on its treatment of the electrons where it is assumed they form a quasi-classical ideal gas in a self-consistent Coulomb potential [57]. The model is constructed from equations of state which rely on uniform pressures and temperatures to calculate the ionization degree. That is, the volume afforded to each atom must be small compared the spatial gradients in density and temperature. This implies that a plasma that has fulfilled these spatial conditions will also be changing slowly in time compared to the ion collision frequency timescale. This means for the model to accurately reflect the conditions of the plasma, the plasma should be in local thermal equilibrium with the electron gas following Maxwell-Boltzmann statistics. Figure 3.9 shows a typical distribution profile for a laser produced plasma. We immediately notice two regions are present in this plot. The region in red represents the hot relativistic electrons most of which are produced from direct laser interactions. The region in blue corresponds to the cooler thermal electrons of the bulk plasma which have gained their energy through collisional processes by the hot electrons. These two groups are distinguished by different slopes in Fig. 3.9. The steeper slope is indicative of a lower temperature group of electrons while the shallow slope represents the hot electrons. The presence of two slops along with an abrupt transition between the two leads to what is known as a “two temperature” electron population. The abruptness of the transition indicates that the groups do little interacting with one another to transfer energy and momentum.

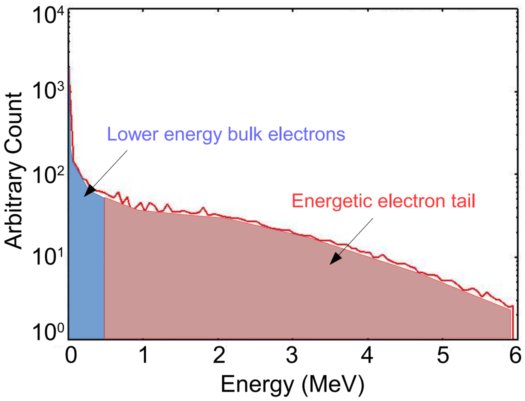

Figure 3.9: Electron energy distribution of a typical laser produced plasma showcasing two distinct electron populations with different temperatures coexisting

This presents a problem for the Thomas-Fermi model which assumes a smooth velocity distribution of electrons represented by a single global temperature. Plasmas produced from high intensity lasers showcase instead two distinct electron populations with very different temperatures, but who also coexist in the same volume with little cross-interaction. Fundamentally, collisional ionization is governed by particle-particle interactions and the associated collisional cross-sections of these interactions for all types of plasmas. However, a new model is needed to better predict collisional ionization for non-equilibrium plasmas. Our particle-in-cell code PICLS was therefore extended to include a new model based on impact ionization cross-sections the details of which were presented in Chapter 2.

Before the comparison between the two models is presented, a few considerations about their implementation and execution in the code must be reiterated. As described in Sections 2.2.2 and 2.2.3, the implementation of these models is only partial. The Thomas-Fermi model accounts for the balance between collisional ionization and three-body recombination, however the recombination is not performed in the event that the plasma cools and the ionization levels is predicted to drop. On the other hand, when impact ionization is used, the process of recombination is completely neglected. Following is a study of the comparison between equilibrium and non-equilibrium ionization modeling in the context of relativistic laser-plasma interactions. These results are presented under the assumption that recombination can be neglected for short timescales when a plasma is under the influence of intense laser irradiation. At this present time, and due to numerical difficulties in implementing recombination in the context of kinetic modeling, the validity of this assumption has not been tested and its effect on plasma dynamics remains unknown.

3.2.2 Simulation parameters

In order to study the differences in ionization dynamics between two models, two simulations were conducted. Both simulations are initialized with identical parameters with the sole exception of the collisional ionization model used. In both cases, a 1 μm laser is used producing an intensity of 5×10^{18} W/cm^2 in a focal spot size of 10 μm over a pulse length of 500 fs. The target material is a solid density 75 μm thick silicon dioxide slab with a 20 μm exponential profiled pre-plasma placed in front to simulate the surface ablation resulting from laser pre-pulse ionization. The total number of grids used were 4000 by 4000 with 66 particles per cell (2 Silicon, 4 Oxygen, 60 electrons). If fully ionized, this amounts to over 1 billion particles. One simulation used Thomas-Fermi to calculate ionization while the other used impact ionization. Both simulations also include field ionization which insulator ionization physics has shown to be important to accurately model the ionization wave. These simulations were performed using 100 processors with a completion time of approximately two weeks.

3.2.3 Ionization comparison

Using this new model reveals new physical effects for multi-species laser-plasma interactions. Figures 3.10(a) and (b) show the average ionization degree per cell for silicon and oxygen respectively. These snapshots were taken at 350fs while the laser is still interacting with the target to show the difference in the evolution of the ionization between the two models while the plasma is still in a transient state. As seen from the plots, the TF model tends to over estimate the ionization degree in the lower density pre-plasma region ($x < 25$ μm). It predicts this region will reach full ionization very quickly in contrast to impact ionization showing maximum ionization around the central hotspot only. Inside the target, the situation is reversed with impact ionization showing higher levels of ionization in the hot spot near the surface. Due to glass being an insulator material, the initial wave of ionization inside the target is dominated by field ionization caused by localized sheath fields driven by fast electrons around the ionization front. With both simulations using field ionization, the ionization front's position shown in silicon's contour plot from Fig. 3.10(a) is at $x \sim 85-90$ μm for both models. However, oxygen's outer electrons are more tightly bound than that of silicon and are thus less susceptible to the initial wave of ionization. It is dominated instead by the second wave of ionization driven by the diffusive collisional ionization process which is governed by either models for these simulations. This explains why oxygen (Fig. 3.10(b) shows a significant difference of about 20 μm in the ionization penetration depth when changing the collisional ionization model. The TF model predicts a faster expansion of the secondary ionization wave which leaves the surface region cooler and less ionized while predicting that hot electrons will dump their energy deeper in the target. Impact ionization shows that a greater number of electrons will collisionally ionize the region near the surface leading to a slower diffusive expansion wave and full ionization at the laser hot spot.

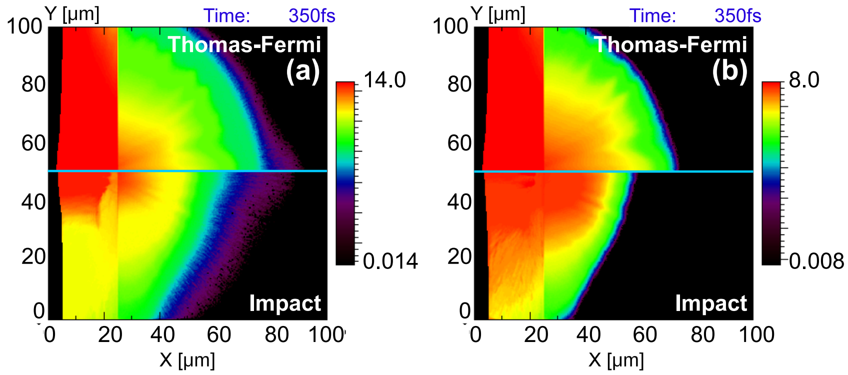

Figure 3.10: (a) Silicon ionization degree (b) Oxygen ionization degree

A cross-section of the target ionization degree at 350 fs is shown in Fig. 3.11. Here the different species' ionization profile are compared to each other in the context of the same model. It is clearly seen that Thomas-Fermi over estimates the ionization of Silicon with the impact model showing it reaching Z=12 instead of the fully ionized Z=14. In addition, the effect of using the ionization cross-section to calculate the ionization probability is emphasized by the greater separation of the ionization front for each species. For impact ionization, the oxygen front is lagging by 30 μm in comparison to 17 μm in the TF simulation. The ionization of silicon shows a sharp step-like decrease in ionization at 50 μm which is not present when using the equilibrium model. This can be attributed to electrons forming two temperature populations as evidenced by a discontinuity in the spectrum data from the simulation. The majority of electrons are heated collisionally to warm temperatures (up to about 500 keV) while a fraction get very high energies via direct interaction with the laser. With the Thomas-Fermi model neglecting the hot electron tail in the ionization calculation, this results in an emphasis on warm electron collisional ionization which leads to smoother ionization profile. The step in ionization shown by the other model is indicative of contributions by two distinct ionization populations. Warm electrons will tend to penetrate less in to the target while the hot electron tail will travel further and have lower probability of ionizing the surrounding media as shown by the sharp decrease in Z beyond 50 μm in Fig. 3.11(b).

3.2.4 Electron kinetics and resistive field generation

Now that the direct effects of using either models on the ionization have been shown, we turn to other simulation metrics to see what additional changes can occur due to using non-equilibrium ionization modeling. The electron energy density shows a similar trend with the TF model underestimating the contribution of the fast electrons to collisional ionization. As explained above, a boundary is set at '10keV' to exclude super hot electrons from directly contributing to the bulk temperature. The bulk temperature is raised by the transfer of energy through collisions between the hot and cold electrons. With the weak coupling between these two groups of electrons being inefficient, this results in a greater proportion of the hot energetic electrons traveling uninhibited deeper in the target. When using impact ionization, hot electrons have an additional channel available to increase ionization in electron-ion collisional ionization. Fig. 3.12(a) shows that impact ionization predicts a greater loss of energy by hot electrons through the mechanism of collisional ionization which results in a slower hot electron population. The spectrum ploted in fig. 3.12(b) shows

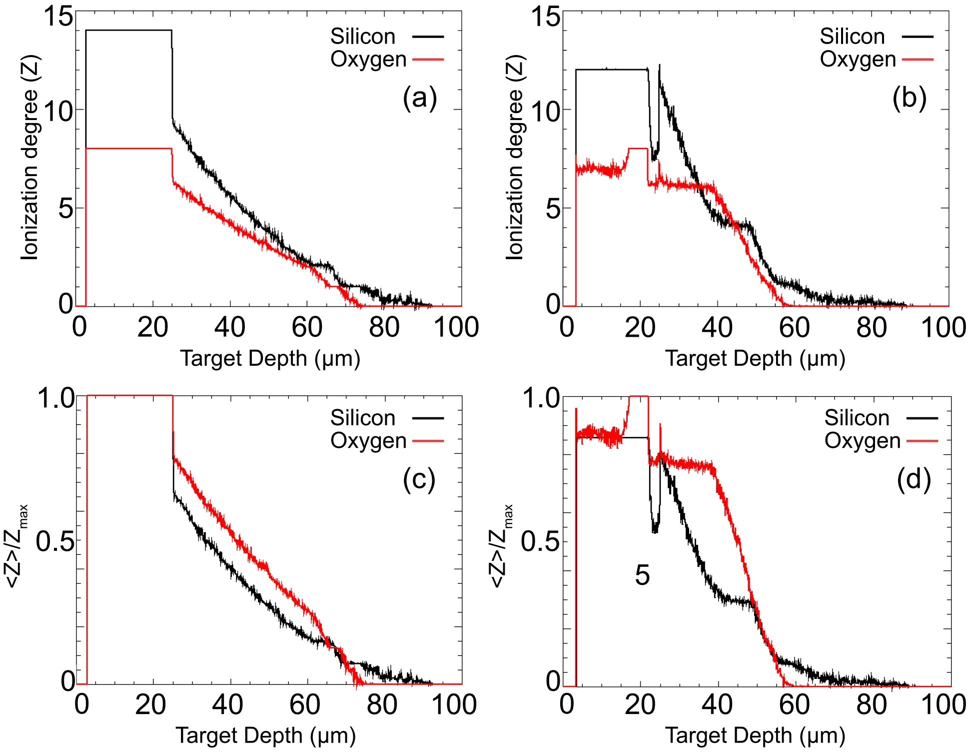

Figure 3.11: (a) Central longitudinal slice of the ionization degree with the Thomas-Fermi model showing showing a smoother ionization profile inside target. Ionization front separation between species is $\sim$ 17 μm. (b) The same plot but this time with Impact ionization model. The species separation is accentuated to $\sim$ 30 μm. (c) Normalized average ionization degree $\langle Z\rangle/Z_{max}$ for Thomas-Fermi. (d) Normalized average ionization degree for impact ionization.

a significant reduction in hot electron population when using impact ionization. Although not the dominant mechanism to increase ionization, impact ionization does show that hot electrons do play an important role in collisional ionization as shown through their loss of energy in comparison to the TF model.

The azimuthal field (Fig. 3.13(a)) clearly demarcates between two regions in the solid density target. Section 3.1 showed how the ionization front for insulators is defined by a strong electric sheath field inside the target. Behind the ionization front ($\approx$ 85-90 μm) is a weakly ionized region with a low density electron background which our simulations have shown to be $\sim$100 eV. In this region, the temperature and density are low which leads to a higher resistivity. Resistivity is a component of $\partial\vec{B}/\partial t$ since there is connection between the time derivative of the magnetic field and the electric field given by $\partial\vec{B}/\partial t = -\vec{\nabla}\times\vec{E}$,

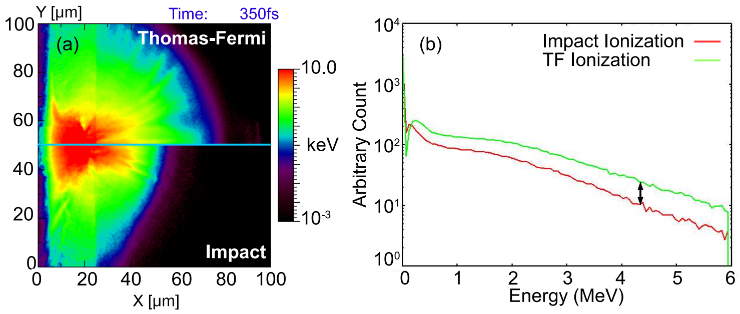

Figure 3.12: (a) Electron energy density contour plot showing the differences in each model. (b) Electron energy distribution throughout the target. Impact ionization shows significant depletion in hot electron population and increased cool collisional electrons.

Faraday's induction equation, where $\vec{E} = \eta\vec{J}$ and by the fact that . However, the magnetic field requires some time to grow which leads to a weak magnetic field in this region at this time in the plasma evolution. The second region (x <65μm for TF and $x < 55$ μm for impact) reveals the boundaries of the diffusive ionization wave. As the name entails, this secondary ionization wave is dominated by collisional ionization. It is characterized by much higher average ionization and is progressing at a much slower diffusive speed. While both models reveal strong modulations in the electron flux, the magnetic field is stronger in the case for Thomas-Fermi which is consistent with higher resistivity. A transversal slice of the azimuthal magnetic field is shown in Fig. 3.13(b) and reveals the field to be 5 to 10 megagauss stronger at its peak. Figures 3.13(c) and (d) show the resistivity to be greater in the diffusion region for Thomas-Fermi. This model depends on bulk heating alone by the fast electron stream and is independent of the hot electron distribution profile. As ionization proceeds, the energy cost from this process is taken from the bulk electrons. Since the bulk electrons are assumed to be in equilibrium, the removal of energy by ionization makes the heating of the bulk plasma slower. As such, the resistivity will tend to be higher than for impact ionization since higher bulk temperatures tend to result in lower resistivity ($\eta \propto 1/T^{2/3}$). On the other hand, impact ionization includes the contribution from the hot electrons population, especially those hot electrons with moderate energy (< 1 MeV) which have a shorter mean free path and are more likely to deposit their energy within a few microns creating a steep gradient in the ionization profile as seen in Fig. 3.11(b).

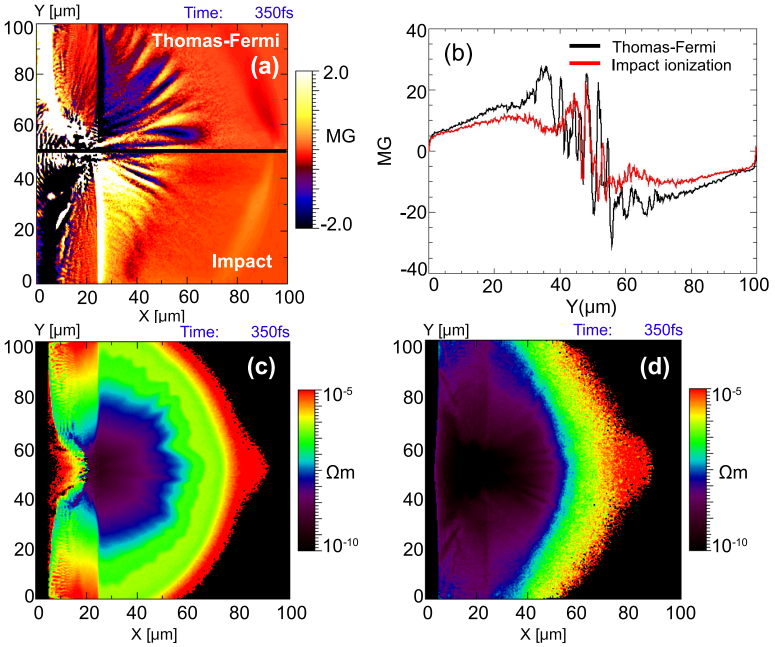

Figure 3.13: (a) Azymuthal magnetic field (B_s) contour plot. (b) Transversal slice of the azymuthal magnetic field profile taken at $x = 30\,\mu$m. (c) Resistivity contour plot for TF ionization model. (d) Resistivity contour plot for impact ionization model.

3.2.5 Summary

We noticed from these results that the choice of the ionization model reaches beyond the accurate prediction of the ionization degree. Due to the differing energy transport mechanisms for each model, the plasma dynamics is affected with the electron energy distribution being rebalanced in favor of cooler electrons. Furthermore, the diffusive ionization speed is also affected due to a change in resistivity in hot highly ionized region. The magnetic field is measurably weaker due to lower fast electron current and lower resistivity in the case of impact ionization. We also notice an increase in the lag of the diffusive ionization wave in the secondary species, that is oxygen when using the new model.

In summary of the ionization models used in PICLS, the Thomas-Fermi model has proven to be reliable in predicting ionization for moderate laser intensities. Below the relativistic threshold ($I < 10^{18}\,\mathrm{W/cm^2}$), the electron population distribution is sufficiently close to a Maxwellian distribution and the density and collision frequency are sufficiently high that an equilibrium ionization model is applicable with good results. With high intensity laser interactions however, it is common to see the generation of a two-temperature electron distribution. For lower laser intensities, the highly energetic tail of the distribution is small and will not affect ionization dynamics appreciably. As the laser energy increases well into the relativistic regime however, the electron population begins to depart further from a Maxwellian temperature distribution for short timescales with the fast electrons beginning to significantly affect ionization physics. The timescales are related to the plasma relaxation time which in turn is given as the inverse of the collision frequency. If the relaxation time is short (high collision frequency), the plasma is considered to be thermalized and the Thomas-Fermi model is then appropriate. For long relaxation times, this is where the application of a non-equilibrium ionization model such as impact ionization becomes important. For example, a solid density aluminum plasma with an electron temperature of a $100\,\mathrm{eV}$ will have a collision frequency of $10^{15} \sim 10^{16}\,\mathrm{Hz}$ which leads to a relaxation time of $0.1 \sim 1\,\mathrm{fs}$ [58]. These temperatures can be achieved using lasers of approximately $10^{18}\,\mathrm{W/cm^2}$. If one is observing plasma dynamics on timescales of 100 fs, the short relaxation times associated with this regime are favorable to use of the Thomas-Fermi model. For higher intensity lasers ($> 10^{19}\,\mathrm{W/cm^2}$), electrons temperatures can easily reach 10 keV leading to collision frequencies of the order of $10^{13}\,\mathrm{Hz}$. For such collision frequencies, relaxation times can stretch to hundreds of femtoseconds. For these regimes, the relaxation times then become comparable or greater than the timescales of electron transport effects. This necessitates the use of a non-equilibrium ionization model. Note here that the TF model is not applicable for lower density plasmas even with non-relativistic laser intensity since the collision frequency will be lower due to the smaller number of particles. The lower density plasma is less collisional leading to an electron distribution which may not thermalize during the interaction time (non-Maxwellian distribution) which will lead to the TF model overestimating the ionization. We have to use the impact model in tenuous plasmas when the density is below $10^21\,\mathrm{cm}^{-3}$. The results have shown that both models begin to differ when the intensity is increased to tenfold of the relativistic threshold. With new lasers with intensities beyond 10^{20} W/cm^2 becoming more common, it has become imperative to move to non-equilibrium ionization modeling as the plasmas generated from such laser systems are increasingly non-maxwellian.

3.3 Electron transport in resistive media

3.3.1 Electron transport experiment

Ultrahigh currents [mega-ampere (MA)] of suprathermal (MeV) electrons that are driven through solids using relativistic laser pulses (with intensity $I > 10^{18}\,\mathrm{W/cm^2}$), lie at the heart of numerous applications such as the generation of ultrashort secondary sources of particle and radiation (ions [59], x-rays [60], positrons [61], or neutrons [62]), fast ignition of inertial confinement targets [63], or laser-driven hadron therapy [64]. The study of electron transport in high energy density (HED) plasmas has been a critical area of focus to develop these applications. A number of experimental studies have been carried out in the past to characterize electron transport in different media such as insulators, metals, and compressed matter [4, 5, 53, 65–68]. To date however, the physics in high energy density plasmas, especially the energy transport in resistive targets, is not fully understood due to the wide range of plasma phenomena ranging from the kinetic regime to the collisional regime including complex atomic processes such as ionization and radiation.

Prior work in the field of the study of electron transport done by Stephens *et al.* [4] on the comparison of transport features between conductors and insulators has yielded interesting results. In order to determine the electron beam divergence inside the target using external detectors, a thin copper layer is embedded at a given distance inside the target. When hot electrons produced by the laser travel through the transport medium and gain their transport feature, they then collisionally interact with the copper layer once they reach it. The product of this interaction are K-α transitions which generate hard x-ray radiation [69]. These hard x-rays have very small cross-sections of interaction and tend to propagate unattenuated through most low Z materials. Therefore, they are the ideal signal marker for electron trajectory measurements. With enough resolution, one can spatially resolve the K-α emissions to determine the shape of the electron transport at a specific depth in the target. Then changing the transport medium allows comparison to be made.

The target configuration used in the experiment is shown in Fig. 3.14.

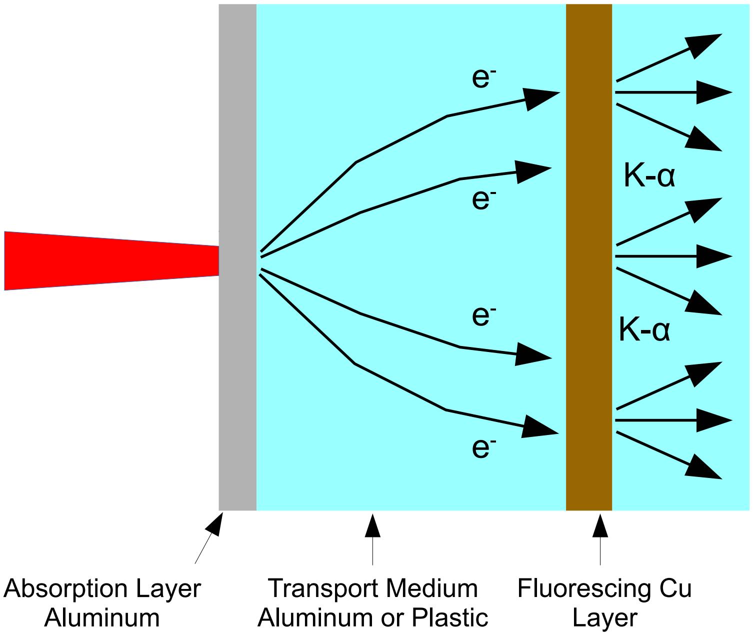

Figure 3.14: The experimental setup used for the experiment. [4]

Results from the experiment showed a tightly collimated electron transport pattern in the aluminum target as is evidenced by narrow peak in the K-α images. On the other hand, plastic's K-α signal was broader with multiple peaks indicating a non-uniform filamentated density in the electron transport current. Shown in Fig. 3.15 are the captured images for both materials. On a different note, transport experiments with higher laser intensities as reported in Ref. [5] have shown a more modulated and spread transport pattern in the Al target, while high Z gold displayed a single tightly confined guiding pattern. At present time, the physics that governs the transport characteristics are not completely understood for various target materials and laser intensities. For example, the critical condition and its physical dependencies for guided (collimated) transport to occur are not known.

3.3.2 Guiding condition derivation

Work by Bell and Kingham [70] involved the derivation of a collimation condition for laser-plasma interactions starting from a characteristic electron energy eT_{fast}. The electrons are assumed to hemispherically expand with radius R_{laser} being the laser spot size. By

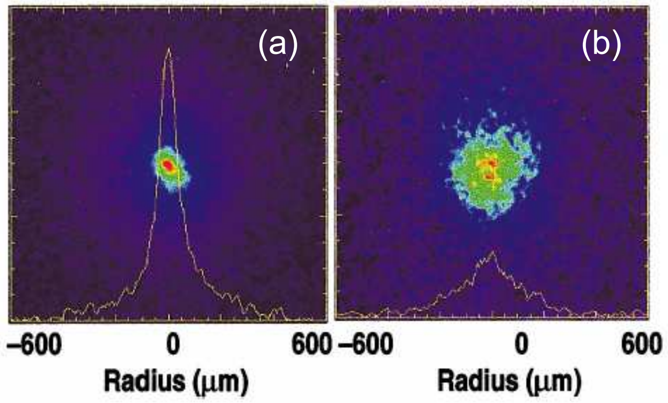

Figure 3.15: K-α images taken at 125μm inside the target for (a) aluminum and (b) plastic from Ref. [4]. Laser beam characteristics: 10 μm focal spot size, 100 Joules, 1 ps, 2×10^{19} W/cm^2.

assuming current neutralization such that $j_{fast} = -j_{cold}$, where $j_{cold} = E/\eta$, a magnetic field is generated according to $\partial B/\partial t = -\nabla \times E = \nabla \times (\eta j_{fast})$. This field is azimuthal surrounding the electron beam and applies a collimating force to the beam. Then by inputing the electron beam parameter, one can derive a guiding condition

$$\Gamma = 0.022 n_{23} {P_{TW}}^{-1} {R_{\mu m}}^2 {T_{511}}^{1/2} \times (2 + T_{511})^{-1/2} (T_{c,keV} - T_{i,keV}) {\upsilon_{rad}}^{-2}. \tag{3.2}$$

Here, n_{23} is the electron density in units of 10^{23} cm^{-3}, P_{TW} is the power of the fast electron beam in units of terawatts, $R_{\mu m}$ is the beam radius in microns, T_{511} is the fast electron units normalized by 511 keV, $T_{c,keV}$ is the temperature of the cold background plasma, $T_{i,keV}$ is the initial temperature of the plasma and υ_{rad} is the half angle of the divergence of the electron beam in radians. In the situation where resistive heating is important ($T_{c,keV} \gg T_{i,keV}$), the above equation changes to

$$\Gamma = 0.13 {n_{23}}^{3/5} Z^{2/5} ln\Lambda^{2/5} {P_{TW}}^{-1/5} {T_{511}}^{3/10} \times (2 + T_{511})^{-1/2} {R_{\mu m}}^{2/5} {t_{psec}}^{2/5} {\upsilon_{rad}}^{-2}. \tag{3.3}$$

Here the additional parameters are Z, the charge state, $ln\Lambda$ the coulomb log and t_{psec} is time in units of picoseconds. Then the guiding conditions states that guiding will occur when $\Gamma > 1$.

In principle, this guiding condition is all that is needed to predict the electron transport's capacity to collimate. However, some of the parameters such as electron beam characteristics and temperatures are unknown *a priori* for standard experimental settings. In this context, we have elected to rederive the scaling using a different approach by connecting the laser parameters to the electron injection profile through the ponderomotive scaling. Ionization gradients are taken into account as a result of heating to obtain an empirical guiding condition which depends on natural input parameters while arriving to a useful scaling equation.

To estimate the resistive magnetic field, we first calculate the bulk temperature evolution under relativistic laser irradiation. In the Vlasov equation modified with Fokker-Plank collisions terms [58], three heating terms exist: resistive heating, drag heating (direct collisions among electrons) and diffusive heating. At solid density, the resistive heating term dominates and the other terms may be neglected. We discard drag and diffusive heating terms and solve the equation with the remaining resistive heating term,

$$\frac{3}{2}\bar{n}_e \frac{\partial \bar{T}_e}{\partial \bar{t}} = \bar{\eta}\bar{j}^2, \tag{3.4}$$

where $\bar{n}_e$ is the electron density normalized by the critical density n_c, and $\bar{T}_e$ is the bulk electron temperature normalized by the electron mass energy $m_e c^2$. $\bar{t}$ is time normalized by the laser oscillation period τ and $\bar{j}$ is the current normalized the electron current $en_c c$ where c is the speed of light. The normalized resistivity $\bar{\eta}$ in the Spitzer regime [71] is written as $\bar{\eta} = \bar{\eta}_0 ZL/\bar{T}_e^{3/2}$ with charge state Z, the Coulomb logarithm L, and a constant $\bar{\eta}_0 = e^2\omega/m_e c^3 \sim 1.6 \times 10^{-8}$.

Assuming a stationary current (constant in time with no longitudinal gradient $\partial/\partial x = 0$) as $\mathbf{j}_h(r) \simeq \alpha e n_h(r) c\mathbf{n}$, here e is the electron charge, $n_h(r)$ the fast electron density, $\mathbf{n}$ is the flow direction, and α is a factor of the fast electron divergence. The electron density is assumed to have the same radial profile as the laser beam. In addition, individual electrons in the current beam are assumed to travel in different directions with an average divergence angle $\langle\theta\rangle$, such that $\alpha = \cos\langle\theta\rangle$. The fast electron density n_h is estimated from conservation of energy flux by assuming that most of the energy is absorbed by the electrons, namely, the absorbed laser energy flux equals the fast electron energy flux

$$\chi I \simeq \epsilon_h n_h c, \tag{3.5}$$

where χ is the absorption coefficient. We then rewrite the absorbed energy flux as

$$\chi I = m_e c^3 n_c(\gamma^2 - 1) \simeq m_e c^3(\gamma - 1) \cdot \gamma n_c, \tag{3.6}$$

here the Lorentz factor is $\gamma \equiv \sqrt{1 + \chi a^2/2}$ with a normalized laser field $a = eE/m_e c\omega$, E the laser electric field, m_e the electron mass, and ω the laser frequency, respectively. The final approximation is to assume $\gamma \gg 1$. Since the fast electron energy distribution follows the ponderomotive potential, $\epsilon_h = m_e c^2(\gamma - 1)$ [56], its density is approximated as $n_h = \gamma n_c$, so that the normalized fast electron current becomes $\bar{j}_h \simeq \gamma$. When a laser pulse has a gaussian spot profile of radius $\bar{r}_0$, normalized by a laser wavelength λ, the fast electron current can have the same profile as the laser, $\bar{\mathbf{j}}_h(\bar{r}) \simeq \gamma \exp(-\bar{r}^2/\bar{r}_0^2)\mathbf{n}\cos\langle\theta\rangle$.

We can integrate Eq. (3.4) with the initial temperature $\bar{T}_{e0}$ on the laser axis as,

$$\bar{T}_e = \left(\bar{T}_{e0}^{5/2} + \frac{5}{3}\frac{\bar{\eta}_0 L\,\gamma^2\,\bar{t}}{\bar{n}_i}\right)^{2/5}. \tag{3.7}$$

Then, the bulk electron temperature increases from $T_{e0} = 0$ with a scaling of $t^{0.4}$ and $\gamma^{0.8}$, while the resistivity decreases with respect to T_e by scaling as $T_e^{-3/2}$.

Using the resistivity, we can calculate the resistive magnetic field $\bar{B}_R$ $(= eB_R/m_e c\omega)$ by integrating Faraday's equation to obtain the azimuthal component B_R driven by $\partial\bar{\eta}\bar{j}_x/\partial\bar{r}$.

$$\frac{\partial\bar{\mathbf{B}}_R}{\partial\bar{t}} = \frac{\partial\bar{\eta}\bar{j}_x}{\partial\bar{r}}. \tag{3.8}$$

We assume the ionization charge state Z has the same Gaussian profile as the fast electron current, $\propto \exp(-\bar{r}^2/\bar{r}_0^2)$ and simplify the problem by eliminating the time dependence of Z by using a constant Z_f. Here Z_f is the full ionization charge state at the center of the beam. We then have an expression for the resistive magnetic field in terms of the electron beam profile which is known from the ponderomotive potential scaling. Then

$$\bar{B}_R(\bar{r},\bar{t}) = 1.84\, t^{2/5} f(\bar{r}) \frac{\bar{n_i}^{3/5}(\bar{\eta}_0\, L)^{2/5}}{\gamma^{1/5}} Z_f \cos\langle\theta\rangle, \tag{3.9}$$

with the radial profile function $f(\bar{r}) = -1.6\,(\bar{r}/\bar{r}_0^2)\exp\left(-\bar{r}^2/\bar{r}_0^2\right)^{4/5}$. The magnetic field has a peak amplitude at a radius of $|\bar{r}| \simeq 0.8\bar{r}_0$. By evaluating Eq. 3.9 at that position, one obtains the peak magnetic field electrons may experience during transport. This result is

$$B_{R\max}(t)[\mathrm{MG}] \simeq 0.11 \frac{\bar{n}_i^{0.6} L^{0.4}}{r_{0[\mu m]}\gamma^{0.2}} \bar{t}^{0.4} Z_f \cos\langle\theta\rangle. \tag{3.10}$$

where $\bar{t}$ is in units of laser period τ.

Now that we have an expression for the confining resistive magnetic field in Eq. 3.10, we can define a guiding condition of the fast electrons under magnetic fields, as in Ref. [70], as a ratio of the Larmor radius r_L and the spot size r_0. If the ratio is less than unity, an electron with a lateral trajectory will stay in the spot region by the mechanism of magnetic rotation. The Larmor radius of a relativistic electron under a megagauss field is $r_L[\mu\mathrm{m}] \sim \gamma 15.9/B_{\mathrm{MG}}$. Since the magnetic field experienced by the electrons will be varying spatially between $\pm 0.8 r_0$ as the particles are rotating, an assumption is made to simplify the guiding expression. We choose to set the magnetic field experienced as the average $B_{R\max}/2$ or half the peak field as the average field in channel. The guiding condition Γ then becomes

$$\Gamma(t) \equiv \frac{r_L}{r_0} \simeq \frac{289\,\gamma^{1.2}}{\bar{t}^{0.4}\bar{n}_i^{0.6}L^{0.4}\, Z_f \cos\langle\theta\rangle} < 1. \tag{3.11}$$

Here we can use the ion density in solid $\bar{n}_i \sim 50$ and the Coulomb logarithm $L \sim 5$, both are good approximations in laser-solid interactions, and we also replace $\bar{t}$ by $\bar{t}_{pulse}/2$ since confinement should occur before the laser pulse halfway mark for the resistive guiding to be considered stable. Finally, the simplified critical parameter Γ_s of the resistive guiding in solid targets is

$$\Gamma_s = \frac{14.6\,\gamma^{1.2}}{(\bar{t}_{pulse}/2)^{0.4}\, Z_f \cos\langle\theta\rangle}. \tag{3.12}$$

The laser parameter dependence is included in γ and $\bar{t}_{pulse}$. We find that conditions with lower intensity, longer pulse duration, higher Z material, and smaller divergence are more conducive to achieving resistive guiding.

3.3.3 Simulation parameters

To benchmark the scaling and study the the transport physics deep inside the target, we use a two-dimensional collisional particle-in-cell code, PICLS [2,3], which features binary collisions among charged particles and dynamic ionization processes in gas and solid density plasmas. Fully self consistent study of transport features in solid materials would require modeling the targets in 3 dimensions. For the size of targets needed for an adequate comparison with experimental data however, the scales of interest require the modeling of a volume of $\approx 1 \times 10^6 \mu\mathrm{m}^3$. To simulate such volumes in 3D using a kinetic approach represent prohibitive costs in computational power well beyond the capability of our available computer infrastructure due to the very large number of particles which need to be included. We must therefore limit our study to 2 dimensional laser-plasma interactions.

The simulation parameters were determined in accordance with experimental conditions of Ref. [4]. Two simulations were prepared with targets made of solid plastic and aluminum to represent insulators and conductors to study the materials specific to the experiment. Since plastic and aluminum have different average atomic numbers Z, solid silicon was chosen as a third material to represent an insulator with similar atomic number Z to aluminum to see the effect of initial insulation on transport physics.

Given the experiments used targets of varying thickness, it was determined that a thickness of 125 μm would offer the best compromise between enhancing transport features and lowering computational cost. For shorter transport distances, the unique features for each material may not fully develop while longer distances will lead to enhanced transport features, but at a much higher simulation cost. The transverse dimension was set to 150 μm to allow sufficient volume for lateral development of transport features. For high intensity lasers, the main laser pulse never hits a sharp target interface due to surface ablation from the laser pre-pulse. To simulate this effect, a 20 μm thick pre-plasma is place in front of the target and is given an exponentially increasing density profile with a short scale length of

$2\,\mu$m and a maximum density of 100 n_c. For all materials (aluminum, plastic and silicon), the pre-plasma is composed of aluminum for the laser absorption to be identical among all simulations.. The $145\,\mu$m deep (including pre-plasma) by $150\,\mu$m wide target is placed in a 200 by $150\,\mu$m simulation box with $5\,\mu$m of vacuum in front and $50\,\mu$m on the backside of the target. An 800 fs laser pulse is injected from the left boundary at an intensity of $10^{19}\,\mathrm{W/cm^2}$ with a wavelength of 1 μm. The beam is focused down to $10\,\mu$m corresponding to the full width at half the maximum intensity and the rise time is 100 fs. Both field ionization and collisional ionization are included along with binary collision among charges in partially ionized plasmas [3]. The plastic and aluminum targets are given an initial charge state of $Z = 0$ and $Z = 3$ in order to distinguish them as insulator and conductor respectively. The electrons initially present for aluminum will serve to simulate the conduction band electrons that freely roam through the metal. Both simulations used a grid size of 8000 by 6000 cells. For the aluminum simulation, 2 ions and 26 electrons were used for a total of 974 million particles while plastic was performed with 3 carbon ions, 3 hydrogen ions and 21 electrons for a total of 730 million particles. These simulations were performed with 200 cpus each and took 1 week to compute 1 ps of data.

3.3.4 Electron transport simulation results

We begin the data analysis with a comparison between the electron energy density plots of either materials. This quantity best shows the trajectory of electrons along with information about the energy distribution inside the material. Figure 3.16 (a-c) and (d-f) show the time evolution of electron energy density in aluminum and plastic targets, respectively. Fast electrons inside aluminum appear to form a narrow jet along the center of the target with the majority of electrons being confined by the strong magnetic field to reside in a narrow ($\approx 50\ \mu$m) wide stream. This geometry is temporally and spatially stable as is evidenced by the jet maintaining collimation over the entire thickness of the target and at later times until the pulse is turned off ($t \sim 1200$ fs). The hottest electrons produced are not guided by the magnetic channel (see Fig. 3.18 (c) for the magnetic field contour) and escape the central jet with a large divergence angle. However, the total energy carried by these electrons is small

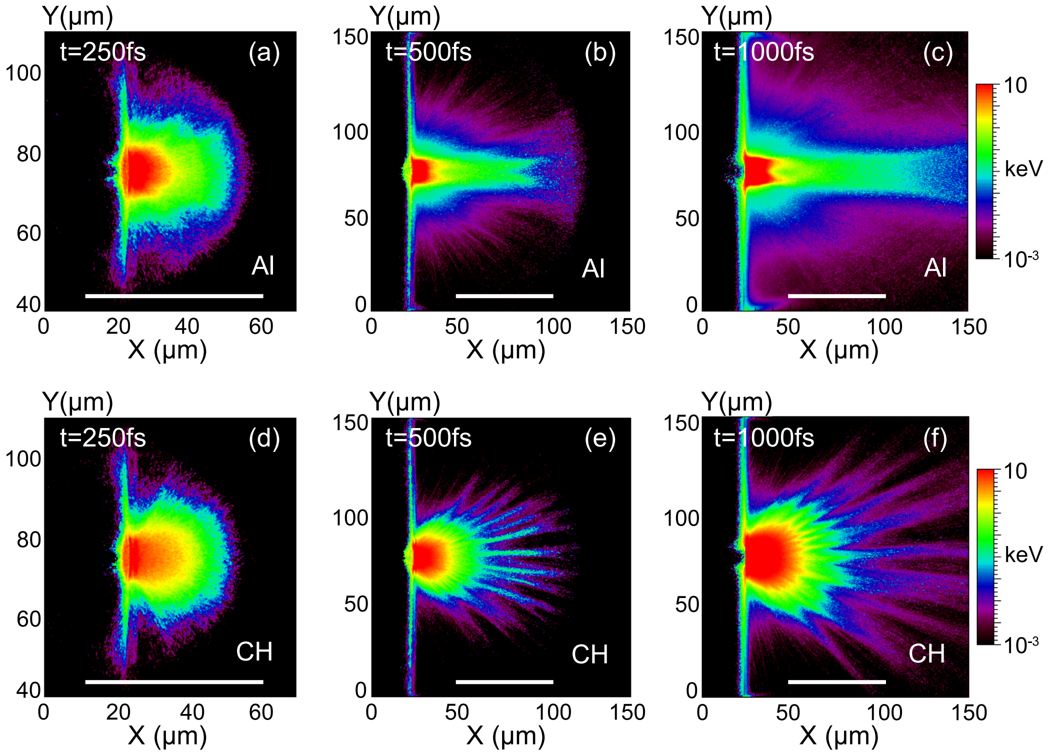

Figure 3.16: 2D contour plots of the normalized electron energy density for (a-c) aluminum, and (d-f) plastic at t = 250, 500, 1000 fs. A white bar in each plot indicates 50 μm scale.

as is evidenced by a drop of approximately two orders of magnitude in energy density from the center to 25 μm of either sides of the electron jet. On the other hand, the plastic target reveals that energetic electrons are broken into multiple channels. The time integrated electron flux of forward moving electrons is obtained at 125μm from the target and shown in fig. 3.17 (a) for Al and (b) for plastic. These figures relate to the K-α images observed at the same location in experiment [4] shown in Fig. 3.15 by the fact that K-α emissions are proportional to the number of hot electrons (above keV) which pass through the copper layer located 125 μm inside the target. In other words, a greater number of electrons passing through the copper layer at a specific point will lead to more K-α transitions which in turn translates to a brighter x-ray signal. We see a similar trend in the K-α images with the simulation results, namely, one single narrow image for Al and widely spread multi-peak image for plastic. We also denote Figs. 3.16 (a) and (d) at t = 250 fs which serve as examples to show the temporal aspect of the magnetic field. Both materials have very similar energy

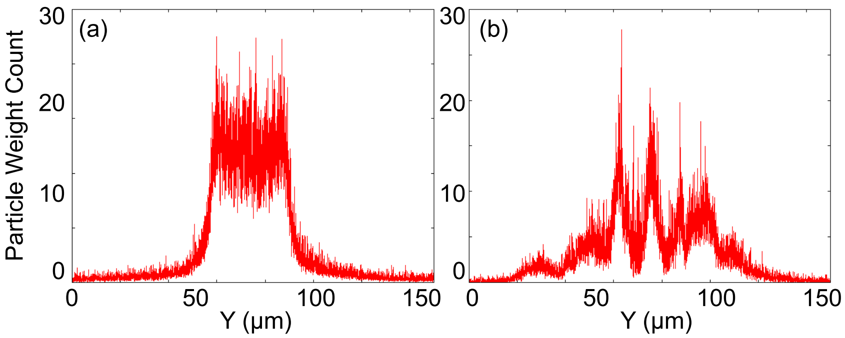

Figure 3.17: The time integrated flux of forward going hot electrons over 2ps at 125μm deep inside the target for (a) aluminum and (b) plastic.

density profiles at during times, and it is only once the magnetic field has had time to grow ($t \geq 500$ fs) that the collimation or filamentation become apparent. The time dependence of the guiding condition is discussed later using Eq. (3.9) in Fig. 3.20.

The propagation of ionization wave was measured and discussed in section 3.1. The speed of the ionization wave is explained by the breakdown process in the formation of sheath fields at the wave front. Absence of background electrons in insulators causes the presence of a peak in the electric field at the ionization front of the order of 5×10^{11} V/m, which slows down fast electrons. Then the ionization wave (breakdown via field ionization) becomes slower than the fast electron speed $\sim c$ as seen in Fig. 3.18 (a) and (b) of the resistivity plot, which is showing heating by $\eta \propto T^{-3/2}$. Comparing the aluminum of Fig. 3.18 (a) where the heating front is at $X \simeq 150\,\mu$m at $t = 500$ fs, the front moves almost with the speed of light while the plastic heating front moves with $\sim 0.8c$ ($X \sim 120\,\mu$m). Inhomogeneities in the sheath field seed sub-micron scale filaments around the ionization front as seen in fig. 3.18 (b) and (d). The magnetic fields induced from these filaments are much weaker than the magnetic field induced from the resistive gradient which determine the global transport pattern. Figure 3.18 shows the mega-gauss magnetic fields pattern is consistent with the resistivity topology, which confirms the strong magnetic fields originate from the resistive gradient. The resistive instability will always creates filaments [67], but if the magnetic field at the edge of the beam is strong enough, these filaments will combine and form a single transport conduit. In higher resistivity materials, the energy of the return current will be dissipated through collisions and the forward going current will be responsible for generating a strong global magnetic field. The growth of the maximum resistive magnetic field in the simulations follows Eq. 3.10.

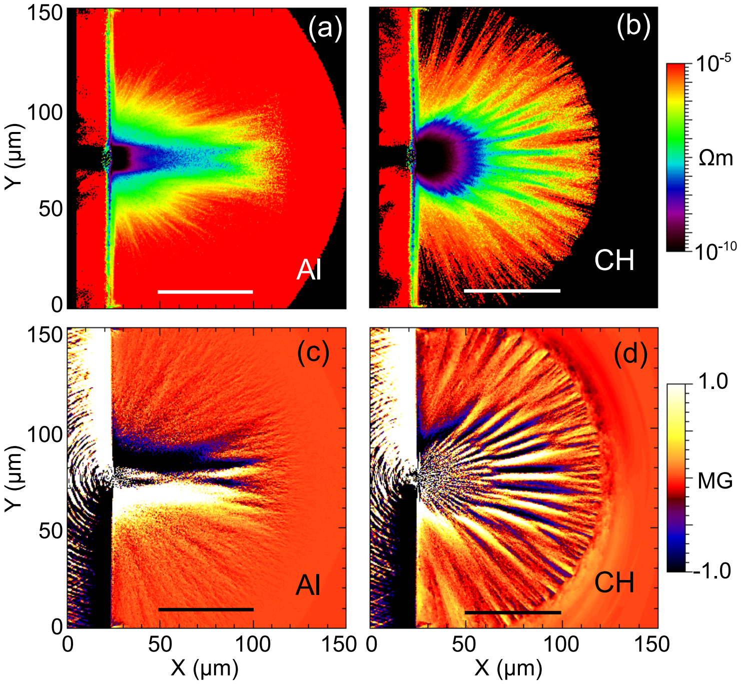

Figure 3.18: The resistivity measured at $t = 500\,\mathrm{fs}$ for Al (a) and plastic (b). The resistive magnetic field observed in Al (c) and plastic (d) at the same time of (a) and (b). A bar in each plot indicates $50\,\mu\mathrm{m}$ scale.

So far, the resistive magnetic field appears to be the dominant factor in controlling how the electron flux is guided. A strong dipolar magnetic field will develop in higher resistivity (more collisional) materials while a weak magnetic field due to lower resistivity will result in the field being unable to collimate the beam in more conductive materials (less collisional). The dipole geometry of the field is largely due to the formation of a single large current carrying electron jet. However, there is an additional effect which was believed to be responsible for the corrugation. Since plastic is an insulator, it is susceptible to electric breakdown and will form small scale ionization filaments which could potentially seed the larger scale corrugation seen above. In order to test this hypothesis, an additional simulation with an insulator with a Z value comparable to aluminum was performed using Silicon. With a Z of 14 compared to 13 for aluminum, resistivity of Silicon should be comparable to aluminum, but retain the insulator characteristics of plastic. Fig. 3.19 (a) to (c) shows the resulting electron energy density inside a silicon target which exhibits the same behavior as aluminum. The resistivity of the material appears to dominates transport while the initial electrical properties of the material do not appear to affect the transport pattern once the energy deposition achieves a steady state. The simulations show that the filamentation caused by the resistive instability at the ionization front is quickly overshadowed by the growing channels from the diffusive collisionally dominated region's growth.

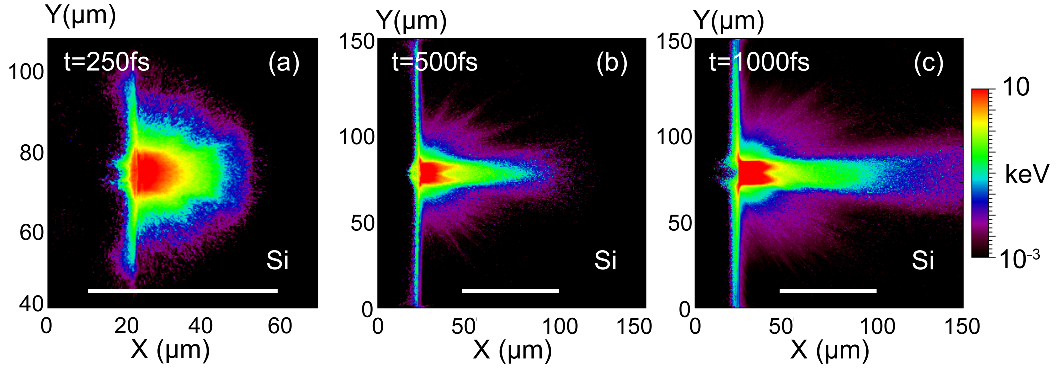

Figure 3.19: Energy density of Silicon at (a) 250 fs, (b), 500 fs and (c) 1000 fs. The bar shows 50 μm scale.

The magnetic field inside the target is not constant over time. The constant influx of energy from the laser while the pulse is still incident on the surface will generate a growing electric field which in turn will stimulate an increasing current. The magnetic field is directly tied to the current and its strength will also have a time dependence. Since the critical condition Γ_s is derived from the magnetic field, it as well will have a time dependence. Figure 3.20 shows the temporal evolution of the critical condition, $\Gamma(t)$, from Eq. (3.11) for the aluminum and plastic simulations. The absorption measured in the simulations is about 30%. Here the timescale is normalized by the laser oscillation period τ and starts when the peak of the laser light hits the target surface. The Γ for both targets is still > 1 at $\bar{t} \simeq 20$, namely, no strong confinement yet occurs, and in fact the electron energy density from the simulations at the corresponding time is Fig. 3.16 (a) and (d) at $t = 250\,\text{fs}$ shows similar patterns in Al and plastic. At later time, aluminum reaches $\Gamma < 1$ and exhibits resistive

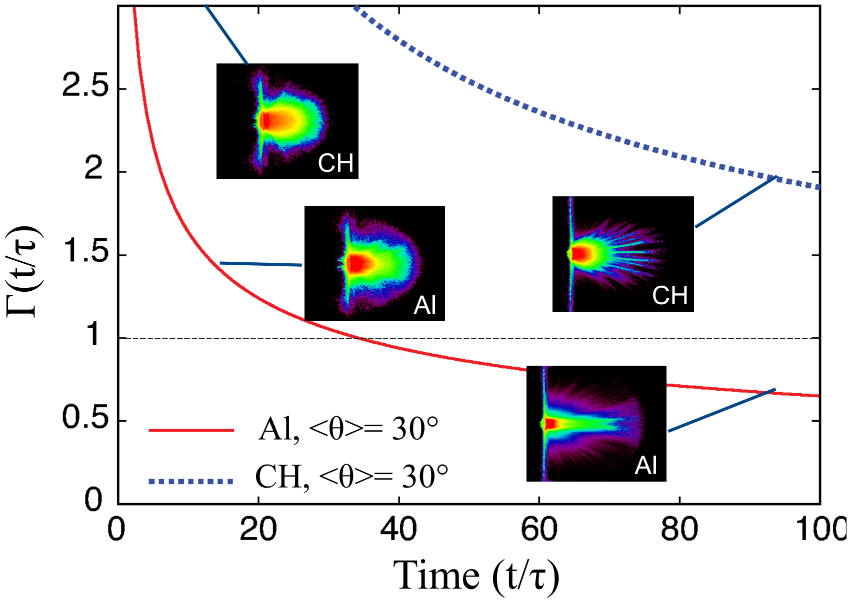

Figure 3.20: The resistive guiding condition $\Gamma(t)$ with snapshots of the electron energy density in simulations. Snapshots shown for 250fs and 500fs from which 185fs must be subtracted to account for laser travel time and peak intensity ramp up. The electron divergence and the absorption coefficient set to $\langle\theta\rangle = 30°$ and $\chi = 0.3$ in this plot, respectively.

guiding.

3.3.5 Guiding condition restrictions

The critical condition Γ_s for resistive guiding in solid targets defined by Eq. (3.12) and is plotted in Fig 3.21 for various laser intensities and materials. It is shown that for an intensity $5 \cdot 10^{19}$ W/cm^2, even aluminum exhibits filamented divergence with $\Gamma_s > 1$ while CH starts to show guided pattern at 10^{18} W/cm^2 with $\Gamma_s < 1$ which are also consistent with what is seen in the simulations. A gold target has $\Gamma_s < 1$ and a confined transport pattern even at $6 \cdot 10^{19}$ W/cm^2, which was confirmed in the experiment [5]. To quantitatively judge whether transport is guided or not, the transverse energy density profile was analyzed. We define ξ as the percentage of energy that remains within the laser beam spot $2r_0$ (10 μm) measured inside the target at a position r_0. We noticed that when guiding occurred, ξ stays greater than 80%. This threshold comes from the fact that for a natural Gaussian function, ≈80% of the integrated area under the curve lies between the half-width half-max points. So given an Gaussian injection profile of energy from the laser, if >80% of the energy remains within the width of the laser beam a few microns deep in the target, it indicates the Gaussian profile is well maintained and the magnetic field is collimating the electron beam. When divergence was observed, ξ quickly dropped to 60% or less. The ξ measured in each simulation is shown in Fig. 3.21.

Note here that our guiding condition assumes no longitudinal current gradient. The guided transport proceeds with the magnetic field extension which is why the target thickness L_t is another important parameter to consider when performing a transport study. The resistive magnetic channels must be allowed enough space to grow longitudinally through the target. If a target is too thin, the magnetic field may not reach the predicted values by the scaling and divergence may be observed when collimation was expected. The same can be said of the laser pulse duration which must be maintained long enough for the magnetic field to reach the backside of the target. If the laser duration is not long enough, even if $\Gamma_s < 1$ is satisfied, the fast electrons can splay out from the magnetic channels in the middle of the target and widely spread patterns will appear at the backside of the target [5]. As a simple stipulation to insure the magnetic channels reach the back of the target is to set a condition on the pulse duration such that $\tau_{pulse} > 2L_t/c$ empirically.

3.3.6 Summary

Electron transport in resistive media is a subject of critical importance for many physical applications that depend on the characterization of laser-produced electron beam. The physics involved in understanding the transport patterns are complex due to the numerous interactions and processes which occur. Many variables must be accounted for and the nonlinear relations between them can make deriving analytical models virtually impossible. However, empirical models can be derived as seen from the works of Bell and Kingham which can be effective in providing insight to design new experiments relying on transport phenomena.

In this section, we have extended the transport concepts introduced by Bell [70] to include the ponderomotive potential scaling for hot electron generation in the relativis-

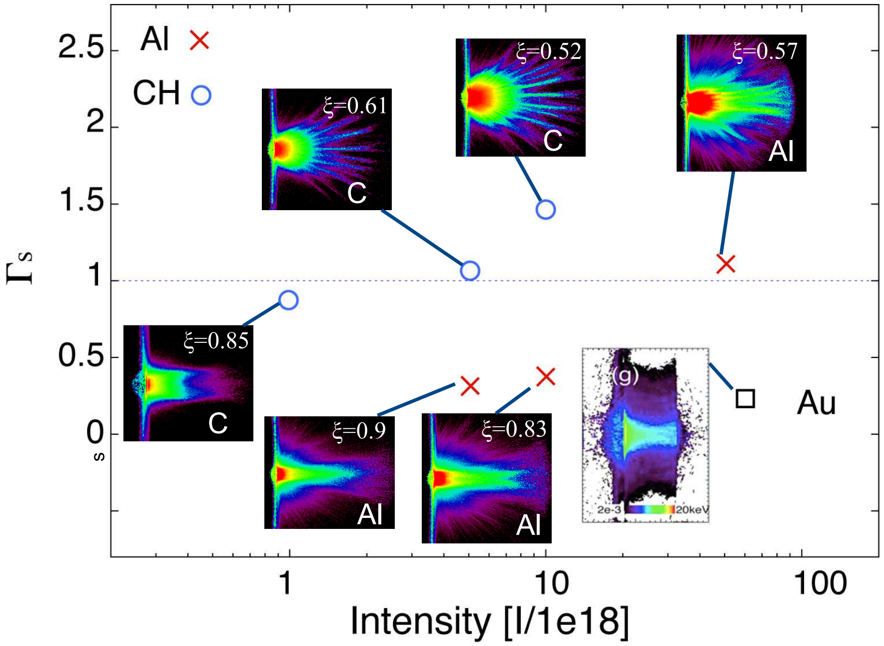

Figure 3.21: The critical parameter Γ_s for various laser intensities and materials. Circles are for CH, and crosses are for Al. The gold simulation result is from Ref. [5]. The values are evaluated with $\langle\theta\rangle = 30^\circ$ and χ in each simulation.

tic regime. A guiding condition was subsequently derived which provides a threshold for predicting whether divergence ($\Gamma > 1$) or collimation ($\Gamma < 1$) will occur. The temporal aspect of the guiding mechanism was discussed and a set of conditions and limitations were described to delimit the parameters for which the scaling is applicable.

Simulation results were also presented to benchmark the scaling for a variety of materials and laser parameters. We showed the transition from collimation to divergence in both aluminum and plastic with laser intensities ranging from 1×10^{18} W/cm^2 to 5×10^{19} W/cm^2. We also conclusively determined that instabilities at the ionization front were not responsible for the current channeling effect in plastic. A silicon simulation was presented which exhibited the typical field ionization driven wave front while still resulting in a guided transport pattern.

Chapter 4

Summary

The subject of electron transport in solid materials is a broad topic which includes many different features and physical effects such laser absorption, plasma wave generation, current and resistive instabilities, collisions, ionization, recombination, and radiation production and transport. A truly comprehensive study is yet to be done since many of the physical features are still poorly understood. However, piece by piece, with the efforts of many laboratories around the world, our understanding of plasmas is improving and the number of missing pieces is shrinking. Of the many applications of high energy density physics, one of the most exiting is certainly nuclear fusion. Although we have yet to realize engineering break even fusion, tremendous progress has been done with recent results at the National Ignition Facility showing scientific break even [72]. With progress in laser technology, photonics and diagnostics, researchers now have better tools to probe into new regimes of exotic matter with greater precision and accuracy. These experimental results combined with continuously improving modeling techniques have allowed for new insight in materials at extreme pressures and densities.

Kinetic codes, like PICLS, have had a long successful track record for modeling laser-plasma interactions. By nature, they are based on first principles of electrodynamics which allows them to make fewer assumptions about the conditions of plasmas they model which makes them very self-consistent. Their prohibitive computational cost however, means that Particle-in-Cell codes always require the most powerful computers available. Despite computing power maintaining an exponential increase over time, detailed 3D PIC simulations are still reserved for most powerful supercomputers in the world. This is due to the increasing regimes that are being simulated. Computers in the past were not capable of handling simulations above a few femtoseconds. Today, PIC codes can simulate plasmas over several picoseconds and in higher dimensions. Over the years, the traditional PIC method has been significantly extended to include new physics. Nowadays, an advanced code like PICLS includes binary collisions, and various atomic packages to improve their accuracy and make them more self-consistent. For example, PICLS now includes various ionization packages such as the Thomas-Fermi ionization model, electron impact ionization and field or tunnel ionization.

Using PICLS, we have modeled several laser-matter interaction scenarios with emphasis on electron ionization and transport in solid density targets. A simulation with silicate dioxide glass, an insulator, yielded interesting results concerning the ionization physics. We discovered that ionization was initially governed by tunnel ionization and it was revealed that a strong hemispherically expanding electric field driven by the ultra hot electrons was responsible for starting the ionization process. We then measured the speed of the ionization and derived a scaling rule to predict the ionization speed which depended on the square root of the laser intensity in the relativistic regime. The simulation results agreed with the scaling.

Traditionally, PICLS used the Thomas-Fermi model to calculate the average charge state of the plasma according to temperature and density. Given this model was developed for LTE plasmas, and that laser produced plasmas are typically not in LTE, a new ionization model was implemented based on electron impact ionization, a non-equilibrium ionization model. We then proceeded to compare the two models an immediately saw a difference in the ionization profiles. Additionally, the model's different approach to calculate ionization led to changes in transport patterns as well. A species dependence became apparent through a lag induced by the difference in collisional cross-section in one of the species which was more pronounced for impact ionization.

Finally, a series of simulations in resistive solid density media were conducted with the goal of explaining the electron transport patterns seen from a laser experiment done with aluminum and plastic. Again, a scaling which connected the laser intensity to the strength of the resistive magnetic field generated from an electron beam. The strength of the field (and indirectly the laser intensity) determined whether electrons were collimated or whether they diverged into numerous filaments. It was discovered that a material's resistivity is the dominant factor in determining the type of guiding one is expected to measure. A guiding conditions Γ was derived from the scaling and benchmarked against the simulation results. The simulations were in complete agreement with the scaling showing collimation and divergence exactly when they were expected. In addition, the simulation results were consistent with experimental results with plastic showing divergence and aluminum showing collimation for the appropriate laser intensities.

As an active and ongoing field of research, many questions and techniques remain to be explored for kinetic modeling. As laser technology progresses with increasing intensities and new regimes of plasma become accessible in the laboratory, the modeling of such plasma will continue to require the implementation of new and exciting physics. The next step in developing kinetic modeling codes involves the implementation of more complete atomic physics. The particle-in-cell code PICLS already includes multiple models to compute collisional ionization as well as field ionization which have been implemented first since they are among the more prominent atomic effects in solid density plasmas. Their implementation is currently incomplete and will require the inclusion of three-body recombination as the opposite atomic process to improve the self-consistency of the contribution of collisional ionization to the charge balance. Another area currently under active investigation is the role of radiation in influencing energy transport. Radiation plays a role in the ionization balance by the processes of photo ionization and its inverse radiative recombination. The importance of these effects is not well understood for various non-equilibrium plasma regimes so a an investigation using a kinetic code to measure them would yield important information about radiation transport. In addition to full scale ionization and recombination, the latest kinetic codes are not equipped to track ions in excited states. Ions may reach excited states through electron collisions or photo excitation and may subsequently relax depending on the lifetime of the excited state. During the decay process, radiation will be emitted which can either escape the material for an optically thin plasma, or be reabsorbed non-locally for an optically thick plasma. These atomically excited states and radiative transport effects are equally poorly understood and merit study to further enhance our understand of transport phenomenon in high energy density matter.

Electron transport is a complex topic with many different physical processes in order to consistently model this effect. Its understanding however, is of paramount importance to fast ignition since it relies on the coupling of electrons which are transported from the laser interaction region through solid gold before they reach the core. The optimization of such a problem will remain an important topic for experimental and theoretical research. In the future, computer modeling will continue to play an important role in supporting experimental results as new physics is uncovered and implemented to account for additional processes.

Chapter 5

References

[1] B.R. Chrisman. *Study of ultra-intense laser produced plasmas via computer simulation.* PhD thesis, University of Nevada, Reno, 2009.

[2] Y. Sentoku and A.J. Kemp. Numerical methods for particle simulations at extreme densities and temperatures: Weighted particles, relativistic collisions and reduced currents. *Journal of Computational Physics*, 227(14):6846–6861, July 2008.

[3] R. Mishra, P. Leblanc, Y. Sentoku, M.S. Wei, and F.N. Beg. Collisional particle-in-cell modeling for energy transport accompanied by atomic processes in dense plasmas. *Physics of Plasmas*, 20(7):072704, 2013.

[4] R.B. Stephens, R.A. Snavely, Y. Aglitskiy, F. Amiranoff, C. Andersen, D. Batani, S.D. Baton, T. Cowan, R.R. Freeman, T. Hall, S.P. Hatchett, J.M. Hill, M.H. Key, J.A. King, J.A. Koch, M. Koenig, A.J. MacKinnon, K.L. Lancaster, E. Martinolli, P. Norreys, E. Perelli-Cippo, M. Rabec Le Gloahec, C. Rousseaux, J.J. Santos, and F. Scianitti. K_ $\{\alpha\}$ fluorescence measurement of relativistic electron transport in the context of fast ignition. *Physical Review E*, 69(6):3–9, June 2004.

[5] Y. Sentoku, E. D'Humières, L. Romagnani, P. Audebert, and J. Fuchs. Dynamic Control over Mega-Ampere Electron Currents in Metals Using Ionization-Driven Resistive Magnetic Fields. *Physical Review Letters*, 107(13):135005, September 2011.

[6] A. Einstein. Zur quantentheorie der strahlung. *Physikalische Zeitschrift*, 1917.

[7] T.H. Maiman. Stimulated optical radiation in ruby. *Nature*, 187:493–494, 1960.

[8] R.G. Gould. The LASER, light amplification by stimulated emission of radiation. In *The Ann Arbor conference on optical pumping : the University of Michigan*, page 128. Ann Arbor, 1959.

[9] D. Strickland and G. Mourou. Compression of amplified chirped optical pulses. *Optics Communications*, 56:219, 1985.

[10] Y. Kitagawa, Y. Sentoku, S. Akamatsu, M. Mori, Y. Tohyama, R. Kodama, K.A. Tanaka, H. Fujita, H. Yoshida, S. Matsuo, T. Jitsuno, T. Kawasaki, S. Sakabe, H. Nishimura, Y. Izawa, K. Mima, and T. Yamanaka. Progress of fast ignitor studies and Petawatt laser construction at Osaka University. *Physics of Plasmas*, 9(5):2202, 2002.

[11] C.N. Danson, P.A. Brummitt, R.J. Clarke, J.L. Collier, B. Fell, A.J. Frackiewicz, S. Hancock, S. Hawkes, C. Hernandez-Gomez, P. Holligan, M.H.R. Hutchinson, A. Kidd, W.J. Lester, I.O. Musgrave, D. Neely, D.R. Neville, P.A. Norreys, D.A. Pepler, C.J. Reason, W. Shaikh, T.B. Winstone, R.W.W. Wyatt, and B.E. Wyborn. Vulcan Petawattan ultra-high-intensity interaction facility. *Nuclear Fusion*, 44(12):S239–S246, December 2004.

[12] M. Roth, T.E. Cowan, M.H. Key, S.P. Hatchett, C.G. Brown, W. Fountain, J. Johnson, D.M. Pennington, R.A. Snavely, S.C. Wilks, K. Yasuike, H. Ruhl, F. Pegoraro, S.V. Bulanov, E.M. Campbell, M.D. Perry, and H. Powell. Fast Ignition by Intense Laser-Accelerated Proton Beams. *Physical Review Letters*, 86(3):436–439, January 2001.

[13] S.Y. Kalmykov, S.A. Reed, S.A. Yi, A. Beck, A.F. Lifschitz, X. Davoine, E. Lefebvre, V. Khudik, G. Shvets, P. Dong, X. Wang, D. Du, S. Bedacht, Y. Zhao, W. Henderson, A. Bernstein, G. Dyer, M. Martinez, E. Gaul, T. Ditmire, and M.C. Downer. Laser wakefield electron acceleration on Texas petawatt facility: Towards multi-GeV electron

energy in a single self-guided stage. *High Energy Density Physics*, 6(2):200–206, June 2010.

[14] T. Tajima and G. Mourou. Zettawatt-exawatt lasers and their applications in ultrastrong-field physics. *Physical Review Special Topics-Accelerators and ...*, 2002.

[15] S. Suckewer. Ultra-intense lasers: Beyond a petawatt. *Nature Physics*, 2010.

[16] W.L. Kruer. *The physics of laser plasma interactions*. Addison-Wesley, 1988.

[17] P. Gibbon. *Short pulse laser interactions with matter*. Imperial College Press, 2005.

[18] F. Brunel. Not-so-resonant, resonant absorption. *Physical Review Letters*, 59(1):6–9, 1987.

[19] E.S. Weibel. Anomalous Skin Effect in a Plasma. *Physics of Fluids*, 10(4):741, 1967.

[20] W. Rozmus and V.T. Tikhonchuk. Skin effect and interaction of short laser pulses with dense plasmas. *Physical Review A*, 42(12), 1990.

[21] T.Y.B. Yang, W.L. Kruer, R.M. More, and A.B. Langdon. Absorption of laser light in overdense plasmas by sheath inverse bremsstrahlung. *Physics of Plasmas*, 2(8):3146, 1995.

[22] W.L. Kruer and K. Estabrook. JB heating by very intense laser light. *Physics of Fluids*, 28(1):430, 1985.

[23] J. Nuckolls, L. Wood, A. Thiesseen, and G. Zimmerman. Laser Compression of Matter to Super-High Densities: Thermonuclear (CTR) Applications. *Nature*, 239, 1972.

[24] M. Tabak, J. Hammer, M.E. Glinsky, W.L. Kruer, S.C. Wilks, J. Woodworth, E.M. Campbell, M.D. Perry, and R.J. Mason. Ignition and high gain with ultrapowerful lasers. In *Physics of Plasmas*, volume 1, pages 1626–1634, Lawrence Livermore Nat. Lab., CA, USA, May 1994.

[25] L. Willingale, P.M. Nilson, A.G.R. Thomas, S.S. Bulanov, A. Maksimchuk, W. Nazarov, T.C. Sangster, C. Stoeckl, and K. Krushelnick. High-power, kilojoule

laser interactions with near-critical density plasma. *Physics of Plasmas*, 18(5):056706, 2011.

[26] S.P. Hatchett, D. Clark, M. Tabak, R.E. Turner, C. Stoeckl, R.B. Stephens, H. Shiraga, and K. Tanaka. Hydrodynamics of conically guided fast ignition targets. *Fusion science and technology*, 49(3):307, 2006.

[27] C.K. Birdsall and A.B. Langdon. *Plasma physics via computer simulation.* Taylor & Francis Group, 2005.

[28] A.B. Langdon. Effects of the spatial grid in simulation plasmas. *Journal of Computational Physics*, 6(2):247–267, October 1970.

[29] J.D. Jackson. Classical Electrodynamics. In *Classical Electrodynamics*, page 781. Wiley, 1998.

[30] J.D. Jackson. Classical Electrodynamics. In *Classical Electrodynamics*, page 3. Wiley, 1998.

[31] J. Villasenor and O. Buneman. Rigorous charge conservation for local electromagnetic field solvers. *Computer Physics Communications*, 69(2-3):306–316, March 1992.

[32] G. Arfken. Mathematical Methods for Physicists. In *Mathematical Methods for Physicists.* Academic Press, 7 edition, 2012.

[33] T.Zh. Esirkepov. Exact charge conservation scheme for Particle-in-Cell simulation with an arbitrary form-factor. *Computer Physics Communications*, 135(2):144–153, April 2001.

[34] J.P. Boris. Relativistic plasma simulation-optimization of a hybrid code. *Proc. Fourth Conf. Num. Sim. Plasmas, Naval Res. Lab.*, 1970.

[35] R. Shanny, J.M. Dawson, and J.M. Greene. One-Dimensional Model of a Lorentz Plasma. *Physics of Fluids*, 10(6):1281, 1967.

[36] T. Takizuka and H. Abe. A binary collision model for plasma simulation with a particle code. *Journal of Computational Physics*, 25(3):205–219, November 1977.

[37] Y. Sentoku, K. Mima, Y. Kishimoto, and M. Honda. Effects of relativistic binary collisions on PIC simulation of laser plasmas. *Journal of the Physical Society of Japan*, 67(12):4084–4088, 1998.

[38] R.H. Miller and M.R. Combi. A Coulomb collision algorithm for weighted particle simulations. *Geophysical research letters*, 21(16):1735–1738, 1994.

[39] K. Nanbu and S. Yonemura. Weighted Particles in Coulomb Collision Simulations Based on the Theory of a Cumulative Scattering Angle. *Journal of Computational Physics*, 145(2):639–654, September 1998.

[40] R.P. Feynman, N. Metropolis, and E. Teller. Equations of State of Elements Based on the Generalized Fermi-Thomas Theory. *Physical Review*, 75(10):1561, 1949.

[41] R.E. Marshak and H.A. Bethe. The Generalized Thomas-Fermi Method as Applied to Stars. *The Astrophysical Journal*, 91:239, 1940.

[42] R. Latter. Temperature Behavior of the Thomas-Fermi Statistical Model for Atoms. *Physical Review*, 99(3):1854, 1955.

[43] R.M. More, K.H. Warren, D.A. Young, and G.B. Zimmerman. A new quotidian equation of state (QEOS) for hot dense matter. *Physics of Fluids*, 31(10):3059, 1988.

[44] R.M. More. PRESSURE IONIZATION, RESONANCES, AND THE CONTINUITY OF BOUND AND FREE STATES. In D R Bates and Benjamin Bederson, editors, *ADV IN ATOMIC & MOLECULAR PHYSICS*, volume 21 of *Advances in Atomic and Molecular Physics*, pages 305–356. Academic Press, 1985.

[45] D. Salzmann. *Atomic physics in hot plasmas.* Oxford University Press, 1998.

[46] H. Nishimura, R. Mishra, S. Ohshima, H. Nakamura, M. Tanabe, T. Fujiwara, N. Yamamoto, S. Fujioka, D. Batani, M. Veltcheva, T. Desai, R. Jafer, T. Kawamura, Y. Sentoku, R. Mancini, P. Hakel, F. Koike, and K. Mima. Energy transport and isochoric

heating of a low-Z, reduced-mass target irradiated with a high intensity laser pulse. *Physics of Plasmas*, 18(2):022702, 2011.

[47] A.J. Kemp, R.E.W. Pfund, and J. Meyer-ter Vehn. Modeling ultrafast laser-driven ionization dynamics with Monte Carlo collisional particle-in-cell simulations. *Physics of Plasmas*, 11(12):5648, 2004.

[48] W. Lotz. Electron-impact ionization cross-sections for atoms up to Z=108. *Zeitschrift fr Physik*, 232(2):101–107, April 1970.

[49] M. Protopapas, C.H. Keitel, and P.L. Knight. Atomic physics with super-high intensity lasers. *Reports on Progress in Physics*, 60(4):389–486, April 1997.

[50] L.D. Landau and E.M. Lifshitz. *Quantum Mechanics*. Pergamon, London, 3 edition, 1978.

[51] S. Kato, Y. Kishimoto, and J. Koga. Convective amplification of wake field due to self-modulation of a laser pulse induced by field ionization. *Physics of Plasmas*, 5(May 2008):0–7, 1998.

[52] S.C. Rae and K. Burnett. Detailed simulations of plasma-induced spectral blueshifting. *Physical Review A*, 46(2):1084–1090, 1992.

[53] G.S. Sarkisov, P. Leblanc, V.V. Ivanov, Y. Sentoku, V.Yu. Bychenkov, K. Yates, P. Wiewior, D. Jobe, and R. Spielman. Fountain effect of laser-driven relativistic electrons inside a solid dielectric. *Applied Physics Letters*, 99(13):131501, 2011.

[54] G.S. Sarkisov, V.V. Ivanov, P. Leblanc, Y. Sentoku, K. Yates, P. Wiewior, O. Chalyy, A. Astanovitskiy, V.Yu. Bychenkov, D. Jobe, and R.B. Spielman. Propagation of a laser-driven relativistic electron beam inside a solid dielectric. *Physical Review E*, 86(3):036412, September 2012.

[55] D. von der Linde and H. Schüler. Breakdown threshold and plasma formation in femtosecond lasersolid interaction. *JOSA B*, 13(1):216–222, January 1996.

[56] S.C. Wilks, W.L. Kruer, M. Tabak, and A.B. Langdon. Absorption of ultra-intense laser pulses. *Physical review letters*, 69(9):1383–1386, August 1992.

[57] S. Atzeni and J. Meyer-ter Vehn. The Physics of Inertial Fusion. In *The Physics of Inertial Fusion*, page 332. Oxford University Press, 2004.

[58] A.J. Kemp, Y. Sentoku, V. Sotnikov, and S.C. Wilks. Collisional relaxation of superthermal electrons generated by relativistic laser pulses in dense plasma. *Physical review letters*, 97(23):235001, December 2006.

[59] V. Malka, J. Faure, Y.A. Gauduel, E. Lefebvre, A. Rousse, and K.T. Phuoc. Principles and applications of compact laserplasma accelerators. *Nature Physics*, 4(June), 2008.

[60] A. Mančić, A. Lévy, M. Harmand, M. Nakatsutsumi, P. Antici, P. Audebert, P. Combis, S. Fourmaux, S. Mazevet, O. Peyrusse, V. Recoules, P. Renaudin, J. Robiche, F. Dorchies, and J. Fuchs. Picosecond Short-Range Disordering in Isochorically Heated Aluminum at Solid Density. *Physical Review Letters*, 104(3):035002, January 2010.

[61] H. Chen, S.C. Wilks, D.D. Meyerhofer, J. Bonlie, C.D. Chen, S.N. Chen, C. Courtois, L. Elberson, G. Gregori, W. Kruer, O. Landoas, J. Mithen, J. Myatt, C.D. Murphy, P. Nilson, D. Price, M. Schneider, R. Shepherd, C. Stoeckl, M. Tabak, R. Tommasini, and P. Beiersdorfer. Relativistic Quasimonoenergetic Positron Jets from Intense Laser-Solid Interactions. *Physical Review Letters*, 105(1):015003, July 2010.

[62] L. Disdier, J-P. Garconnet, G. Malka, and J-L. Miquel. Fast neutron emission from a high-energy ion beam produced by a high-intensity subpicosecond laser pulse. *Physical review letters*, pages 3–6, 1999.

[63] M.H. Key. Fast track to fusion energy. *Nature*, 412(6849):775–6, August 2001.

[64] S.V. Bulanov, T.Zh. Esirkepov, V.S. Khoroshkov, A.V. Kuznetsov, and F. Pegoraro. Oncological hadrontherapy with laser ion accelerators. *Physics Letters A*, 299(July):240–247, 2002.

[65] L. Gremillet, F. Amiranoff, S.D. Baton, J.-C. Gauthier, M. Koenig, E. Martinolli, F. Pisani, G. Bonnaud, C. Lebourg, C. Rousseaux, C. Toupin, A. Antonicci, D. Batani, A. Bernardinello, T. Hall, D. Scott, P. Norreys, H. Bandulet, and H. Pépin. Time-resolved observation of ultrahigh intensity laser-produced electron jets propagating through transparent solid targets. *Physical Review Letters*, 83(24):5015–5018, December 1999.

[66] J.J. Santos, F. Amiranoff, S.D. Baton, L. Gremillet, M. Koenig, E. Martinolli, M. Rabec Le Gloahec, C. Rousseaux, D. Batani, A. Bernardinello, G. Greison, and T. Hall. Fast Electron Transport in Ultraintense Laser Pulse Interaction with Solid Targets by Rear-Side Self-Radiation Diagnostics. *Physical Review Letters*, 89(2):025001, June 2002.

[67] M. Storm, A.A. Solodov, J.F. Myatt, D.D. Meyerhofer, C. Stoeckl, C. Mileham, R. Betti, P.M. Nilson, T.C. Sangster, W. Theobald, and C. Guo. High-Current, Relativistic Electron-Beam Transport in Metals and the Role of Magnetic Collimation. *Phys. Rev. Lett.*, 102(23):235004, June 2009.

[68] S. Chawla, M.S. Wei, R. Mishra, K.U. Akli, C.D. Chen, H.S. McLean, A. Morace, P.K. Patel, H. Sawada, Y. Sentoku, R.B. Stephens, and F.N. Beg. Effect of Target Material on Fast-Electron Transport and Resistive Collimation. *Physical Review Letters*, 110(2):025001, January 2013.

[69] R.D. Deslattes, E.G. Kessler, P. Indelicato, L. de Billy, E. Lindroth, and J. Anton. X-ray transition energies: new approach to a comprehensive evaluation. *Reviews of Modern . . .* , 75(January), 2003.

[70] A.R. Bell and R.J. Kingham. Resistive collimation of electron beams in laser-produced plasmas. *Physical review letters*, 91(3):035003, July 2003.

[71] L. Spitzer. Physics of Fully Ionized Gases. In *Physics of Fully Ionized Gases*, chapter 5. New York: Interscience, 1 edition, 1957.

[72] P. Rincon. Nuclear fusion milestone passed at US lab, 2013.

Appendix A

Publications

1. P. Leblanc, Y. Sentoku. “Scaling of Resistive Guiding of Laser Driven Fast Electron Currents in Solid Targets”. Submitted to Phys. Rev. E.
2. R. Mishra, P. Leblanc, Y. Sentoku *et al.*. “Collisional particle-in-cell modeling for energy transport accompanied by atomic processes in dense plasmas”. In: Phys. Plasmas 20.7 (2013), p. 072704.
3. G.S. Sarkisov, V.V. Ivanov, P. Leblanc *et al.*. “Propagation of a laser-driven relativistic electron beam inside a solid dielectric”. In: Phys. Rev. E 86.3 (Sept. 2012), p. 036412.
4. G.S. Sarkisov, P. Leblanc, V.V. Ivanov *et al.*. “Fountain effect of laser-driven relativistic electrons inside a solid dielectric”. In: Appl. Phys. Lett. 99.13 (2011), p. 131501.

Appendix B

Presentations

1. Oral presentations
   (a) P. Leblanc, Y. Sentoku. “Simulations of MA current transport in conductor and insulator laser irradiated targets”. HEDP Workshop (2013)
   (b) P. Leblanc, Y. Sentoku. “Simulations of MA current transport in conductor and insulator laser irradiated targets”. APS-DPP (2012)
2. Posters
   (a) P. Leblanc, Y. Sentoku. “Comparison of Equilibrium and Non-Equilibrium Ionization Models for Dielectric Materials”. SSAA (2012)
   (b) P. Leblanc, Y. Sentoku. “Comparison of Equilibrium and Non-Equilibrium Ionization Models for Dielectric Materials”. APS-DPP (2011)
   (c) P. Leblanc, Y. Sentoku. “Dynamics of Ionization Wave Produced by Relativistic Electron Beam Inside a Glass Target”. SSAA (2011)
   (d) P. Leblanc, Y. Sentoku. “Dynamics of Ionization Wave Produced by Relativistic Electron Beam Inside a Glass Target”. APS-DPP (2010)
   (e) P. Leblanc, Y. Sentoku, R. Presura. “Ultra-fast Magnetized Laser-Matter Interactions”. APS-DPP (2009)